Experimental and Numerical Analysis of Damage in Notched Composites

Bilel Aidi

Dissertation submitted to the faculty of the Virginia Polytechnic Institute and State University in partial fulfillment of the requirements for the degree of

Doctor of Philosophy
In
Engineering Mechanics

Scott W. Case, Chair
Brian Y. Lattimer
Raffaella De Vita
Saad Ragab
Mark Cramer

08/11/2016
Blacksburg, Virginia

Keywords: Carbon fiber; notched composite; fatigue; residual properties; digital image correlation (DIC) ; damage monitoring; vibration; Finite Element Method

Experimental and Numerical Analysis of Damage in Notched Composites

Bilel Aidi

ABSTRACT

This dissertation contains the results from an experimental study, numerical, and analytical study conducted on quasi-isotropic carbon fiber laminates containing a center hole (notch) subjected to constant amplitude tension-tension fatigue loading in order to investigate the effect of fatigue damage development on the residual properties. Quasi-static tests were initially performed on notched composites using digital image correlation (DIC) to determine the strain profiles at selected transverse sections of the outer ply of the laminates and the static strength of the laminates. Subsequently, tension-tension fatigue tests were carried out at 70%, 75% and 80% of the nominal static failure load. A finite element model was developed using Abaqus and Digimat in which Digimat was used to implement the damage evolution model via a user-defined material subroutine. Damage initiation has been assessed using Hashin's failure criteria and the Matzenmiller model was adopted for damage evolution. A second finite element model was developed using Abaqus and Autodesk Simulation Composite Analysis (ASCA) in which ASCA was used to implement the user-material subroutine. The subroutine includes a failure initiation criterion based upon multi-continuum theory (MCT) and an energy-based damage evolution law. Numerical and experimental strain results were presented and compared for different section lines on the outer surface of the laminate at different loading stages. Additionally, the experimentally measured notched composite strength was compared with the predictions from the finite element solutions. These results are used as baseline for subsequent comparison with strain profiles obtained using DIC for specimens fatigued at different stress levels and fatigue lifetime fractions. The results showed a significant effect of fatigue damage development on strain redistribution even at early stages of fatigue. The results also showed the capability of DIC technique to identify damage initiation and its location. Furthermore, X-ray computed tomography (CT) was used to examine the sequence of damage development throughout the fatigue lifetime and to connect the observed damage mechanisms with the occurred change of strain profiles.

Experimental vibrational modal analysis tests were also conducted to assess the effect of fatigue damage on the residual frequency responses (RFRs). Vibrational measurements were initially performed on pristine notched composites. The results are used as baseline for subsequent comparison with strain profiles obtained with DIC. Finite element models based on the classical plate theory (Kirchhoff) and the shear deformable theory (Mindlin) within the framework of equivalent single-layer and layer-wise concepts as well as the three-dimensional theory of elasticity are developed to predict the natural frequencies of non-fatigued specimen. These models are implemented using the finite element software, Abaqus, to determine the natural frequencies and the corresponding mode shapes. In addition, an analytical model based on Kirchhoff plate theory is developed. Using this approach, an equivalent bending-torsion beam model for cantilever laminated plates is extracted taking into account the reduction in local stiffness and mass induced by the center hole. Numerical and analytical natural frequency values are then compared with those obtained through experimental vibrational tests, and the accuracy of each finite element (FE) and analytical model type is assessed. It is shown that the natural frequencies obtained using the analytical and FE models are within 8% of the experimentally determined values.

Dedication

Dedicated to

My loving parents Nasreddine Aydi and Saousen Kharrat for their unwavering support and guidance.

My brother Bassem and sister Rania.

My supervisor.

Acknowledgement

First of all, I thank ALLAH, the most Merciful and most Gracious, for this achievement.

I would like to express my gratitude to my supervisor, Dr. Scott W. Case, whose expertise, understanding, and patience, added considerably to my post graduate experience. I appreciate his immense knowledge and various skills in many areas including composite materials. His assistance in research and writing either conference or journal papers has helped shape my skills and enlarge my sphere of knowledge. Beyond that, he was very supportive, helpful and understanding person outside the work context. I could not have imagined having a better advisor and mentor for my Ph.D study.

Besides my advisor, I would like to thank the rest of my thesis committee members, Dr Brian Lattimer, Dr Raffaella De Vita, Dr Saad Ragab and Dr Mark Cramer for their insightful comments and useful feedback.

My sincere thanks go to Dr Michael Philen from the Aerospace and Ocean Engineering Department at Virginia Tech for giving me access to his laboratory and research facilities.

I would like to acknowledge the support of BEAM laboratory supervisors Mac McCord and Danny Reed in operating the MTS machines and constructing the materials as well as Dr Cheryl Carrico from the Engineering Education Department for providing the composite materials from Hexcel Company for composite fabrication. Without their precious support it would not be possible to conduct this research.

I would like to extend my appreciation to the Department of Biomedical Engineering and Mechanics and particularly to the Graduate Committee for honoring me with the prestigious award Amir Chand and Dewki Bai Batra Scholarship, for nominating me as the best teaching assistant in 2014, and also for giving me the opportunity to teach the mechanical behavior of materials laboratory as an instructor for almost 2 years. This award and confidence in teaching has made me more responsible and has given me a strong push to pursue my engineering education with greater pledge.

I am also thankful to all staff members of the Biomedical Engineering and Mechanics Department. Special thanks go to Beverly S. Williams, Melissa D. Nipper, Amanda Stanley and Lisa Smith for their pleasant personalities and precious administrative help.

I am also grateful to Dr. Slim Choura for having introduced me to the Department of Biomedical Engineering and Mechanics and for his continuous encouragement and practical advice throughout my academic career.

I would like to thank my dear friend and collaborator Dr Abdessattar Abdelkefi for his encouragement, care and advice throughout my PhD research journey. His enthusiasm of increasing knowledge and solving problems has impressed and motivated me to perform better.

I am also grateful to my collaborators Mohamed Ibrahim Shaat and Hichem Abdelmoula from New Mexico State University. I would like also to thank Roger Assaker CEO of e-Xtream engineering for introducing me to Bob Schmitz and Philippe Hebert to use Digimat.

I am also thankful to Ameni Hlioui for her time to do the English editing of my reports and to Elizabeth Mack for proofreading them.

I thank my colleagues in the department: Roozbeh Kalhor, Dr Yanyun Chen, Farzad Ahmadi for the stimulating discussions either in engineering or eco-socio-political subjects, for their help during experimental setups, and for all the fun we have had in the last four years. A special thanks goes to Dr Jessica May and Dr Patrick Summers for their guidance and help in using the Aramis and Correlated Solutions DIC systems respectively.

My time at Blacksburg was made enjoyable in large part due to the many friends and groups that became a part of my life. I am grateful for the time spent with special and unique roommates and friends Mohamed Jrad, Nejib Masghouni, Karim Fadhloun, and Youssef Bichiou. I also would like to thank all my friends in Blacksburg, especially Faycal Beji and his wife Autumn Taylor, Maha Elouni, Imen Tanniche, Dr Sameh Ben Ayed, Dr Mehdi Ghommem, Dr Omar Al-Abbasi, Dr Amara Loulizi, Dr Amr Hilal, Dr Zakariya Dalalah, Khaled Adjerid and Dr Shahriar Kabir. My outmost sincere thanks also go to Dr Saher Lahouar and his wife Afek Jaballah for their parent-like support, generous care and the home feeling atmosphere I get whenever we meet at our usual gatherings or at celebrating special events.

My thanks go to my best friends in Tunisia Mahdi ben Hmouda, Bilel Ben Amira, Amel Gammoudi, Wael Baba, and Bayram Jribi.

Lastly, I would like to express my profound gratitude to my beloved parents Nasreddine Aydi and Saousen Kharrat for all their love, encouragement and continuous support (materially and emotionally). They raised me with a love for science and supported me in all my life goals. I would like to express my gratitude as well to my dearest brother Bassem and dearest sister Rania. My deepest appreciation goes to my supportive and encouraging fiancée Hana Dammak for her love and deep faith in my abilities during the final stages of this Ph.D. I extend my thanks as well to all my family members for their support with a special thought to Foued, Mehrez, Mejda, Imene, Lobna, Salma, Nidhal and Amal.

I am so grateful for all those who helped me along this journey. Without you all, I would have never gotten close.

List of Figures

List of Tables

Chapter 1. Introduction and Dissertation Objectives

The application of polymer matrix composites in aerospace, civil infrastructure, wind turbine, marine, and automotive applications has evolved as a result of the need to improve structural performance and reduce total weight. The advantages of composite materials, such as specific stiffness and strength to weight ratios, corrosion resistance, excellent surface profiles, enhanced fatigue resilience, and tailored performance, have been the main reasons for their rapidly increasing utilization in various applications. In fact, their use is seen to be broadening and now extends in a wide range of various fields among which these can be mentioned: medicine, dental and pharmaceutical applications. Research in these fields was focused on the use of bio-composites for bone grafts, artificial prostheses, medical stents and dental fillers [1].

Furthermore, the application of advanced composite materials in airframe structures is increasing with every new aircraft designed and produced. This is particularly true for military fighter aircraft. The F-15 Eagle, a 1968 aircraft, has a 1.5% of its structural weight made from composite materials while the newest F-35 comprises about 38% composites. The commercial aircraft field has also had a significant increase of composite materials in the airframe. Boeing jumped from 12% on the 777 to 50% on the Dreamliner 787 while Airbus moved from 10% on the A340 to 53% on the A350 XWB. Figure1.1 provides a chart showing the increase in the use of composite materials in aircraft over the last few decades [2].

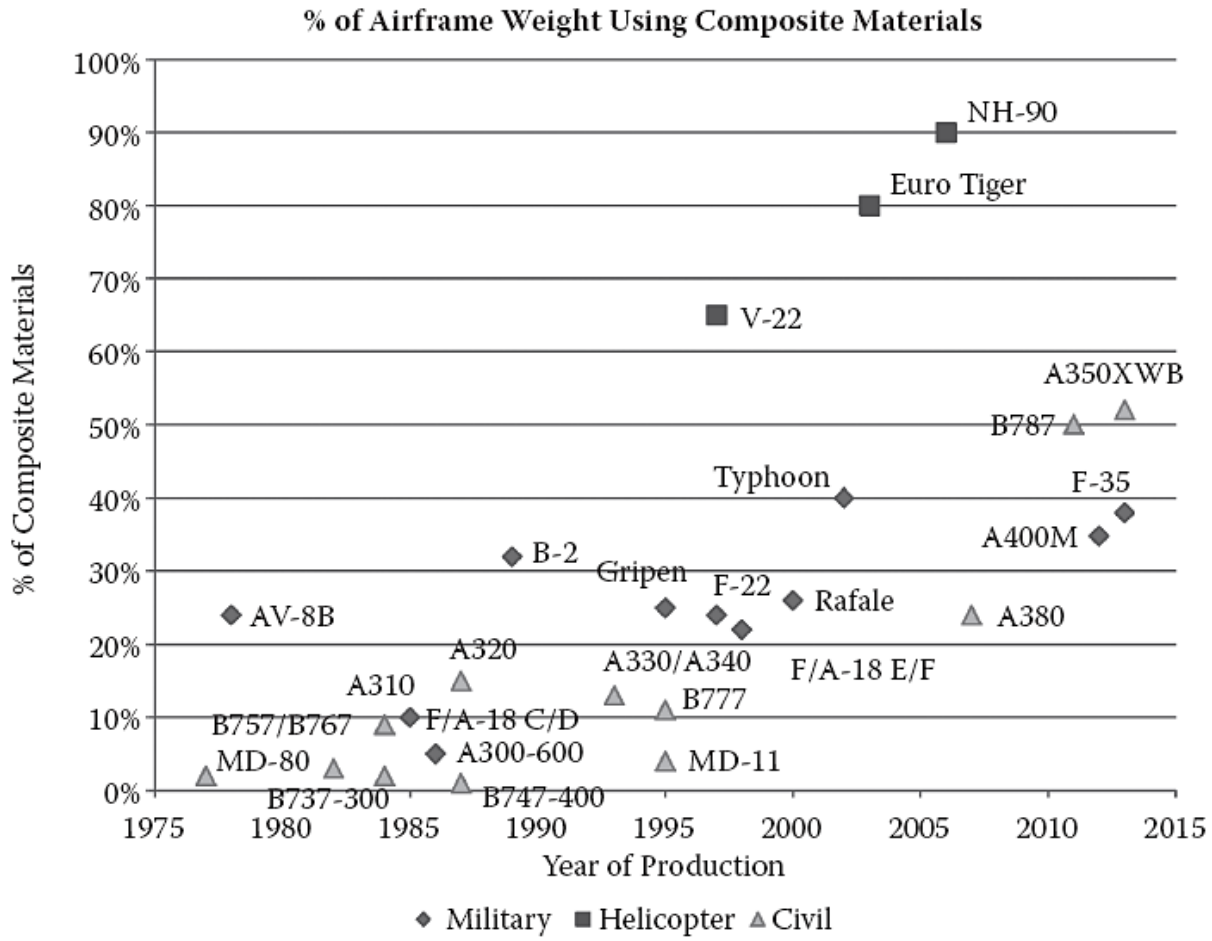

Figure 1.1. Growth in composite materials used in airframes [2]

The designs for these composite structures frequently include discontinuities such as cut-outs for access or fastener holes for joining and these become critical regions under thermo-mechanical loading. The understanding of the behavior of such structures is essential for the design of complex structures where parts are mostly connected with bolts and rivets. However, the potential advantages of composite structures will not be fully realized unless the structural joints are designed efficiently taking into account the fact that the damage and failure mechanisms of a loaded notched composite laminate are more complex than unnotched laminates due to the presence of the notch and the resulting stress gradients. Damage in composites initiates and accumulates in a fashion different from metals, predominantly because of the inherent inhomogeneous and anisotropic nature of these materials. Damage in metals often reveals itself in a localized manner (single crack leading to

failure) while damage in composites occurs simultaneously at different locations with various crack types [3]. For the validation of the structural durability and system reliability of safety components made from FRPs, the material characteristics with their very different failure mechanisms compared to metals, manufacturing properties and component performance must be considered. Figure 1.2 shows the typical failure mechanisms of an open hole $[45_2/90_2/-45_2/0_2]_s$ composite laminate fatigued with a stress level of 60% UTS and undergone a 15% of stiffness loss obtained from X-ray micro computed tomography (CT).

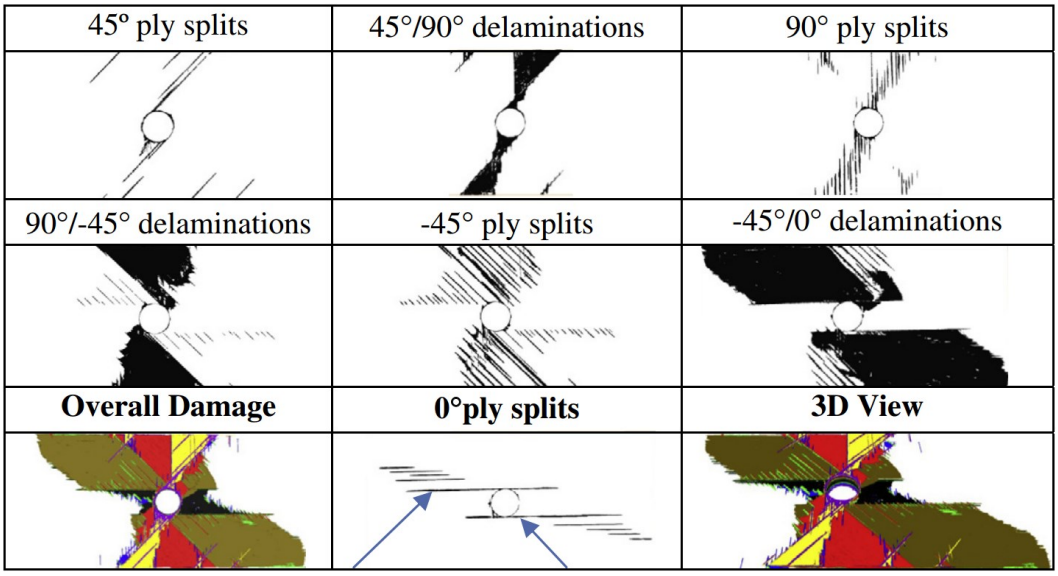

Figure 1.2. An interrupted test of a laminate $[45_2/90_2/-45_2/0_2]_s$ fatigued till 15% of stiffness loss with a stress level of 60%UTS [4].

Several experimental tools and techniques have been used to characterize the damage in carbon fiber reinforced plastics (CFRP). Acoustic emissions, ultrasonic, electrical resistance measurements, and fiber optic sensors (EFPI and FBG sensors) were used for the analysis of the damage-induced behavior. More recently, full-field measurement techniques, such as Digital Image Correlation and Thermography, as well as the X-Ray Computed Tomography have been used to capture the involved physical mechanisms during loading and to understand the relevant damage process [5].

Different numerical approaches have been used to simulate intra-ply and inter-ply failures mechanisms. Many different failure criteria based on the three-dimensional stress state and the unidirectional layer strength properties (e.g. Tsai-Wu, Hashin, Puck) were developed to predict the failure within the ply. However, these failure criteria are not sufficient for the prediction of

laminate failure. Thus, the progressive failure approach must be used. In this context, continuum damage models based on gradual softening have been employed. One such popular continuum damage formulations is the Matzenmiller model [6] in which distinction between fiber failure and matrix failure is taken into account. However, a correct prediction of matrix cracking is not guaranteed in continuum models and therefore spurious damage mechanisms may be predicted. To alleviate this problem matrix cracks have been modeled with interface elements (cohesive elements), but where crack locations must be predefined. XFEM with the use of enriched finite elements has also been used in an attempt to eliminate the need to predefine cracks [7]. In addition, delamination modeling has been accomplished with interface elements [8, 9]. These interface elements most often incorporate a simple bilinear softening law in which the fracture energy is a phenomenological function of the mode mixity as formulated by Benzeggagh and Kenane [10].

The overarching goal of this dissertation is to fabricate and characterize notched FRP composites under quasi-static and fatigue loading. Studying the effect of the discontinuities on the behavior of composite materials under these loading conditions is important. The Digital Image Correlation (DIC) technique is employed to obtain the full-field surface strain measurements of open-hole carbon fiber epoxy composite plates subjected to uniaxial tensile loading. Finite element models are developed and validated based on the measured open-hole strengths as well as the strain distributions. This represents a contribution to the current research since there is no comparison of experimental strain contours with numerical strains obtained from progressive damage models. Moreover, the effect of different stacking sequences and hole sizes on the ultimate tensile strength are also investigated. An extensive experimental program is conducted to evaluate the residual properties of notched composites under fatigue loading, for different stress levels, using different measurement techniques. DIC and non-contact vibration measurement techniques are used to characterize the damage evolution. The combination of both methods to assess residual properties represents a key contribution to the current research, in addition, the current work represents the first attempt to monitor the change in strain contours frequency response signatures of open-hole composites at various stress levels .Penetrant enhanced X-ray radiographs are taken to identify the failure mechanisms throughout fatigue lifetime. The resulting in-depth understanding of the progressive damage mechanisms paves the way towards predictive fatigue models and further material optimization with respect to fatigue and durability [3].

Chapter 2. Experimental and numerical determination of strength and strain contours of notched composites under tension loading

2.1. Abstract

Experimental quasi-static tests were performed on center notched carbon fiber reinforced polymer (CFRP) composites having different stacking sequences made of G40-600/5245C prepreg. The three-dimensional Digital Image Correlation (DIC) technique was used during quasi-static tests conducted on quasi-isotropic notched samples to obtain the distribution of strains as a function of applied stress. A finite element model was built within Abaqus to predict the notched strength and the strain profiles for comparison with measured results. A user-material subroutine using the multi-continuum theory (MCT) as a failure initiation criterion and an energy-based damage evolution law as implemented by Autodesk Simulation Composite Analysis (ASCA) was used to conduct a quantitative comparison of strain components predicted by the analysis and obtained in the experiments. Good agreement between experimental data and numerical analyses results are observed. Modal analysis was carried out to investigate the effect of static damage on the dominant frequencies of the notched structure using the resulted degraded material elements. The first in-plane mode was found to be a good candidate for tracking the level of damage.

2.2. Introduction

The use of fiber reinforced composite materials continues to increase in many applications such as aerospace, automotive, submarine, medical equipment and civil engineering structures. They offer various advantages such as high stiffness- and strength-to-weight ratios, corrosion resistance, and high fatigue strength. Composite structures usually require the use of mechanical joints in order to satisfy design specifications and to transfer loads between different parts of hybrid assemblies that are made of composite and metal. However, the potential advantages of composite structures will not be fully realized unless the structural joints are designed efficiently since the joint efficiency of ductile metals has been shown to be as much as twice that of the CFRP composites [11]. Therefore, suitable analysis methods for the failure strength would help in selecting the appropriate

joint size in a given application [12]. However, the damage and failure mechanisms of a loaded notched composite laminate are more complex than in an unnotched laminate due to the existence of the notch and the resulting stress gradients. Indeed, subcritical damage modes such as transverse matrix cracks, axial splits (fiber/matrix shearing), and delamination between adjacent layers in the vicinity of the highly stressed regions of the hole boundary contribute to the relief of stress concentration that exist at the hole [13]. The sensitivity of a composite laminate to notches is dependent on many factors such as notch size and geometry, laminate thickness, fiber orientation, and machining quality. Green et al. [14] studied the effect of sublaminate-level scaling and ply-level scaling on the tensile strength of notched composites. Three different scaling types were adopted: the first was increasing the thickness of the laminate only, the second was increasing the in-plane dimensions (hole diameter, width and length of specimen) but maintaining a constant thickness, and the third type was increasing all specimen dimensions simultaneously. Over a scaling range of 8 from the baseline specimen, both decreases and increases in notched strength were noted, with a maximum reduction of 64% observed over the scaling range tested. Wisnom and Hallet [15] showed that, for specific ply block thicknesses, failure stress increased with increasing hole diameter, the opposite to the usual hole size effect. This effect is because of the crucial role delamination may play in the strength and failure mechanisms in open hole samples tested in tension. Qin et al. [16] used Digital Image Correlation (DIC) method to study the notch effect with different patterns and localizations of carbon fiber reinforced carbon matrix composites. Using the full-field measurement, both the local mechanical properties (stress concentration, shear damage, and fracture behavior) and the globe properties (notch sensitivity and tensile behavior) were studied. Caminero et al. [17] also used DIC to assess the damage taking place in composite plates with an open hole loaded in tension as well as to investigate the damage and performance of adhesively bonded patch repairs in composite panels under tension loading. They compared the stress concentration factors obtained analytically using the elastic solution of an infinite orthotropic plate containing a hole with the experimental results obtained from DIC measurements.

In addition to the experimental investigation of failure of notched samples of different types, analytical models for the prediction of notched strength have been adopted for preliminary design purposes. These models rely on the analysis of the stress distribution near the notch or on the use of linear elastic fracture mechanics. One early and widely used model is the point stress criterion

(PSC) developed by Whitney and Nuismer [18]. This criterion assumes that fracture occurs when the tensile stress reaches the unnotched strength at a characteristic distance from the notch. The earliest energetic model was developed by Waddoups et al. [19]; it predicts that fracture occurs if the energy release rate for an equivalent critical length reaches the material toughness Gc. Martin et al. [20] used an improved PSC criterion that combines strength and energy approaches and geometry (hole size and plate width) to analyze the strength of notched plates. Moreover numerical models have been developed for the same context to predict strength and failure mechanisms. Hallet et al. [21] developed a 3D finite element model of notched composite using cohesive elements to model axial splits and delamination propagation in conjunction with a Weibull criterion for fiber failure. Atas and Soutis [22] developed a similar model with the inclusion of nonlinear stress-shear strain curve. They showed its influence on the strength and subcritical damage development of the CFRP laminates. Van Der Meer et al. [7] extended the previous work by using the phantom node method to predict arbitrary transverse matrix cracks in 90° and axial splits in 0° plies with enriched elements. However, they still predefined the matrix crack paths in 45° plies. Ridha et al. [23] used a different approach for in-plane damage within the finite element framework by developing a progressive damage model based on matrix and fiber energy release rates to describe the in-plane material softening as well as the failure pattern of fiber and matrix damage. Recently, Su et al. [24] developed a finite element model to predict compressive strengths and progressive failure patterns for open-hole laminates. The Hashin criteria and energy-based linear softening laws were implemented to represent in-plane failure and delamination. They predicted some of the failure mechanisms and compared them to experimentally observed ones. In addition, they explained the reasons behind the different failure mechanisms observed between sublaminate scaled laminates and ply-level scaled laminates.

Furthermore, vibration-based structural health monitoring (SHM) has been used as a reliable technique to assess and detect damage in composite structures under normal service. Changes in natural frequencies can be correlated to loss of stiffness caused by the typical failure modes of composite structures (i.e matrix cracking, fiber breakage and delamination). Several experimental, numerical, and analytical studies have been carried out on composite structures containing initially embedded defects involving the direct vibration problem. Each study considered only one type of damage: cut-outs (notches), transverse matrix cracks, delamination or impact failures with possible different shapes, locations and severities [25-29]. Capozucca and Bonci [25] performed experimental

and analytical analysis of damaged and undamaged CFRP laminate elements under free vibration. The actual damage consisted of double rectangular notches on different sections of the specimens with varying increases in width resulting in local reduction of stiffness with effects on dynamic response. Analytical frequency values are compared with those obtained through tests and finite element analysis. Zhang et al. [27] performed experimental modal testing on simply supported and cantilever quasi-isotropic composite beams with different delamination locations and severities. A finite element model was built using contact elements between layers to compare the predicted natural frequencies with experimental ones for various damage scenarios. In addition, the authors used a graphical approach which requires an a priori database of frequency shifts versus delamination parameters to estimate the interface, span-wise location, and size of delaminations within the composite sample. However, there is still a lack of studies that involve the effect of real progressive damage on the vibration response of composite specimens subjected to tension loading.

The objective of this study is to develop a progressive damage finite element method that is sufficiently general to predict the open-hole tension (OHT) strength and failure behavior of brittle (fiber-dominated failure with little sub-critical damage) or more ductile (fiber-dominated failure with extensive sub-critical damage) fiber reinforced composite laminates that do not exhibit significant delamination [14], requiring only the ply-level properties of composites and the energies dissipated during fiber and matrix damage. The predictions of the strengths are compared with the experimental results for composite laminates with a variety of stacking sequences. The DIC technique is used to obtain the full-field strains on the outer layer of the quasi-isotropic notched composite under tension loading. The experimental strain profiles are compared to the finite element solutions for the laminate at different section locations. Subsequently, the effect of progressive damage, described by the degradation of elastic properties, on the modal parameters of notched composites is investigated.

2.3. Finite Element Model

The FEA model presented in this section is a representative model for all notched samples, with different stacking sequences and hole sizes, used for the experimental determination of the ultimate tensile strength. An open-hole tension plate made from G40-600/5245C composite is developed within Abaqus/CAE and partitioned as shown in Figure 2.1 in order to assign various edge seeds

to obtain this specific mesh. The composite sample is 127 mm in length, 25.4 mm in width and 2.54 mm depth. The mesh was tailored to enable more efficient model runtime by specifying a fine and regular mesh around the notch and a progressively coarser mesh away from the hole. The illustration of the meshed model, with a total of 12,288 elements and 56,672 nodes, is shown in Figure 2.1.

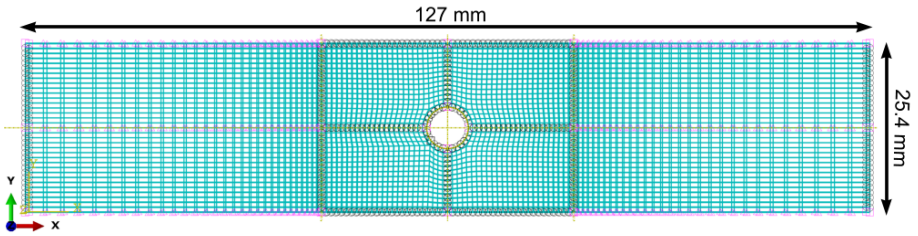

Figure 2.1. Edges seeding of partitioned geometry

For each lamination sequence consider the orientation of unidirectional plies is measured with regard to the sample length (*x*-axis). The model is meshed with 8-node first-order brick elements with reduced integration and hourglass control. Since layered elements are used in all FE models, a swept mesh is used to define consistent top and bottom element faces. The use of the Abaqus continuum element C3D8R that explicitly accounts for all six stress components admits the use of material failure criteria that utilize the transverse stress components that are neglected (or only approximated) in conventional or continuum shell elements. All material properties (i.e. linear elastic moduli, damage initiation, and evolution properties) are assigned through ASCA. Boundary conditions have been selected in order to replicate experimental conditions used on axial testing of similar notched samples (Figure 2.2).

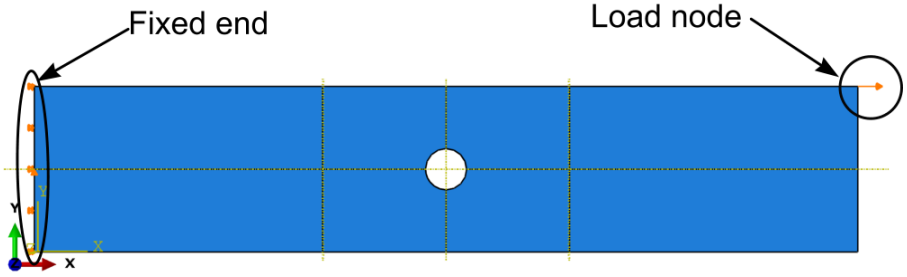

Figure 2.2. Boundary conditions and load configuration

Therefore the nodes at the bottom are encastre. Additionally, the top surface of the plate undergoes an imposed vertical displacement. A constraint equation is applied to a set of nodes "tiednodes", which represent all the nodes at the loaded end of the plate except one, and a single node "loadnode", which represents the remaining node at the top surface. This is done to allow simple determination of the total reaction force during post-processing from the "loadnode". To achieve robust convergence when using ASCA, the solution controls for the quasi-static step must be modified from their default state as discussed in [30].

Each composite material system which will be used with ASCA has to be created through a stand-alone graphical-user interface program Autodesk Composite Material Manager (ACMM) within the ASCA package. The properties of the material, G40-600/5245C, used in this work and entered into ACMM are given in Table 2.1.

Table 2.1. G40-600/5245C Ply elastic properties

E_1	E_2	G_{12}	γ_{12}
179 GPa	8.5 GPa	5 GPa	0.378

Since the micromechanical failure criteria used in the current work decomposes the lamina-level stresses into fiber and matrix stresses, the fiber and matrix stiffnesses must also be provided. The process of decomposition is described in detail in [31]. These fiber and matrix properties are iteratively tuned within ACMM to match the specified lamina properties and volume fraction as well as fiber and matrix behaviors. Typical fiber and matrix elastic constants of G40-600/5245C are presented in Table 2.2.

Table 2.2. G40-600/5245C Constituent elastic properties

Constituent	$E_1(MPa)$	$E_2(MPa)$	$G_{12}(MPa)$	γ_{12}
Fiber	321300	14030	14730	0.303
Matrix	3901	3901	1344	0.451

In Abaqus, five failure criteria are provided for use in linear elastic analyses: four stress-based criteria (maximum stress, Tsai-Hill, Tsai-Wu, Azzi-Tsai-Hill) and one strain-based criterion (maximum strain). The practical utility of these linear elastic failure criteria is quite limited because they only predict the occurrence of localized failure, not the consequences of localized failure. Within Abaqus, there is only one damage evolution model which must be used in

combination with Hashin's damage initiation criteria. This implementation of this model in Abaqus is based entirely upon an assumed condition of plane stress. Consequently, it can only be used in plane stress 2D continuum elements or shell elements [32]. ASCA uses a general 3D state of stress in its applicable failure criteria. As a further contrast, the Abaqus linear elastic failure criterion utilizes the homogenized composite state of stress or strain to predict failure of the homogenized composite material, whereas ASCA utilizes constituent average stress to independently predict failure of each constituent material. An additional shortcoming of the Abaqus damage model is its numerical instability and non-convergence in the phase of an in-plane material softening or stiffness degradation. As a result, viscous regulation is used to improve the convergence rate in the softening regime; nevertheless, the amount of energy associated with viscous regularization over the whole model must be controlled to obtain physically meaningful results. In contrast, ASCA uses a zigzagging curve that approximates the linear softening curve to alleviate this problem when adopting the energy based scheme. This is performed by degrading the material stiffness (secant stiffness) in a stepwise manner.

ASCA provides two material degradation schemes for intra-laminar material failure: instantaneous degradation and energy-based material degradation. The latter method was adopted in the current work. To use the energy-based degradation (EBD) feature in ASCA, values are required for the total energy dissipated in the composite after matrix and fiber constituents reach their fully degraded conditions (G_m and G_f, respectively) [33, 34].

The failure criteria for each constituent matrix or fiber are defined in eq (2.1) and eq (2.2) utilizing the constituent stress information produced by MCT

$$\pm K_{2m}(\sigma_{22m}+\sigma_{33m})^2 + K_{3m}(\sigma_{22m}^2+\sigma_{33m}^2+2\sigma_{23m}^2) + K_{4m}(\sigma_{12m}^2+\sigma_{13m}^2) = 1 \qquad (2.1)$$

$$\pm K_{1f}\sigma_{11f}^2 + K_{4f}(\sigma_{12f}^2+\sigma_{13f}^2) = 1 \qquad (2.2)$$

where the ± symbol indicates that the appropriate tensile or compressive ultimate strength value is used depending on the constituent's stress state. The values K_{im} and K_{if} are coefficients of matrix and fiber failure criteria respectively that are dependent on the constituent strength values [31].

After damage initiation within the matrix or fiber constituent is predicted using MCT, the response of that constituent beyond that relevant critical strain must be softened to allow redistribution of load to the other constituent and to surrounding plies. A typical constitutive relation that permits

the rate of material degradation to be controlled is a bi-linear law composed of a linear elastic region followed by a linear stiffness degradation region as shown in Figure 2.3 [35].

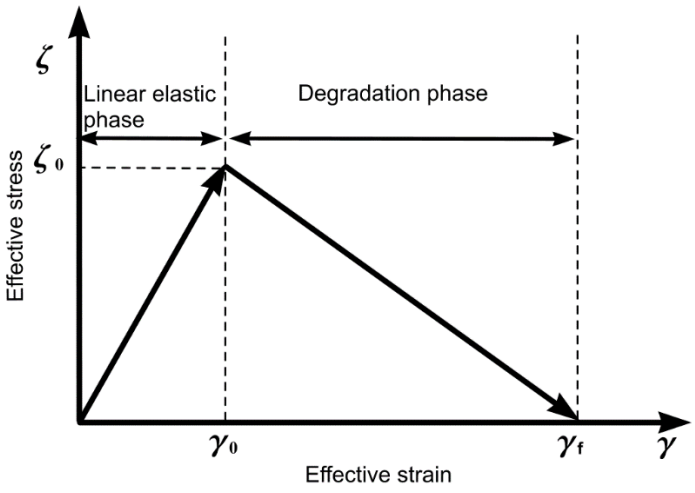

Figure 2.3. ***Piecewise linear damage evolution law***

For each failure mode, the energy dissipated due to failure represents the area under the bilinear curve. This total energy can be expressed as

$$G = \frac{1}{2}\zeta_0 \gamma_f L_e \tag{2.3}$$

where ζ_0 is the value of measured effective stress at failure initiation, γ_f is the value of the measured effective strain at final failure and L_e is the representative element length as defined by Abaqus [32]. The values of γ_f for the various modes of failure depend on the respective *G* values. Thus separating failure modes allows the constituents to degrade independently of each-other, providing a physical reality to the progressive failure analysis. Once damage initiation occurs for one or both constituent materials, an expression for constituent damage evolution that is applicable for any strain state that the material might experience is required. For this purpose, it is expedient to utilize an effective scalar measure of stress and strain that is appropriate for each of the constituents. To predict damage evolution within the matrix constituent, we define the effective stress and strain as follows

$$\zeta^m = \sqrt{\sigma_{22}^2 + \sigma_{33}^2 + \sigma_{12}^2 + \sigma_{13}^2 + \sigma_{23}^2} \tag{2.4}$$

$$\gamma^m = \sqrt{\varepsilon_{22}^2 + \varepsilon_{33}^2 + \varepsilon_{12}^2 + \varepsilon_{13}^2 + \varepsilon_{23}^2} \tag{2.5}$$

where ζ^m is the effective stress and γ^m is the effective strain. To predict damage evolution within the fiber constituent, we define an effective stress and strain as

$$\zeta^f = \sqrt{\sigma_{11}^2} \tag{2.6}$$

$$\gamma^f = \sqrt{\varepsilon_{11}^2} \tag{2.7}$$

where ζ^f is the effective stress and γ^f is the effective strain.

The evolution of the constituent damage variables is expressed in terms of these effective strains. The fiber damage d_f $(0 \le d_f \le 1)$ is computed by

$$d_f = \frac{\gamma_0^f \left(\gamma^f - \gamma_0^f\right)}{\gamma^f \left(\gamma_f^f - \gamma_0^f\right)} \tag{2.8}$$

where γ_0^f and γ_f^f are the value of the effective strain γ^f at damage initiation and at full fiber degradation, respectively. The matrix damage d_m $(0 \le d_m \le 1)$ is computed by

$$d_m = \frac{\gamma_0^m \left(\gamma^m - \gamma_0^m\right)}{\gamma^m \left(\gamma_f^m - \gamma_0^m\right)} \tag{2.9}$$

where γ_0^m and γ_f^m are the value of the effective strain γ^m at damage initiation and full matrix degradation, respectively. The values of fiber and matrix damage calculated using eq (2.8) and eq (2.9) are presented graphically in Figure 2.4.

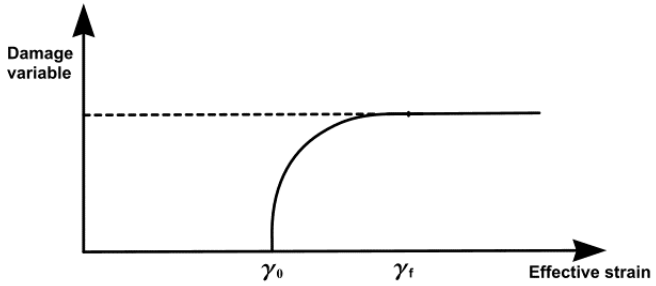

Figure 2.4. ***Damage variable as a function of effective strain.***

It should be re-emphasized that the dissipated energy of a fully degraded material is directly proportional to γ_f^m and γ_f^f. Therefore, mesh sensitivity is alleviated by making γ_f^m and γ_f^f proportional to element size, so that

$$\gamma_f^m = \frac{2G^m}{\zeta_0^m L_e} \tag{2.10}$$

$$\gamma_f^f = \frac{2G^f}{\zeta_0^f L_e} \tag{2.11}$$

The damage variables d_f and d_m serve as stiffness reduction factors for the various composite moduli,

$$E_{11} = \left(1-d_f\right)E_{11}^0 \tag{2.12}$$

$$E_{22} = \left(1-d_f\right)\left(1-d_m\right)E_{22}^0 \tag{2.13}$$

$$G_{12} = \left(1-d_f\right)\left(1-d_m\right)G_{12}^0 \tag{2.14}$$

In equations (2.12)-(2.14), the superscript 0 refers to the undamaged material properties while d_f and d_m are the degradation factor for fiber and matrix dominated damage. It should be noted that E_{33}, G_{13} and G_{23} are degraded also with the same manner as G_{12}.

In equations (2.4)-(2.7), the ε_{ij} and σ_{ij} values are all composite lamina strains and stresses. To estimate the energy dissipated at failure, the composite lamina strain and stress values are replaced with the failure strain and failure stress values. The ply strength (failure stress) values for G40-600/5245C are listed in Table 2.3.

Table 2.3. Ply strength properties

$X_t(MPa)$	$X_c(MPa)$	$Y_t(MPa)$	$Y_c(MPa)$	$S(MPa)$
2123	1351	35	35	67

Failure strain values are obtained using simple Hooke's law assuming the material response prior to failure is approximately linear. Afterwards, the energy dissipated in the composite after a total fiber failure is calibrated once using the unnotched strength value of the laminate.

Furthermore, to investigate the effect of progressive damage induced by static load on the modal parameters of notched composites, different levels of damage are introduced by imposing different ratios of displacement to failure values. After the quasi-static step, the composite specimen returns to its initial position while the bottom surface of the sample remains fixed before the definition of free vibration procedure. A subsequent frequency analysis step is defined considering the residual stiffness after such occurred damage. The equation of motion for free vibration of the composite plate is reduced to the eignenvalue problem below which forms the basis for calculating the natural frequencies

$$\left(\left[K^d\right]-\omega^2\left[M\right]\right)\{\delta\}=0 \qquad (2.15)$$

where $\left[K^d\right]$ is the damaged stiffness matrix, $[M]$ is the mass matrix and $\{\delta\}$ is the displacement vector.

2.4. Experimental procedure

All samples utilized in this work were fabricated using G40-600/5245C prepreg. Three different composite stacking sequences were utilized: $[+45_2/45_2]_s$, $[0/+45/-45/90]_s$ and $[90_2/0_2]_s$. Each sample was cut from laminates having a nominal width of 25.4mm and a nominal length of 127mm. For each stacking sequence, four notched samples and two unnotched samples were produced. In each of these notched samples, a center hole with a diameter of 6.35mm was introduced. Nine additional notched samples with the stacking sequence $[0/+45/-45/90]_s$ were constructed to examine the effect of hole size on the strength. In these samples, three different hole sizes were introduced: 3.175 mm, 6.35 mm and 9.525 mm diameter (Figure 2.5).

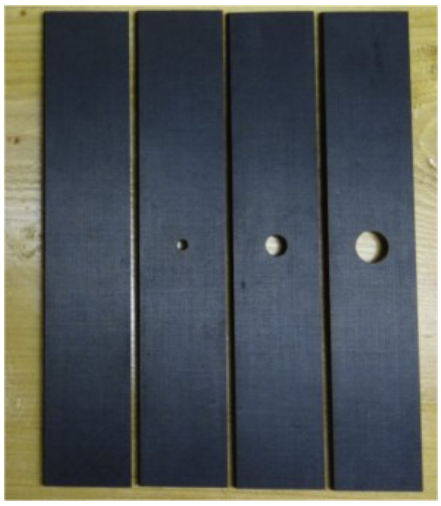

Figure 2.5. Different notch size in [0,+45,-45,90]s laminate

Tension testing was conducted using a 88kN load frame, run in displacement control at a rate of 0.0254 mm/s. Emery cloth was used to prevent slipping of the specimen in the grips. Load was measured using a 88kN load cell installed in the crosshead of the load frame. The Aramis Digital Image Correlation (DIC) system v6 by GOM was used in this work to obtain the full in-plane strain field on the outer ply of the laminate [36]. To do so, a 3D measurement setup was performed, using two cameras with 2 megapixel resolution each. Images are recorded in various load stages of the specimen. A fast measurement method was adopted to record temporal equidistant sequence of images with the rate of 6 frames per second. A shutter time of 5 ms was used. An analog channel was used to read the output voltage from load cell to relate each strain field computed with its relevant applied load. Prior to testing, the samples were painted first with black paint and then speckled with white paint to create a high contrast stochastic pattern as required for the DIC measurement (Figure 2.6).

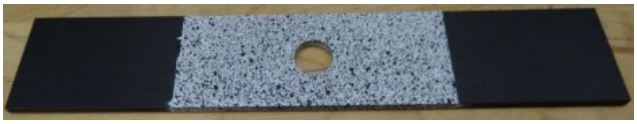

Figure 2.6. Speckled sample

During postprocessing, the deformation of the specimen is determined through the captured images by means of rectangular facets with size 15 x 15 pixels. The average intersection error of all 3D points of all samples is 0.05 pixels, less than the maximum recommended value of 0.1 [37].

2.5. Results

Experimental maximum tensile strengths were recorded for all unnotched and notched samples with different ply configurations and then averaged. These results are shown in Table 2.4 where σ^U and σ^N represent the unnotched and notched strength value of laminate, respectively.

Table 2.4. Averaged strength (MPa) of unnotched and notched samples

	$[+45_2/45_2]_s$	$[0/+45/-45/90]_s$	$[90_2/0_2]_s$
σ^U (MPa)	109.8	702.9	1086
σ^N (MPa)	80.46	527.83	825.65
σ_n	0.73	0.75	0.76

Strength retention is used as a normalized value that compares the tensile strength of different hole size samples to the tensile strength of the unnotched ones and is expressed as $\sigma_n = \frac{\sigma^N}{\sigma^U}$. Using the strength retention index, the effect of the notches on the tensile strength of the composite materials can be classified into three types: notch strengthening materials when $\sigma_n > 1$, notch weakening materials when $\sigma_n < 1$, and notch insensitivity materials when $\sigma_n = 1$. The maximum tensile strength, resulting from the FE analyses of models with different ply configurations, were extracted and compared to the averaged recorded experimental maximum tensile strength value of each ply configuration as shown in Table 2.5.

Table 2.5. Comparison between experiments and FE predictions of ultimate stress at failure

Layup	σ^N_{EXP} (MPa)	σ^N_{FEM} (MPa)	Error (%)
$[+45_2/45_2]_s$	80.46	83.03	-3.2%
$[0/+45/-45/90]_s$	527.83	512.7	2.86%
$[90_2/0_2]_s$	825.65	774.7	6.25%

Among the possible nondestructive techniques (thermography, scanning electron microscopy, acoustic emission, moiré interferometry and ultrasound) available to localize or identify the damage induced by mechanical loading in high gradient zones such as in notched composites, the DIC technique gives both good quantitative and qualitative information about the strain fields around the notch. Accordingly, DIC analysis was adopted in this study to determine the full field strain on the outer ply of the notched composite. The DIC strain contours for samples with a $[0/+45/-45/90]_s$ stacking sequence were compared to those predicted by FEA in Figure 2.7 and Figure 2.8.

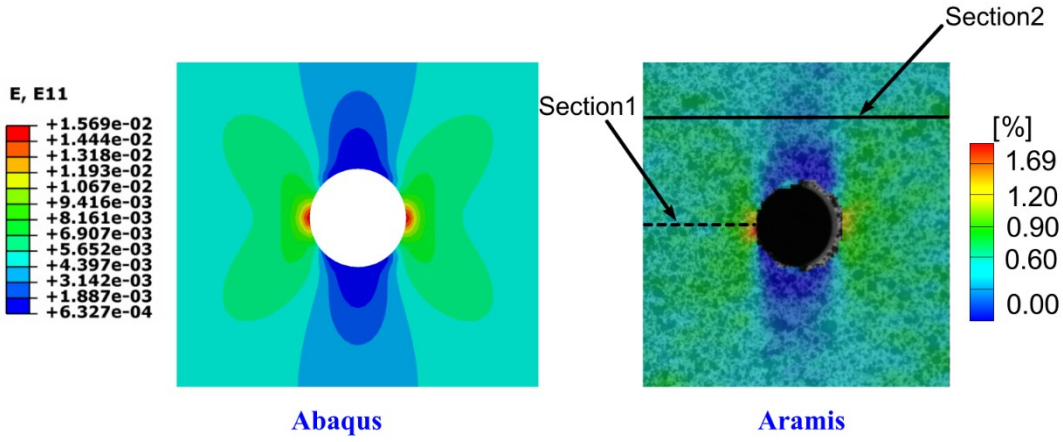

Figure 2.7. Correspondence of longitudinal strain contours obtained from FE and DIC results

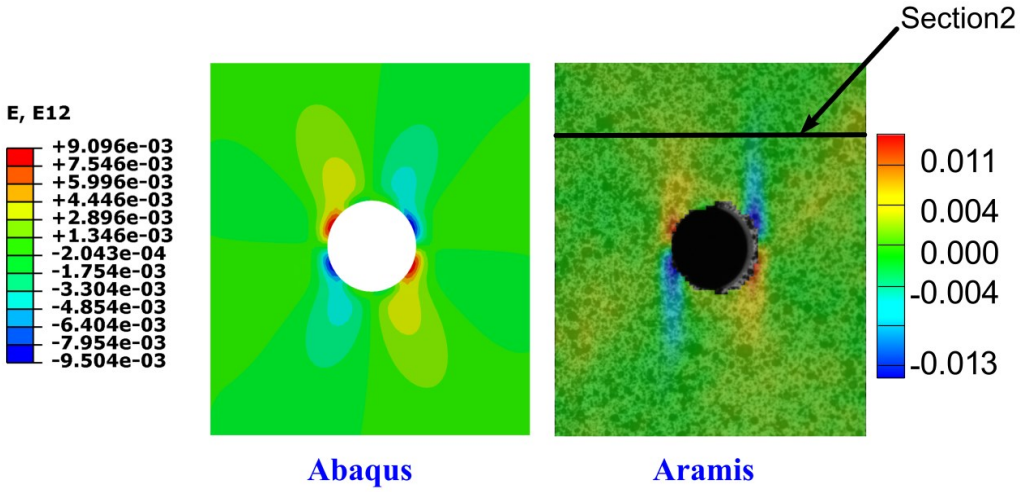

Figure 2.8. Correspondence of shear strain contours obtained from FE and DIC results

The measured and predicted contours for DIC and FEA compare well, with zones of maximum and minimum strain extending out from the hole. Figure 2.7 shows the longitudinal strain maps from the FEM and DIC techniques at the same load level (corresponding to 58% of the UTS). The characteristic butterfly shape is seen for the distribution of the strain gradients around the hole. The region of large strain concentration at the transverse edges of the hole is seen, as well as the regions of smaller strain around the longitudinal edges of the hole parallel to loading direction. Experimental strain values cannot be measured right at the edge of the hole. Figure 2.8 shows the contours of in-plane shear strain obtained from both methods. It can be noted that FEM and DIC contours appear qualitatively similar. High positive and negative shear strain strips parallel to load direction were observed on either side of the hole emanating from the four corners. For further comparison between DIC and 3D FEA results, axial and shear strains of both methods were plotted along selected section lines at two different load levels. The lengths of sections 1 and 2 are respectively equal to 8 mm and 19 mm. The strains were plotted as a function of the distance from the right extremity of the sections divided by their respective total lengths. The first load level is at 29% of the ultimate tensile strength (UTS) while the second level is at 58% of UTS. Figure 2.9 and Figure 2.10 show the development of longitudinal strain profiles along Section1 and Section 2, which are sketched on Figure 2.7, respectively.

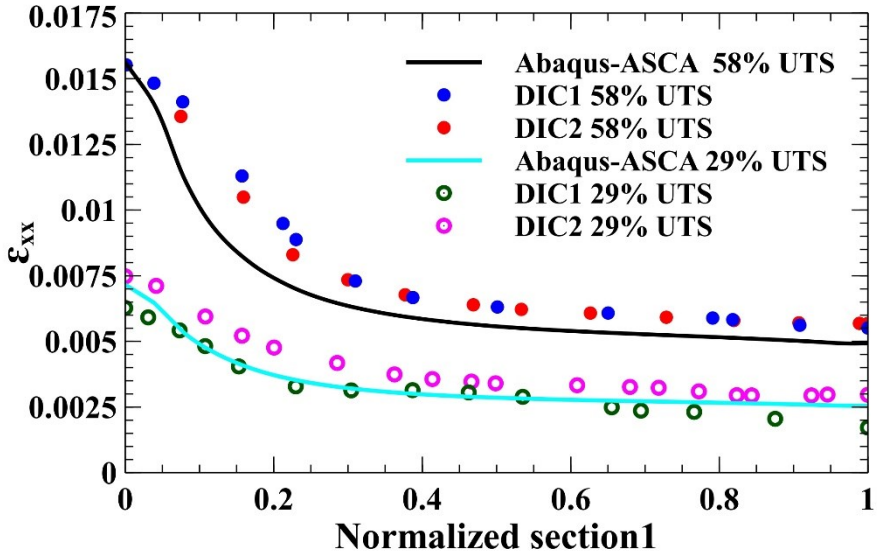

Figure 2.9. Longitudinal strain vs. normalized distance from the hole along Y-axis

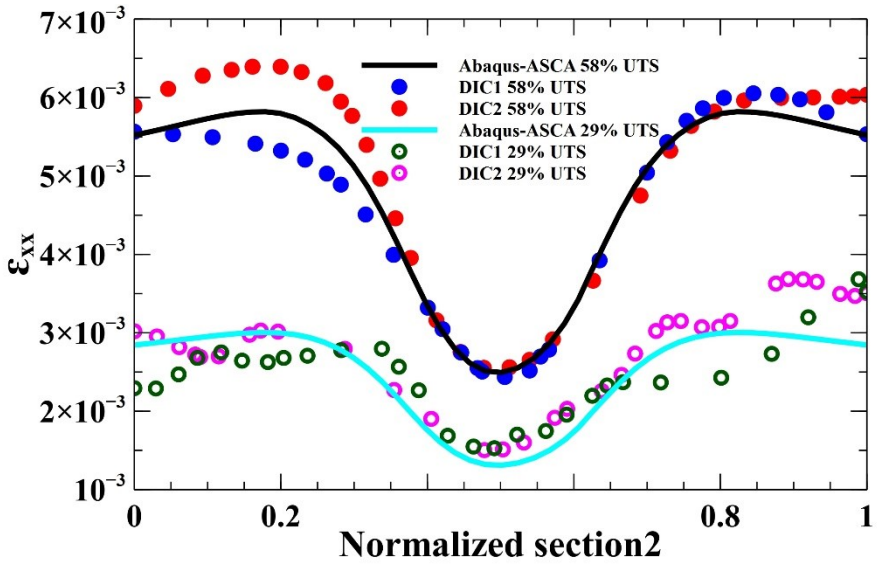

Figure 2.10. Longitudinal strain vs. normalized distance of section2 along Y-axis

Both figures represent two experimental curves of two different tests of the same layup at each level load. It can be observed from Figure 2.9 that the longitudinal strain is maximum around the hole and then tends to decrease as moving towards the specimen edge, as expected. The experimental and numerical results are in good agreement for both sections and load levels. Figure 2.11 shows the shear strain as a function of the normalized Section 2 at the second level of load. This figure depicts that the shear strain variation along Section 2 follows a spatially sinusoidal distribution. The DIC and FEA results are comparable for different strains with different locations and loads.

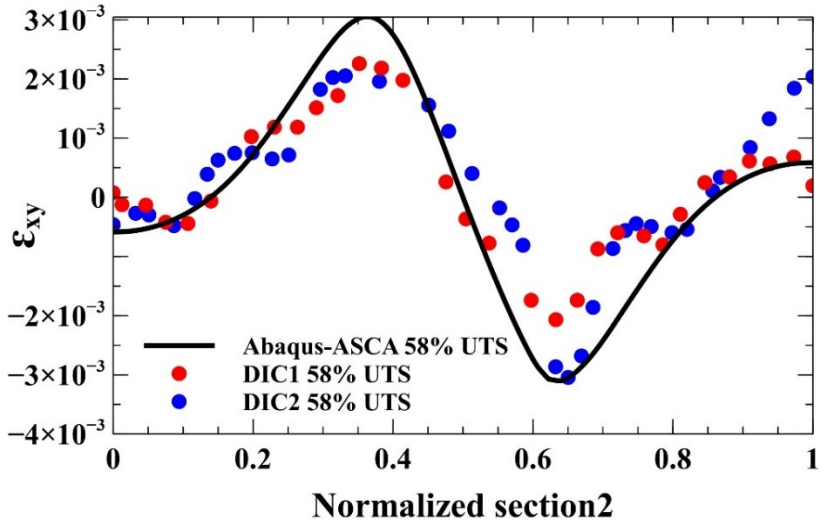

Figure 2.11. Shear strain vs. normalized distance of section2 along Y-axis

Figure 2.12 depicts the strength sensitivity to notch sizes. A decreasing of strength with increasing of diameter hole is observed. Since a good agreement is noticed between the predicted notched strength values and the experimental results for the quasi-isotropic laminate [0/+45/-45/90]s, the notch size effect on the strength for the other two layup configurations are determined numerically (see Figure 2.13).

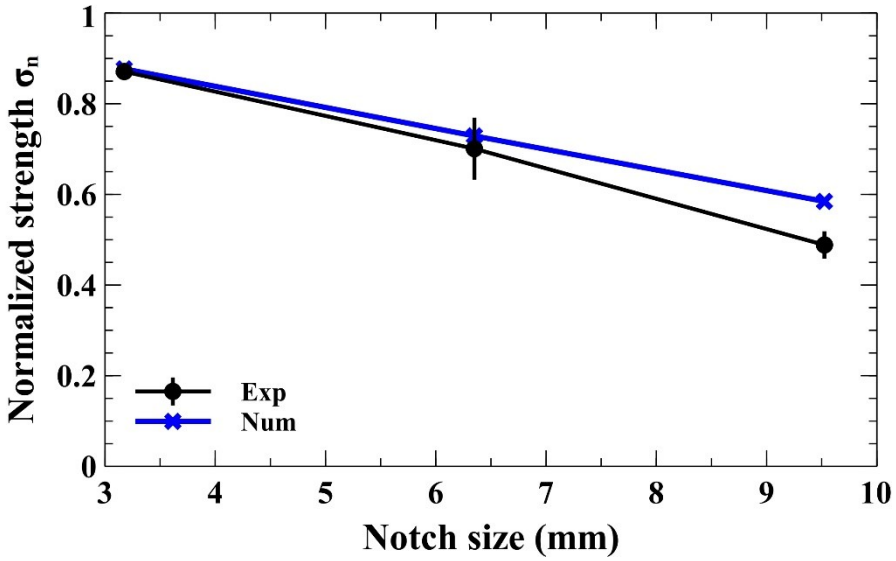

Figure 2.12. Notch size effect on strength

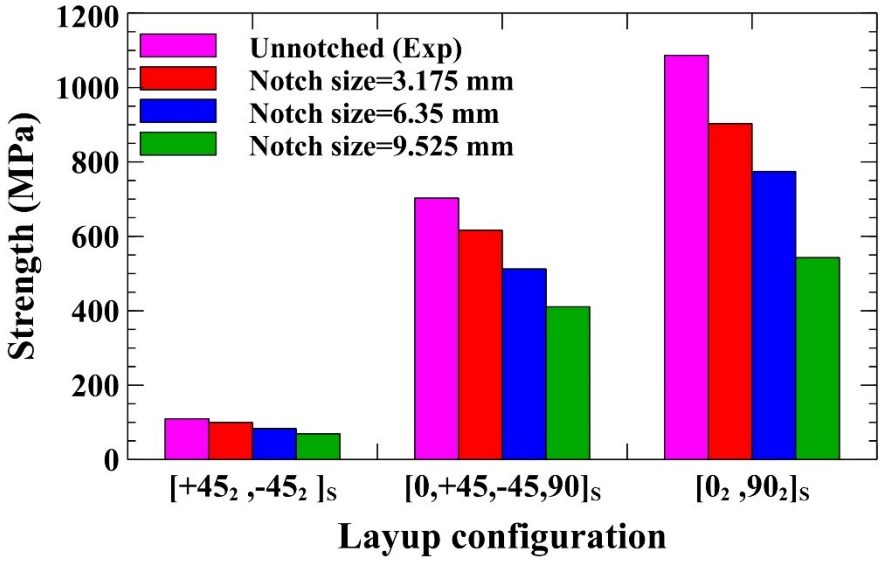

Figure 2.13. FE results of notch size effect on all layup configurations

ASCA generates two output state variables SDV1 and SDV2 that track the failure within matrix and fiber constituents. The meaning of different values for SDV1 is summarized in Table 2.6. SDV2 is a damage variable that ranges from 0 to 1 and is used to indicate the fraction of the matrix failure criterion that has been satisfied. A value of SDV2 equal to 0 implies that the matrix stress state is zero, while SDV2 equal to 1 implies that the matrix stress state has reached the failure level.

Table 2.6. SDV1 interpretation

SDV1 values	Composite damage state
1.0	Undamaged Matrix, Undamaged Fiber
2.0 : 2.92 2.96	Matrix Post-failure degradation level 1 : Matrix Post-failure degradation level 25 Failed matrix, undamaged fiber
3.0 : 3.92 3.96	Fiber Post-failure degradation level 1 : Fiber Post failure degradation level 25 Complete fiber failure

Figure 2.14 shows the matrix and fiber failure pattern in the three different layups. Figure 2.14**a** shows that just before global failure of the angle ply laminate ($[+45_2/45_2]_s$), matrix cracking along +45 and -45 directions was observed. Figure 2.14**b** shows a total fiber failure at the hole edges in the transverse direction as well as total matrix failure towards the free edges of the sample just before a global failure of the $[0/+45/-45/90]_s$ laminate. Figure 2.14**c** shows matrix splits parallel to the loading direction tangential to the hole boundary as well as the beginning of fiber failure at the hole edges in the transverse direction at the load level 58% of UTS for the $[0_2/90_2]$ laminate.

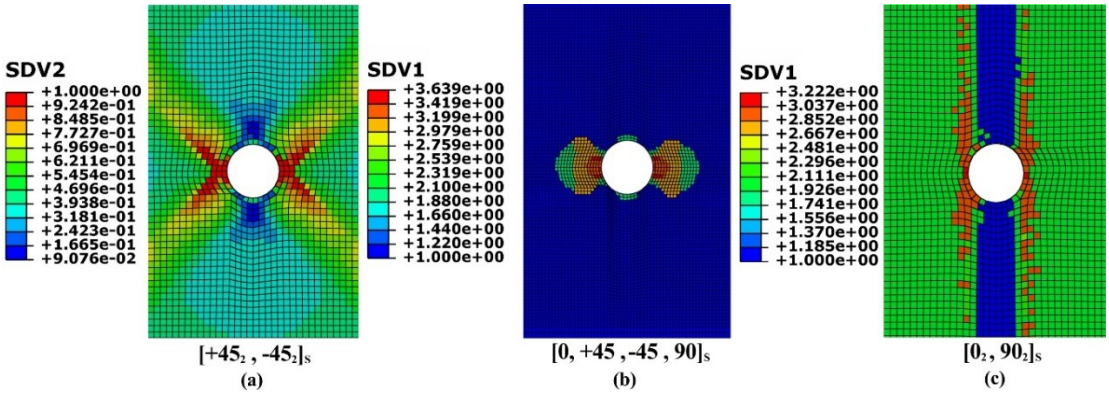

Figure 2.14. Failure pattern predicted by ASCA for different layup configurations

Stresses at the first matrix and fiber failure initiation events were recorded for all layup configurations in Table 2.7.

Table 2.7. Stress at first matrix and fiber failure initiation for different layup configurations

Lay-up	Stress at first matrix failure initiation	Stress at first fiber failure initiation
$[0/+45/-45/90]_s$	106 *MPa*	258 *MPa*
$[+45_2/45_2]_s$	61 *MPa*	80 *MPa*
$[90_2/0_2]_s$	64 *MPa*	308 *MPa*

The state variables at these failure events were plotted as a function of through thickness for quasi-isotropic layup (Figure 2.15 and Figure 2.16). The damage patterns for both failure initiation events were also shown along with the change of the state variable through thickness. The initiation of matrix failure was captured within the 90° plies as indicated when SDV2 reaches the value of 1 for the first time with increasing load. The envelope plot, which shows the maximum absolute value of the state variable across all of the plies in a layup for each element, has a similar pattern damage as the 90° ply plot. The fiber failure onset was captured within the outer 0° ply and indicated when SDV1 reaches the value of 3 for the first time with increasing load. The envelope plot at this load stage shows more matrix damage in the interior plies compared to the outer ply. This is expected since the 90° and 45° exhibit more matrix degradation at early load stages.

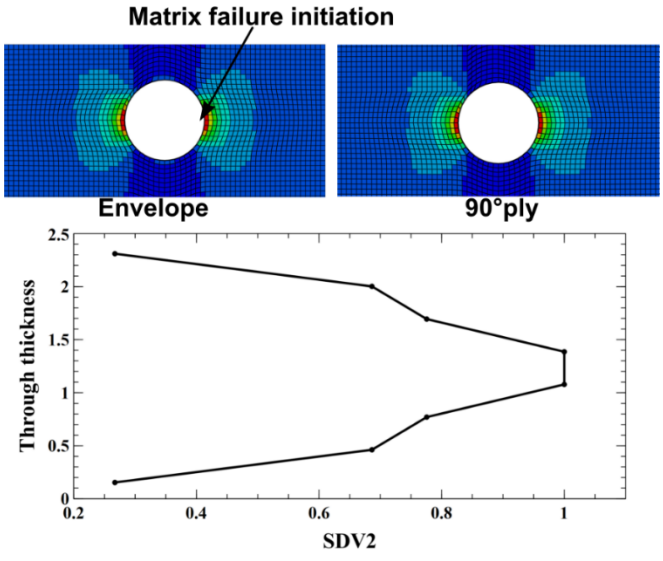

Figure 2.15. Matrix Failure initiation event and representation of SDV2 through thickness

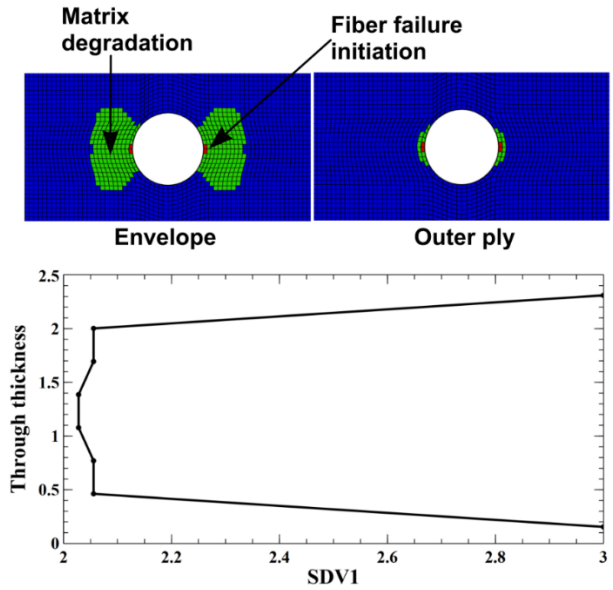

Figure 2.16. Fiber failure initiation event and representation of SDV2 through thickness

Furthermore, a modal analysis of the notched composite was conducted to approximate its dominant frequencies and associated mode shapes using the FEM discretized model. The main motivation behind this modal analysis is to check how the dominant frequencies and associated mode shapes are altered if a damage is introduced by a static loading. Changes in frequencies can be considered as potential indicator of damage severity. Table 2.8 displays the natural frequencies of undamaged notched composites and damaged notched composites with different severities corresponding to 0.1, 0.3 and 0.6 mm of imposed displacement.

Table 2.8. Frequency deviation of composite under different imposed displacements

Imposed displacement (mm)	**0**	**0.1**	**0.3**	**0.6**
Mode 1 (First bending) (Hz)	251	250.5	250.4	249.7
Mode 2 (First torsion) (Hz)	993	992	991	981
Mode 3 (Second bending) (Hz)	1319	1317	1315	1309
Mode 4 (First in-plane bending) (Hz)	1805	1751	1736.5	1661
Mode 5 (Second torsion) (Hz)	3107	3104	3099	3068
Mode 6 (Third bending) (Hz)	3225	3221	3217	3192
Mode 7 (Third torsion) (Hz)	5524	5519	5509	5441
Mode 8 (Fourth bending) (Hz)	5800	5793	5784	5720

Figure 2.17 shows the first eight relevant mode shapes. The results show that the fundamental frequency is not sensitive to the different levels of static loadings: the deviation from the undamaged value is less than 2 Hz. However, the fourth mode which represents the first in-plane bending mode seems to be a good candidate for evaluating damage level. In fact for the first eight modes examined, the fourth mode shows the largest deviation with respect to the undamaged natural frequency value for all levels of static loading.

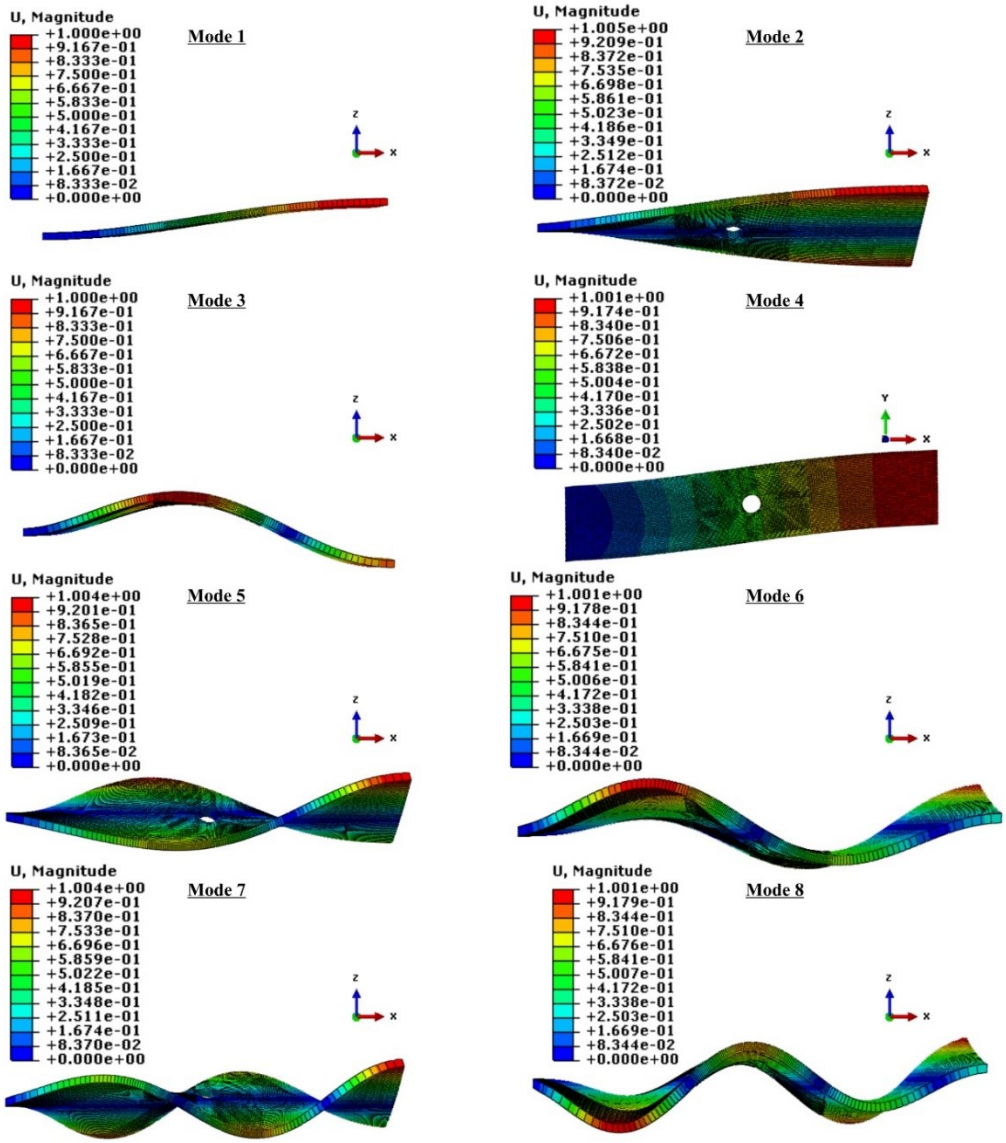

Figure 2.17. Mode shapes

2.6. Conclusion

A finite element model developed in this paper utilizing the energy-based degradation scheme is used to predict the strength of notched composites. The resulting strengths are within 3% to 6% of the experimental observed values for three different stacking sequences (angle-ply, cross-ply, and quasi-isotropic) requiring only the elastic and strength ply properties and the dissipation energies for matrix and fiber failures. The Autodesk Simulation Composite Analysis (ASCA) is used in conjunction with Abaqus to implement the processes of progressive failure and load redistribution via a user-defined material subroutine. An energy-based degradation analysis was conducted to account for residual load carrying capability of initially damaged coupons after a failure criterion is satisfied. Quasi-static tensile experiments are conducted in which digital image correlation (DIC) is used to extract strain field data for subsequent comparison to the finite element results. Therefore, qualitative and quantitative comparison of strain distribution of both FEM and DIC methods are presented. A good agreement between the numerical and experimental strain profiles is observed.

As an example of further application of the model, the sensitivity of notched strength to hole diameter is studied. In addition to the expected decrease in strength with increasing hole size, quantitative predictions for the strength are obtained.

The model is capable of computing the degraded composite and constituent properties as a function of increasing strain, after the initiation of failure event within matrix or fiber constituents is captured using MCT. As a result, a modal analysis is conducted to assess the effect of different imposed displacements and their relevant damage states on the first eight natural frequencies. The first in-plane mode is selected to be a good candidate of tracking damage level.

It should be noted that the developed finite element model is applicable to notched composite laminates that exhibit either brittle or pull-out failure modes. The strength prediction of laminates whose main failure mechanism is delamination requires appropriate finite element analysis; the model proposed herein is not appropriate in this case. Future work will address the generalization of the model to deal with such type of failures.

Chapter 3. Experimental and numerical monitoring of strain gradients in notched composites under tension loading

3.1. Abstract

Experimental tensile tests have been carried out to investigate the effect of progressive damage within notched, quasi-isotropic T650/F584 carbon fiber/epoxy laminates on the strain distribution in the vicinity of the notch. Three-dimensional Digital image correlation was used during quasi-static tests to obtain the distribution of strains as a function of applied stress. A finite element model was developed using Abaqus and Digimat in which Digimat was used to implement the damage evolution model via a user-defined material subroutine. Damage initiation has been assessed using Hashin's failure criteria and Matzenmiller model was adopted for damage evolution. Numerical and experimental strain results were presented and compared for different section lines on the outer surface of the laminate at different load stages. The experimental notched composite strength was compared as well with the predicted one from finite element solution.

3.2. Introduction

The use of fiber reinforced polymer matrix composites in a wide range of applications in various industries has significantly increased in the last several years. For example, composites make up approximately 16% of the total A380 airframe weight, representing a replacement of 20% of the conventional aluminum structures by composites [38]. The rapid growth in use of composites is explained by their prominent characteristics: high strength and stiffness to weight ratios, flexible fabrication shapes, and resistance to environmental corrosion.

The use of composites in load-bearing structures may necessitate including geometric discontinuities in order to satisfy design specifications. Therefore, there is a need to quantitatively describe the mechanical behavior of composite structures containing stress raisers such as notches. However, the damage mechanisms and failure modes of composites which contain notches are more complex than those occurring in unnotched laminates because of the discontinuities and their associated stress gradients. In fact, the existence of high gradient stresses regions around the hole boundary leads to the occurrence of different damage mechanisms such as transverse matrix cracks, axial splitting and delamination between adjacent layers in the vicinity of hole boundary that contribute to the relief of the stress concentration localized at the hole [13]. The sequence, severity, extent and interaction of damage mechanisms depend on many factors such as notch size, geometry, laminate thickness, block ply thickness, layup sequence and load configurations [14, 15]. As a consequence, these parameters affect the ultimate strength of such notched composites. Classical analytical models are adopted for the prediction of notched composite strength as faster prediction methods. These models rely on the analysis of the stress distribution near the notch or on the use of linear elastic fracture mechanics. As an example, the early and widely used model is the point stress criterion (PSC) developed by Whitney and Nuismer [18] assumes that fracture occurs when the tensile stress reaches the unnotched strength at a certain critical distance from the notch. The earliest energetic model was developed by Waddoups et al. [19]; it predicts that fracture occurs if the energy release rate for an equivalent characteristic length reaches the material toughness G_c. Martin et al. [20] developed an improved PSC criterion that combines strength and energy approaches and geometry parameters (hole size and plate width) to determine the strength of notched composites. Moreover, various numerical models based on finite elements analysis have been developed either to determine the ultimate tensile strength and/or to capture the failure mechanisms. These models are often based on cohesive zone approaches that require the use of critical energy release rates for mode I (opening) and mode II (shear) and predefined paths of cohesive interface elements. These cohesive zone models simulate the intra-ply splitting and the inter-ply delamination [21, 22]. These latter models were improved by predicting arbitrary matrix cracking trajectories without the need pre-knowledge of crack path from experiments. This is implemented by the use of XFEM through the phantom node method [7].

Experimental techniques that have been used to assess the performance of composites containing stress concentration raisers include infrared thermography, ultrasonic C-scanning, X-ray

radiography and digital image correlation (DIC). However, there are few studies that used DIC to characterize the damage progression in notched composites during tensile loading. Caminero et al. [39] used DIC to assess the damage taking place in open-hole composites loaded in tension. They showed that the high localized strains identified by the DIC technique were related to the damage modes identified by penetrant enhanced X-ray radiography. Kashfuddoja and Ramji [40] used DIC technique to analyze the behavior of notched and repaired composites under tensile loading. Damage initiation and propagation in notched and repaired composites were studied using DIC. A 3-D finite element analysis was carried out and the numerical strain profiles were compared to the experimental results. The results seem to have similar trends. However, the predicted magnitude of the longitudinal strain was 36% lower than the experimental value for the considered range.

The current work focuses on the use of digital image correlation technique and its capability of tracking the strain redistribution during loading notched composites. In addition, a finite element model was constructed within Abaqus 6.13 and the Matzenmiller damage model was implemented as a user material subroutine through Digimat 5.1.1. The results obtained from both methods are presented and compared qualitatively and quantitatively. Full-field strain contours and strain profiles at different selected transverse sections of the outer ply of the laminate from both methods were compared.

3.3. Experimental procedure

Quasi-isotropic laminates [0°/-45°/+45°/90°]S were made from carbon fiber epoxy Hexcel T650/F584 prepreg.. This unidirectional prepreg system has a nominal ply thickness equal to 0.314 mm. The laminates were cured according to the cure cycle specifications suggested by Hexcel [13]. Specimens were then machined using a water cooled diamond saw and the holes were drilled using a tungsten carbide bits. Each specimen has a nominal thickness of 2.512 mm, width of 25.4 mm and gauge length of 69 mm and a central hole of diameter 6.35 mm.

Quasi static tests were performed on both unnotched and notched composites using a 88 kN MTS frame with hydraulic grips. The load-frame servo-valves were controlled by MTS 407 controller through a Labview program and a DAQ card. Digital image correlation was used to obtain the full in-plane strain field on the outer ply of the laminate of each quasi-static test. Stainless steel mesh cloth (100x100 mesh size) was used to prevent slipping of the unnotched

specimens in the grips and fracture at the gripped region. The mesh cloth was not used for the notched samples as failure tends to occur around the central notch. The 3D-DIC setup consists of two megapixel cameras coupled with Nikon lenses of 35 mm focal length. Prior to the testing, specimen were painted with white and then speckled with black paint. Uniform illumination of specimen surface is ensured by the use of two white led lights. Cameras are then calibrated for their actual position and orientation using an appropriate calibration grid plate for the typical region of interest (ROI) in the tested specimen. Ten images per second are captured using Vic-Snap software (Correlated Solutions, Inc.) during tests. VIC-3D software supplied by Correlated Solutions, Inc. is used for post-processing of the captured images. The ROI is selected on initial image (no load or reference image) and appropriate subset and step sizes are specified for post-processing

3.4. Numerical Modeling

A linear static 3D finite element analysis of notched composite is conducted using Abaqus 6.13 software and Digimat 5.1.1 software. An open hole tension plate from T650/F584 composite is built within Abaqus/CAE. The model was meshed with S4R 4 nodes quadrilateral shell elements with reduced integration. The mesh was tailored to allow rapid model runtime by specifying a fine and regular mesh around the notch and a progressively coarser mesh away from the hole. Elastic properties, damage initiation and damage evolution law material properties were implemented as UMAT subroutine created within Digimat [41]. The sample is fixed at the bottom and undergoes an imposed displacement at its top surface. The current work is based on Hashin failure criteria as damage initiation criteria and the Matzenmiller [6] approach as a damage evolution law. In this model four different modes of failure were considered, namely, fiber rupture in tension, fiber buckling and kinking in compression, matrix cracking under transverse tension, and shearing and matrix cracking under transverse compression and shear. The failure initiation criteria for the above mode of failures should satisfy the following general forms:

$$f_A = \frac{\sigma_{11}^2}{X_t^2} + \frac{\tau_{12}^2}{S_t^2} \quad \text{if } \sigma_{11} \geq 0 \tag{3.1}$$

$$f_B = \frac{\sigma_{11}^2}{Y_c^2} \quad \text{if} \sigma_{11} < 0 \tag{3.2}$$

$$f_C = \frac{\sigma_{22}^2}{Y_t^2} + \frac{\tau_{12}^2}{S_l^2} \text{ if } \sigma_{22} \geq 0 \tag{3.3}$$

$$f_D = \frac{\sigma_{22}^2}{4S_t^2} + \frac{\tau_{12}^2}{S_l^2} + \left[\left(\frac{Y^c}{2S_t} \right)^2 - 1 \right] \text{ if } \sigma_{22} < 0 \tag{3.4}$$

where X_t and X_c are the longitudinal and compressive strengths respectively,

Y_t and Y_c are the longitudinal and compressive strengths respectively,

S_l and S_t are the longitudinal and transverse shear strengths respectively, and

σ_{11}, σ_{22} and τ_{12} are components of the effective stress tensor σ that is used to evaluate the initiation criteria.

The response of the material during the post-damage initiation phase requires the definition of Hashin failure indicators and the damage variables are computed as:

$$D_{11} = \varphi\left(\max\{f_A, f_B\}\right) \tag{3.5}$$

$$D_{22} = \varphi\left(\max\{f_C, f_D\}\right) \tag{3.6}$$

$$D_{12} = 1-(1-D_{11})(1-D_{22}) \tag{3.7}$$

$$D_{33} = D_{13} = D_{23} = 0 \tag{3.8}$$

where the function φ for instantaneous degradation and linear softening damage laws respectively

$$\varphi(f) = \begin{cases} 0 & \textit{if } f < f_{\min} \\ D_{\max} & \textit{otherwise} \end{cases} \tag{3.9}$$

$$\varphi(f) = \begin{cases} 0 & \textit{if } f < f_{\min} \\ D_{\max} \times \dfrac{f_{\max}}{f} \times \dfrac{f - f_{\min}}{f_{\max} - f_{\min}} & \textit{if } f_{\min} \leq f < f_{\max} \\ D_{\max} & \textit{otherwise} \end{cases} \tag{3.10}$$

$D_{\max}$, $f_{\min}$ and $f_{\max}$ were chosen to be equal to 0.99, 1 and 2 respectively. $D_{\max}$ represents the maximum damage parameter that enables to threshold all the damage variables. This parameter enables to limit the damage without changing the damage evolution law parameters. $D_{\max}$ should be left to 1 in order to enable a complete damaging of the material. However, it is recommended to use a value slightly below 1 to avoid convergence issues. $f_{\min}$ should be left to 1 according to the definition of failure initiation criteria unless a lower value is wanted to trigger earlier damage evolution. The choice of $f_{\max}$ equal to 2 for the linear softening damage evolution law along with

$f_{\min} = 1$ and $D_{\max} = 0.99$ results in a bilinear-shaped stress-strain curve where the final strain at failure is the double of strain at damage initiation.

These damage variables are used with a Matzenmiller's 2-D progressive failure model and the damage compliance is computed in the principal material coordinate system axis by changing the diagonal terms of the undamaged compliance $\hat{S}$, as follows,

$$S(D) = \begin{bmatrix} \frac{\hat{S}_{1111}}{1-D_{11}} & \hat{S}_{1122} & \hat{S}_{1133} & 0 & 0 & 0 \\ & \frac{\hat{S}_{2222}}{1-D_{22}} & \hat{S}_{2233} & 0 & 0 & 0 \\ & & \frac{\hat{S}_{3333}}{1-D_{33}} & 0 & 0 & 0 \\ & & & \frac{\hat{S}_{1212}}{1-D_{12}} & 0 & 0 \\ & Sym. & & & \frac{\hat{S}_{2323}}{1-D_{23}} & 0 \\ & & & & & \frac{\hat{S}_{1313}}{1-D_{13}} \end{bmatrix} \tag{3.11}$$

An important consequence of this choice is that, in agreement with experimental observations, the apparent Poisson's ratios evolves when damage occurs:

$$\nu_{12} = -\frac{\varepsilon_{22}}{\varepsilon_{11}} = \frac{S_{1122}}{S_{1111}} = \frac{\hat{S}_{1122}}{\hat{S}_{1111}}(1-D_{11}) \neq \hat{\nu}_{12} \tag{3.12}$$

The properties of the material, T650/F5845C, used in this work and implemented through Digimat are given in Table 3.1 [24]. The ply strength values used in failure criteria for this material are listed in

Table 3.2.

Table 3.1. T650/F485 Ply elastic properties

$E_1(GPa)$	$E_2(GPa)$	$G_{12}(GPa)$	$G_{23}(GPa)$	ν_{12}	ν_{23}
153.67	9.49	4.26	3.44	0.295	0.381

Table 3.2. Ply strength properties

$X_t(MPa)$	$X_c(MPa)$	$Y_t(MPa)$	$Y_c(MPa)$	$S(MPa)$
2337	1585	46.6	46.6	126.9

3.5. Results and Discussion

Five unnotched and notched specimens were all tested in tension with DIC measurements conducted. The DIC technique was used to obtain the full-field strain on the outer layer of the laminate. During the DIC post-processing, a virtual extensometer (a tool within Vic3D software) with a 25.4 mm gauge length centered over the hole. The averaged notched strength UTS σ^N, stiffness E_0 and maximum strain to failure $\varepsilon_{\max f}$ values were determined to be 393 MPa, 37.74 GPa and 1.07% respectively, with coefficients of variation 2.9%, 2.33%, and 5%, respectively. The unnotched tensile strength of the laminate σ^U, was also measured using five test specimens and the average value obtained was 581.35 MPa with a coefficient of variation of 4.7%.

In addition, the finite element model built using Abaqus and Digimat was used to predict the ultimate tensile strength (UTS) of the notched composites. For instantaneous and linear softening degradation approaches, the calculated values of UTS are equal to 392.8 MPa and 393.3 MPa, respectively. The percentage errors for both methods are equal to 0.14% and 0.02%. Thus, the numerical results are in very good agreement with the average experimental values. We also not that the predicted notched strengths are insensitive to the softening approach used. Furthermore, the contour plots of strains ε_{yy} and ε_{xy} obtained from FEM and DIC are presented for qualitative comparison. Figure 3.1 shows the longitudinal strain maps from the FEM and DIC techniques at the same load level (corresponding to 80% of the UTS). The characteristic butterfly shape is seen for the distribution of the strain gradients around the hole. The region of large strain concentration at the transverse edges of the hole is seen, as well as the regions of smaller strain around the longitudinal edges of the hole parallel to loading direction. The grey area in FEM contour represents the strain values beyond the fixed limit which is set equal to the maximum strain value observed by DIC. Experimental strain values cannot be achieved in the immediate vicinity of the

hole. The FEM results indicate that the magnitude of longitudinal strain in the vicinity of the hole is very high (more than two times the maximum strain captured by DIC).

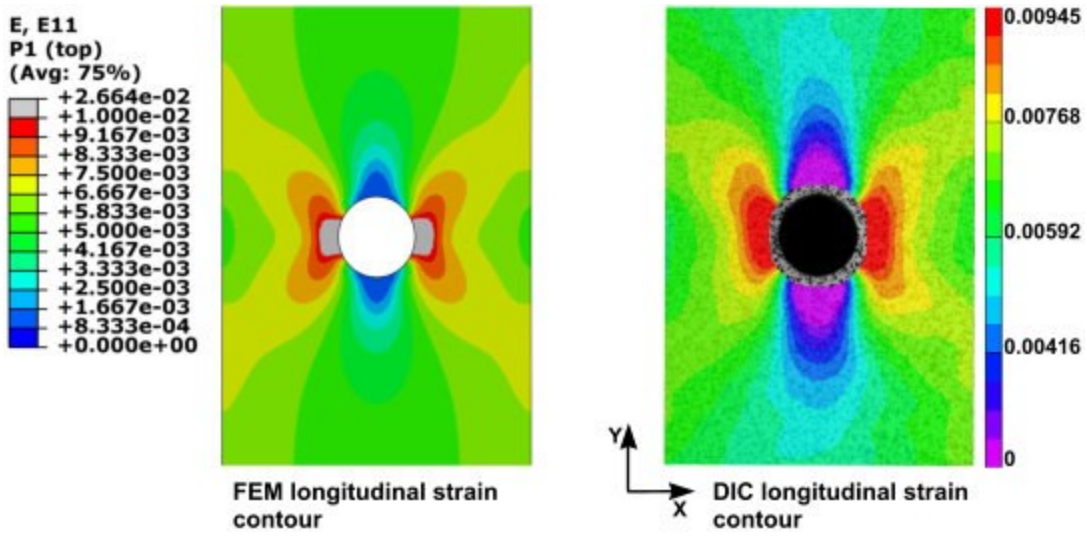

Figure 3.1. Comparison of longitudinal strain contours obtained by FEM and DIC methods

Figure 3.2 shows the contours of in-plane shear strain obtained from both methods. It can be noted that FEM and DIC contours look qualitatively similar. High positive and negative shear strain strips parallel to load direction were observed on either side of the hole emanating from the four corners. Lateral antisymmetric concentrated shear strain zones were observed in the ±45° directions in the FEM contour. The DIC was able to capture these zones very well in the appropriate directions in the right side of the hole whereas on the left side of the hole, these zones are not as discernible and aligned with respect to the ±45° directions.

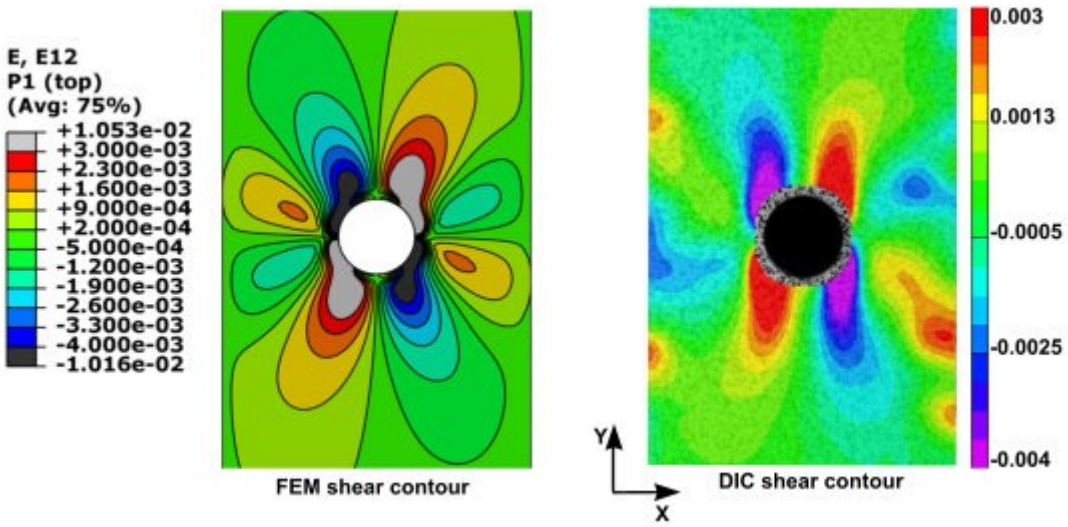

Figure 3.2. Comparison of shear strain contours obtained by FEM and DIC methods

In addition, longitudinal, transverse, and shear strain profiles at two predefined sections were determined. Figure 3.3 shows the strain profiles at the sketched sections at various load stages of one specimen. Figure 3.4 shows the variation of ε_{yy} along section1 at four load levels 20% , 40%, 60% and 80% UTS. It can be observed from the plots that the longitudinal strain is maximum around the hole and then tends to decrease as moving towards the specimen edge. The maximum percentage difference between the predicted results by FEM and the experimental results is equal to 28% and is captured at the high level load 80%UTS. The longitudinal strain distributions at section1 from both methods have a similar trend. The numerical and experimental curves tend to approach at certain distance near from the hole. Figure 3.5 shows the shear strain profiles at section 2 at the load levels 20%, 40%, 60% and 80% UTS. This figure depicts that the shear strain variation along section2 follows a spatial sinusoidal distribution. Both DIC and FEM shear strain profiles at different load stages show a very good agreement, in contrast to the differences in the longitudinal strain profiles.

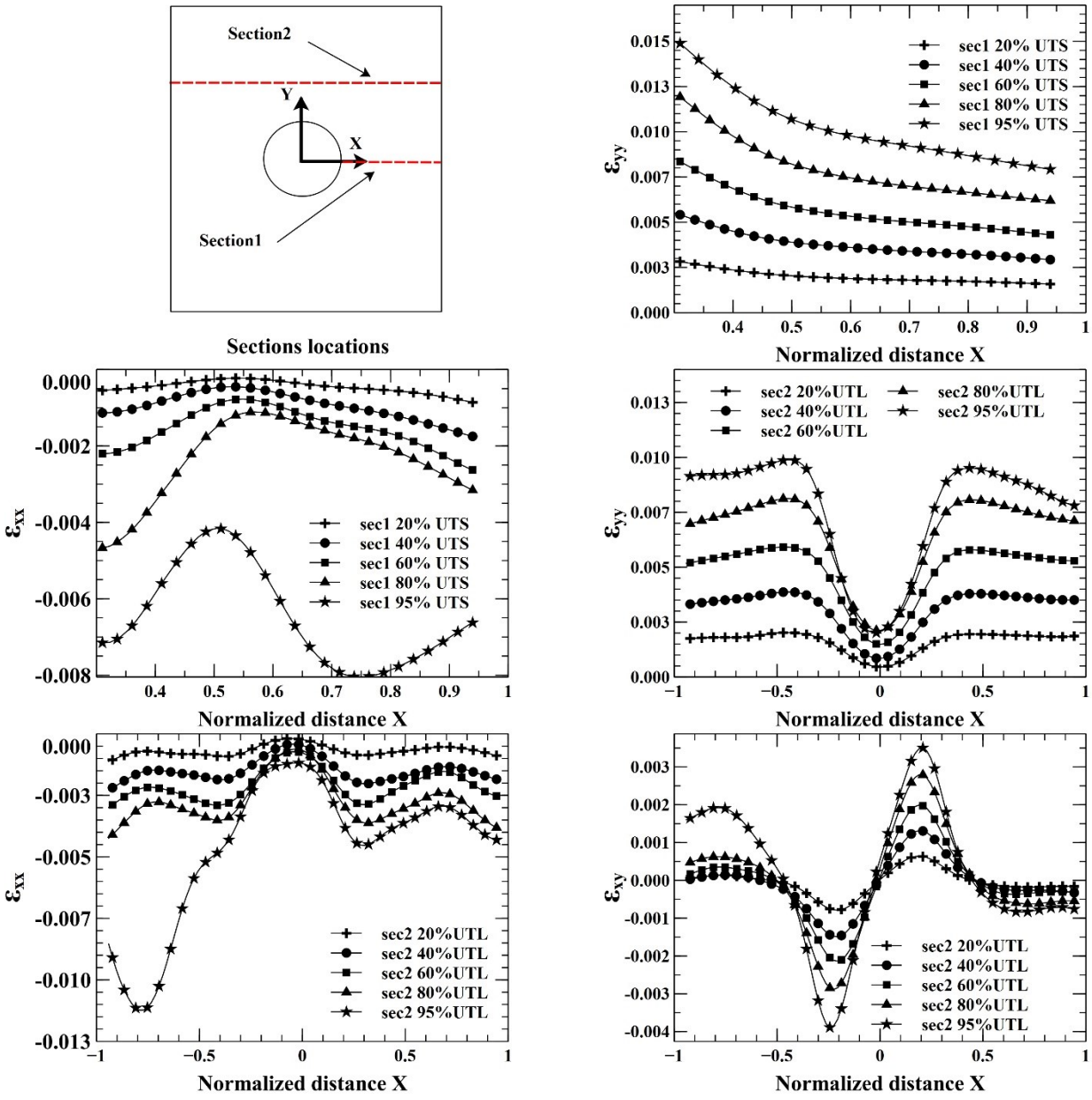

Figure 3.3. Strain profiles at different sections and load stages

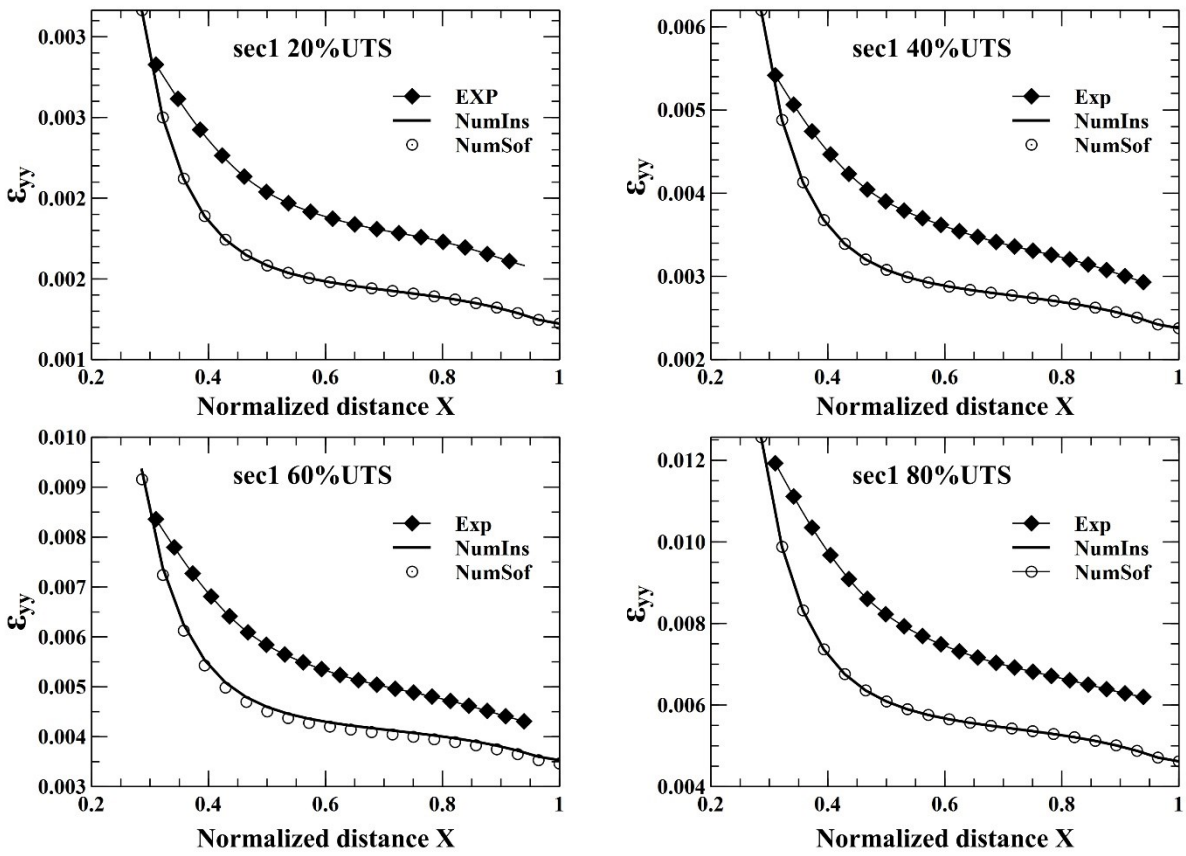

Figure 3.4. Longitudinal strain profiles at section1 at 20%, 40%, 60% and 80% UTS load levels

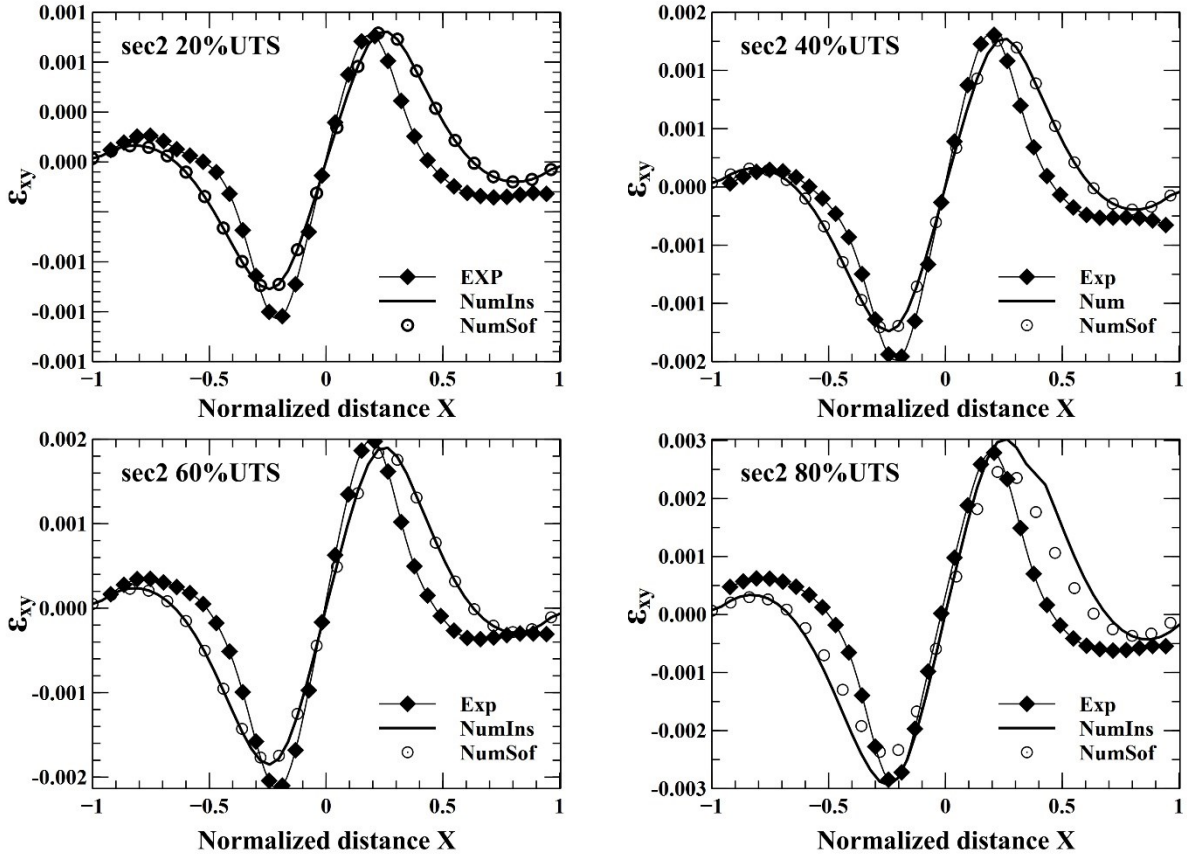

Figure 3.5. Shear strain profiles at section1 at 20%, 40%, 60% and 80% UTS load levels

3.6. Conclusions

Quasi-static tension tests were performed on notched quasi-isotropic composites using digital image correlation (DIC) to determine the full field strain contours on the outer layer of the laminates. Then a finite element model was built within Abaqus for comparison. A user material subroutine containing Hashin's damage initiation criteria and Matzenmiller's damage evolution laws was implemented by Digimat. The finite element model was able to predict the ultimate tensile strength using only the elastic and strength ply properties without any calibration needed with a maximum percentage error of 0.12%.

Full-field strain variations obtained from the DIC technique were compared with finite element results. For further comparison, experimental results of the various strain components at different section lines using digital image correlation were compared to the predicted results. The

comparison confirmed the consistency of localized and full field strains determined by DIC. These localized highly strained zones captured by DIC are good indicators of damage development. The measured in-plane shear strain profiles were in good with the measured ones. However, considerable discrepancies were seen in the longitudinal strain profiles.

Chapter 4. Progressive damage assessment of centrally notched composites in fatigue

4.1. Abstract

The aim of this study is to assess the residual properties and the corresponding damage states within centrally notched quasi-isotropic $[0/-45/+45/90]_S$ T650/F584 (Hexcel) carbon-fiber/epoxy composites subjected to fatigue loading using Digital Image Correlation (DIC), radiography, and a non-contact vibration measurement technique. Quasi-static tests were performed on virgin samples using DIC to determine the full-field in-plane strains at different applied load levels. Fatigue tests were interrupted during the fatigue lifetimes in order to perform quasi-static tests with DIC measurements. Non-contact vibration measurements were performed to investigate the effect of fatigue damage on residual frequency responses. X-ray computed tomography was used to determine the type, location, and extent of fatigue damage development. The results provide an important step in the validation of DIC and vibration response as a powerful combined non-destructive evaluation tool for monitoring the development of fatigue damage as well as predicting the damage level of notched composite materials.

4.2. Introduction

The increased and extended use of fiber reinforced composite materials in aerospace, submarine, wind turbine, automotive, civil engineering structures and other applications, can be attributed to the myriad of advantages these materials provide compared to isotropic materials such as steel, aluminum, concrete and even anisotropic wood. Indeed, fiber reinforced composite materials are characterized by high stiffness and strength with relative light weight, corrosion resistance and excellent fatigue properties. Although composite materials are expected to have excellent fatigue lifetimes especially when compared to metallic materials, researchers must consider fatigue as a crucial aspect in performance calculations during design processes, particularly for structures that undergo cyclic loading during their service time. The anisotropic nature of FRP composite materials renders their experimental fatigue damage characterization a complicated task since these materials exhibit different damage modes at different locations at the same time. The

principal types of damage that can be developed during fatigue life are matrix cracks, delamination, matrix and fiber debonding and fiber breakage [4, 42, 43]. In addition, the interaction between these failure modes contributes significantly to the complexity of the damage characterization task. Moreover, the multitude of material configurations resulting from the variability of fibers, matrices, manufacturing methods, lamination stacking sequences and geometries makes the development of a commonly accepted method to cover all these variations difficult [44].

Several experimental techniques have been used to obtain valuable information on the micro-structural level as well as on the macro-structural level damage development during fatigue loading. Nevertheless, each work has been focused in one or more aspects for studying fatigue damage effects on composite material during its fatigue lifetime. Early fatigue studies used many non-destructive techniques for the identification of damage patterns on the surface of and also inside fatigued composite materials. The most common methods used were X-rays, acoustic emission, surface observation during fatigue loading or post mortem observation using scanning electron microscope, ultrasounds and surface replicas [45-49]. However, the generally accelerated enhancement of the hardware (mechanical and electronic aspects), the software (Data processing and display) and the development of modern embedded systems lead to a significant improvement of the results obtained by the aforementioned techniques and the development of new other techniques. For instance, recent advances in digital photography and computer technology have led to the development of digital image correlation (DIC) as an effective non-contact method of measuring deformation.

Davi et al. [50] have combined different techniques to analyze fatigue damage mechanisms of a woven hemp fiber reinforced epoxy composites for two different stacking sequences ($[0/90]_7$ and $[\pm 45]_7$): optical microscopy, X-ray micro-tomography observations, temperature field measurement by infrared camera and acoustic emission monitoring. All these techniques permitted a complete description of damage mechanisms developing in these hemp/epoxy composites. Ihab et al. [51] used infrared (IR) thermography to build a simple predictive model of fatigue life in two configurations of flax/epoxy composites layup ($[0]_{16}$ and $[\pm 45]_{4S}$) by establishing a direct correlation between the temperature increase and the number of cycles to failure at the same stress level . They also used SEM to monitor crack density for a stress level at different damage stages. In the case of $[0]_{16}$ laminates, the dynamic modulus was found to increase with increasing number of cycles. This hardening behavior has been observed exclusively in flax/epoxy composite

laminate that have plant-based fibers. Montesano et al. [52] also used infrared thermography technique to determine the stress-life curve and the fatigue threshold of a triaxially braided carbon fiber composite material. They established a direct correlation between the increase in temperature at stabilization, the intrinsic dissipation energy (hysteresis) and the number of cycles to failure. Other studies based on infrared thermographic techniques (passive and active approaches) are carried out to characterize the fatigue damage of CFRP composites [53, 54].

Dattoma and Giancane [55] evaluated fatigue damage from a theoretical viewpoint of energy balance during the test by evaluating the hysteresis area, dissipated and accumulated heat and then calculating the fatigue damage energy. Their work was performed on double notched specimen made from E-glass/epoxy using two different full-field techniques thermography (via a FLIR 7500 camera) and digital image correlation (via a high speed camera with an image resolution of 320x256 pixel^2).

Broughton et al. [56] used various measurement techniques including digital image correlation, to monitor local and global strains throughout the fatigue lifetime of open-hole composites machined from quasi-isotropic $[45/0/-45/90]_{4s}$ E-glass/913 epoxy laminates, and multiplexed fiber Bragg grating (FBG) sensors to measure the residual stiffness resulting from the increasing of number of cycles. However, the study was restricted to monitoring longitudinal strain, specifically at the mid-section of the notched samples for a single stress level. The images were recorded during statically reloading the specimen to a constant load at a frequency of 1 Hz using a single megapixel camera after stopping the fatigue testing at set intervals of 10000 cycles.

Sisodia et al. [57] used DIC for full-field strain measurement of composites under fatigue loading with the help of a high speed camera that captures images at a peak load level for every cycle. They also used microscopy to track the micro-cracks formation at certain milestone levels of load cycles.

The aforementioned studies represent the very limited number of existing studies in the literature that used DIC to describe the fatigue behavior of composites generally. Even for monotonic tests, there are only a few studies that used DIC to characterize the damage progression in notched composites during tensile loading [39, 40, 58, 59].

Frequency response methods have been used as reliable and cost-effective damage detection techniques when utilizing composite materials. Indeed, they are found to be a great tool for identifying even small amounts of damage in composite structures through the change in natural

frequencies, mode shapes, and damping ratios. Nevertheless, the potentially important information about damage type, shape, size, location and orientation were lost since various combinations of these parameters may engender similar frequency responses. However, a multitude of experimental studies were carried out on composite structures containing initially embedded defects. Each study represents only one type of damage: delamination, transverse matrix cracks, cut-outs or impact failures with possible different locations and severities [26-28, 60, 61].

Nonetheless, only a restricted number of studies have focused on establishing relationships between fatigue damage, fatigue life, and changes in the modal vibration responses of composite structures[62-65]. Bedewi and Kung[62] conducted experiments to determine the effects of changes of modal parameters, natural frequencies, and damping ratios on the fatigue life of composite samples. They correlated these changes with the prediction of fatigue failure life for selected composite specimens. They selected modes 5 and 6 to predict fatigue life due to the apparent sensitivity of these modes to the induced damage. They also suggested the use of damping ratios to predict fatigue life as a backup approach to support predictions made using natural frequencies. Abo-Elkhier et al. [63] performed plane bending fatigue tests on glass fiber polyester composites with different lamina orientation: $[0°]_3$, $[45°]_3$ and $[90°]_3$. The fatigue tests were interrupted at different fatigue life ratios and modal testing was conducted to determine the change in modal parameters. The results showed that these changes offer a means for predicting the fatigue life of composite structures. However, the latter two studies involve the effects of out of plane bending fatigue on the modal properties of composite structures. Moon et al. [64] developed a non-destructive fatigue prediction model for matrix-dominated fatigue damage of composite laminates. They related the natural frequencies of cross-ply laminates under tension-tension fatigue loading to the equivalent flexural stiffness reduction which is a function of the elastic properties of sublaminates and the number of cycles. In this method, only the 90° plies undergo stiffness reduction while the 0° plies remain intact. This relation indicates that there is an equivalence relation between a residual natural frequency and extensional stiffness reduction. They also conducted vibration tests on $[90°_2/0°_2]_s$ carbon epoxy laminates to verify the natural frequency-reduction model. Kim [65] established a vibration-based damage identification for cross-ply carbon fiber epoxy laminates under fatigue loading. This structural damage identification uses the structural dynamic system reconstruction method by using the frequency response functions of damaged structure. The two previous studies represent the only available studies in the literature

to study the effect of axial-fatigue testing damage on the modal parameters of composite structures during their fatigue life.

This study has carried out an extensive experimental program to investigate and quantify the damage development by measuring the residual properties throughout the fatigue life of open-hole quasi-isotropic $[0/-45/+45/90]_S$ T650/F584 (Hexcel) carbon-fiber/epoxy laminates loaded in tension-tension fatigue. The current work focuses on the application of (a) the Digital Image Correlation (DIC) technique to determine the strain profiles at selected locations of fatigued and non-fatigued specimens and (b) vibration tests to determine the frequency response of undamaged and fatigued specimens. X-ray scans are performed to partially fatigued samples to investigate damage details throughout the fatigue lifetime.

4.3. Materials processing and Experimental Methods

4.3.1. Tested materials

Seven composite plates measuring 305 mm x 305 mm were autoclave manufactured using carbon fiber epoxy Hexcel T650/F584 pre-impregnated tapes with a quasi-isotropic [0°/-45°/+45°/90°]S lay-up. The plates were cured according to the manufacturer's specifications [31]. The temperature was raised to 179°C at a rate of 3°C per minute and then kept constant for 120 minutes. Afterwards, the temperature decreased to the ambient temperature with the same heating rate before releasing the pressure. A pressure of 689 kPa was applied during the duration of the cycle to obtain a void free laminate. Specimens with the dimensions 140 x 25.4 x 2.3 mm (Figure 4.1) were machined from the manufactured plates avoiding their edges using diamond-wheel saw blade. The edges of all cut specimens were subsequently ground using water-cooled grinding wheel to remove any large saw nicks on the edges which might influence the damage development during the fatigue tests. A limited number of samples were tested in the unnotched configuration to determine the strength of quasi-isotropic laminates. For the remaining samples, a hole of diameter 6.35 mm was drilled using a water-cooled tungsten carbide drill bits. Sacrificial frontal and backing plexiglass plates were used to clamp the specimens during the drilling process in an effort to reduce damage from the machining process. Specimens were visually inspected to ensure no damage was present at the hole prior to testing.

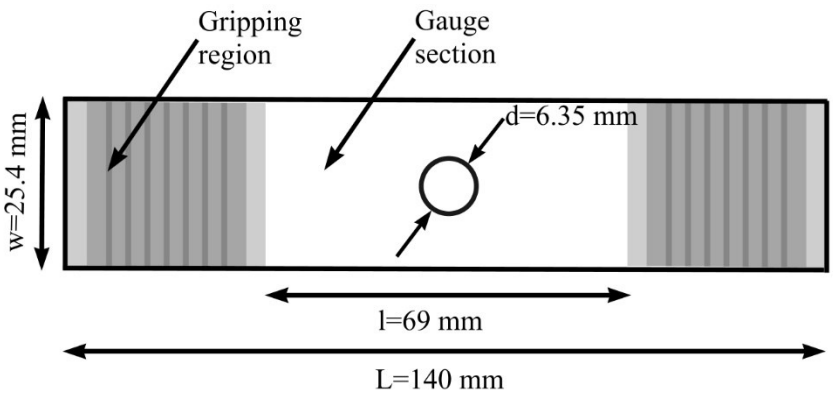

Figure 4.1. Specimen geometry

4.3.2. Experimental procedure

There were three main types of tension tests conducted in this study: quasi-static tests of virgin unnotched and notched specimens, tension-tension fatigue tests of notched specimens, and quasi-static tests of specimens from the interrupt fatigue tests.

All tension tests were conducted at a room temperature on an 89kN MTS load frame equipped with hydraulically operated wedge grips. The load frame servo-valves were controlled by MTS 407 controller operated in external input mode. The desired load voltage signals were created by a custom LabView program and National Instruments PCI-6221 M series DAQ card that also recorded the load and strain response data. Stainless steel wire cloth (100x100 mesh size) was used to prevent slipping of the unnotched specimens in the grips and fracture in the gripped region. Masking tape was used to adhere the mesh to the samples prior to gripping. The mesh cloth was not used for the notched samples as failure tends to occur around the central notch. Unnotched and notched samples were initially quasi-statically loaded to total failure to determine the average of ultimate tensile strength. All these tests were conducted in displacement control at a rate of 0.0254 mm/s with a gage length of 69 mm. The Correlated Solutions Digital Image Correlation (DIC) system was used to obtain the full in-plane strain field on the outer ply of the laminate of each quasi-static test.

Each fatigue test was conducted in load control using a constant amplitude, with an R ratio of 0.1 and frequency of 10 Hz. Each test was left to run to 106 cycles or to total failure, which ever occurred first. Fatigue tests were carried out at 65%, 70%, 75% and 80% of the nominal static failure load.

Selected fatigue tests were interrupted after various extents of stiffness loss to assess the damage effect on the strain field and the natural frequencies. For each stress level, the specimens were cyclically loaded to different percentages of the median life time, and frequency response experiments are performed using a dynamic signal analyzer followed by a quasi-static test with 3D DIC observation. After pausing the tests and performing the suitable measurements with the DIC and dynamic signal analyzer, loading resumed with the same fatigue loading conditions, and so forth. In addition, other tests were also paused at various preselected cyclic intervals to obtain the X-ray images.

In this study, average strain values were measured for all continuous and interrupted fatigue test specimens using a clip gauge extensometer recorded over a gauge length of 25.4 mm symmetric about the hole. The extensometer was mounted via aluminum "V" shapes, adhesively bounded to the surface with rubber silicone adhesive, and attached with rubber bands that enlace the specimen to attain robust measurements during cycling. Two tapes were applied at the sharp edges of the specimen in order to prevent the rupture of rubber bands. The use of silicone adhesive permits easy removal of the "V" shapes and the adhesive for the frequency response and DIC measurements.

4.3.3. Digital Image Correlation

The Correlated Solutions DIC system was used to obtain two-dimensional contours of the strain distributions (ε_{xx}, ε_{yy} and ε_{xy}) on one exterior face of the notched specimens during the quasi-static tests for virgin samples and those subjected interrupted fatigue testing. To do so, a 3D measurement setup was performed, using two Allied Vision Prosilica GX 1660 CCD (1600 x 1200) cameras, each with 2 megapixel resolutions and 66 fps capability, equipped with Nikon lenses and mounted vertically on a tripod for better spatial resolution. Prior to testing, the samples were painted first with high heat Rust-Oleum white paint and then speckled with black paint to create a high contrast stochastic pattern as required for the DIC measurement. The sample is illuminated using white LED lights that can conveniently be adjusted to provide even illumination across the entire sample. Cameras are then calibrated for their position and orientation using an appropriate calibration grid plate. A timed capture method was adopted, using Vic-Snap, to record temporal equidistant sequence of images with the rate of 10 frames per second. A shutter time of 4.5 ms was used. An analog input channel was used to record load. During post-processing with

Vic3D (Correlated Solutions) software, the deformation of the specimen in a region of interest around the hole was analyzed using subset sizes ranging between 28 x 28 pixels^2 and 35 x 35 pixels^2 and a step size of 7 pixels. All strain results were calculated relative to the first image recorded at zero load.

4.3.4. Vibration measurements

Laser Doppler Vibrometry (LDV) is an optical technique capable of accurately measuring vibration velocity and displacement of any kind of structure, in a non-intrusive way, overcoming the problem of mass loading, typical of contact sensors as accelerometers and strain gauges.

In order to examine the effect of progressive fatigue damage on the dynamic properties of notched composites, frequency response measurements were conducted on preselected samples fatigued at different ratios of fatigue lifetimes for a selected stress level. These vibrational tests were performed using a non-contact single point laser vibrometer Polytec OFV-505 coupled to the modular Polytec OFV-5000 vibrometer controller [32]. The composite specimen was clamped at one end with an overhang length of 130 mm; the other end was free. A small piece of copper reflective tape of negligible mass was applied to the tip of the specimen. The laser vibrometer reference beam was aligned with the reflective tape. An external random excitation (Gaussian white noise) is applied at the base (the clamped end) via a permanent magnet LDS V408 shaker and a LDS PA100E power amplifier. The vibrometer sensor head measured back-scattered laser light from the copper tape of the vibrating composite beam. The controller processes these obtained vibration signals through its embedded analog decoder VD-02 to obtain velocity information. A National Instruments system with a PXI-4461 (24-Bit, 204.8 kS/s, 2-Input/2-Output) and a PXI-4462 (24 Bit, 204.8 kS/s, 4-Input) data acquisition module with antialiasing filters records the velocity from the laser vibrometer and provides the output signal for the shaker. The Sound and Vibration Measurement Suite in LabView 2010 is used for calculating the results, displaying the data, and saving the data. The FRF magnitudes and their relevant critical frequencies were then highlighted over a preset frequency range of 6 kHz. Those obtained critical frequencies are the modes of the notched composite structure under out of plane excitation.

4.3.5. X-Ray Computed Tomography

In order to track the fatigue damage patterns, selected fatigue tests were also interrupted at various stages of damage accumulation, as indicated by number of fatigue cycles and the decrease in effective modulus.

To enhance X-ray contrast, an X-ray solution penetrant comprising of 60g zinc iodide (98% pure), 10 ml distilled water, 10 ml isopropyl alcohol and 10 ml Kodak Photo-Flo 200 was painted onto the specimen using cotton tipped applicator [33]. All surfaces of the samples (front and back faces, lateral edges and the interior surface of the hole) had penetrant applied to them in the hope that the dye penetrant, supported by capillary action, would penetrate all cavities. Cracks and interior delaminations which were not reached by the penetrant remain invisible in the X-ray process. Before X-ray scanning, the extra penetrant over the surfaces of the samples was removed using light spray of isopropyl alcohol.

X-ray Computed Tomography (CT) was undertaken at the X-ray imaging facility of Virginia-Maryland College of Veterinary Medicin. Helical scanning was performed using a whole-body Toshiba Aquilion 16(Model TSX-101A, Toshiba Medical Systems, Inc) Computed Tomography (CT) scanner under the following settings: 120 kV tube voltage, 300 mA tube current, 2.00 mm slice thickness, 0.50 mm slice overlapping interval, a gantry rotation time of 0.5 s and a reconstruction matrix of 512 × 512. After acquisition of the raw spiral CT data, Multiplanar Reconstruction (MPR) images were developed by the computer that was a part of the CT system using a sharp reconstruction filter. Images were then displayed and edited using eFilm lite which is an application used for viewing and manipulating digital images from various radiographic devices.

4.4. Results and discussion

4.4.1. Quasi-static tests

Five notched quasi-static tests were conducted to determine ultimate tensile strength (UTS), stiffness and strain t2o failure. The DIC technique was used in conjunction with all quasi-static tests to obtain the full in-plane strain field on the outer face of the laminate. The correlations among various grey values of digital images are analyzed by comparing the deformed and un-deformed images to obtain the displacement and strain fields surrounding the notch [66]. After post processing of captured images and acquisition of strain contours at different load stages, a virtual

extensometer, a measurement tool within Vic3D with a 25.4 mm gauge length, was placed on both sides of the hole in order to measure the local maximum strain to failure. The average notched UTS σ^N, stiffness E_0 and maximum strain to failure $\varepsilon_{\max f}$ values were equal to 393 MPa, 37.74 GPa and 1.07% respectively with coefficients of variation 2.9%, 2.33% and 5%. The unnotched tensile strength of the laminate σ^U, was also measured using five test specimens and the average value obtained was 581.35 MPa with a coefficient of variation of 4.7%. The average ultimate tensile strength of notched specimen was used subsequently to calculate load levels for fatigue.

In addition, the longitudinal, transverse, and shear strain profiles in different sections, on the outer layer of the notched specimens were determined for multiple stress levels using the DIC technique. Figure 3.3 shows the strain profiles in different sections for various load stages of a quasi-static test of one specimen. These curves represent the baseline results that will be used for further comparison with strain profiles of fatigued specimen at different life times and different load levels. Sections 1 and 2 labeled sec1 and sec2 respectively on all figures were drawn with two lines in the locations schematically shown in Figure 3.3. The length of these two sections are 8 mm and 22.35 mm approximatively. Section 2 is positioned 5 mm away from the top of the hole. The transverse strain is negative because of the Poisson effect. The results obtained for the other specimens are similar to the results shown for this chosen specimen. Figure 4.2 shows the strain profiles of all samples at the two extreme load cases 20% UTS and 95% UTS where the profiles are expected to be noticeably different because correlations at low level load and high level load are sensitive to many DIC parameters (discussed later) and surface damage respectively.

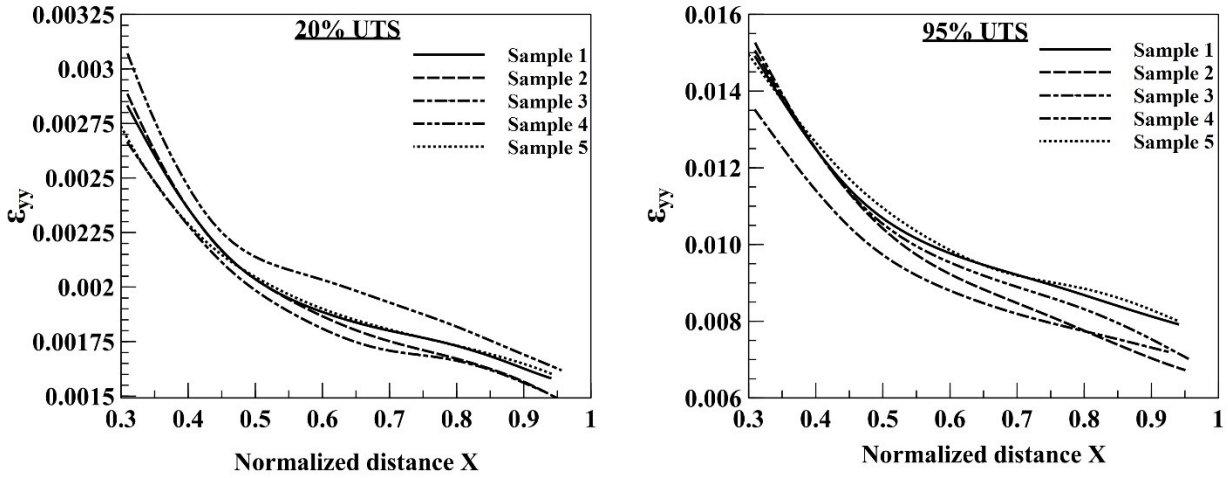

Figure 4.2. Strain profiles at 20% UTS and 95% UTS of all quasi-static tested specimens

4.4.2. Fatigue tests

Constant-amplitude tension-tension fatigue tests were performed at 65%, 70%, 75% and 80% UTS using a stress ratio R=0.1 and a loading frequency 10Hz. Specimens were generally tested to failure for this section. Tests with 65% maximum stress amplitudes were stopped because they did not fail after 10^6 cycles. A minimum of four replicates were tested under each test condition.

A summary fatigue lifetime curve in which the fatigue data were plotted in terms of normalized maximum applied stress $(\sigma_{\max} / \sigma_{UTS})$ with respect to the ultimate tensile strength (UTS) versus the number of cycles to failure N_f is given in Figure 4.3. The line of best fit is given in the form of

$$\frac{\sigma_{\max}}{\sigma_{UTS}} = 1 - k \log_{10} N_f .$$

where $k = -0.0623$. Significant scatter is observed in the tests conducted at 70% of the ultimate tensile strength. While the results in Figure 4.3 are based upon total failure of the samples, others [67] have suggested using 15% stiffness loss to define failure. If such a definition is adopted, less scatter is observed in the lifetimes. However, the definition of failure becomes somewhat arbitrary. The resulting lifetimes are also very conservative, as samples may exhibit 70% stiffness loss with significant load carrying capability.

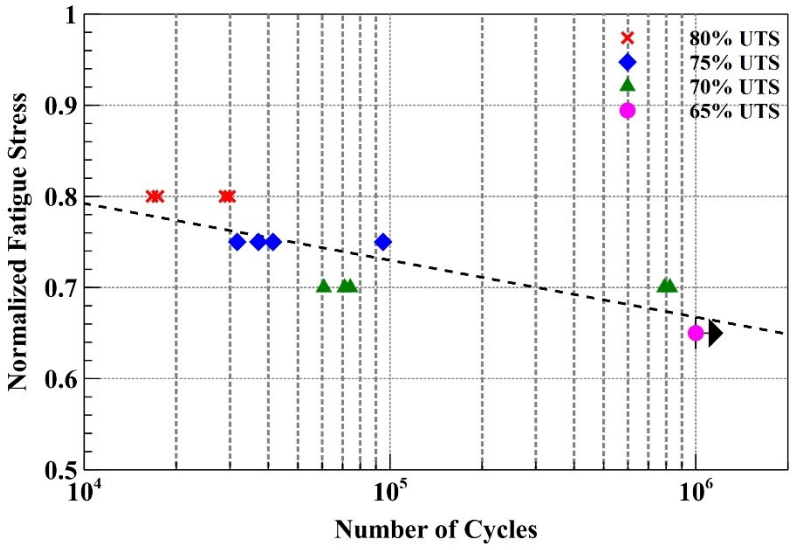

Figure 4.3. Summary of fatigue lifetime results

The damage induced during fatigue loading was assessed as a first step by real-time monitoring of stiffness degradation. During load cycling, the effective modulus E is calculated by using

$E(N) = \dfrac{\dfrac{F_{\max} - F_{\min}}{A}}{\varepsilon_{\max} - \varepsilon_{\min}}$ where $\varepsilon_{\max}$ and $\varepsilon_{\min}$ represent the extrema strains at peak and valley loads $F_{\max}$ and $F_{\min}$ respectively. The longitudinal deformations were measured with 25 mm gage length extensometer surface mounted with the hole centered in the gage length.

The loss of stiffness is obtained to characterize the effect of propagating damage and to relate it with strain contours and frequency responses changes. Figure 4.4 shows a typical plot of effective modulus for each normalized applied stress. The reduction in stiffness occurs continuously over the fatigue lifetime of composite coupons for 70%, 75% and 80% severities except for 65% severity and lower ones in which stiffness reduction is limited to a portion of their total life. This latter stiffness remains constant for the remaining truncated curve. The stiffness reduction represents an excellent indicator of the damage development in composite materials [68-70]. However, the rate of effective modulus degradation may be misinterpreted because of the logarithmic axis for fatigue cycles. If we consider a plot of effective modulus versus fatigue cycles (on a linear scale), the trend is described by a continuous decreasing curve until impending failure, indicated by a sharp loss of effective modulus. This response holds for all cases examined except for the lowest cyclic stress level where there is a plateau of constant effective modulus with fatigue cycles. This observed behavior is unlike the behavior seen in [56] for the fatigue of notched glass fiber composites. The glass fiber composites exhibit a significant decrease in stiffness within the initial cycles (described as phase I) followed by a period of nearly constant effective modulus (phase II) before the total failure.

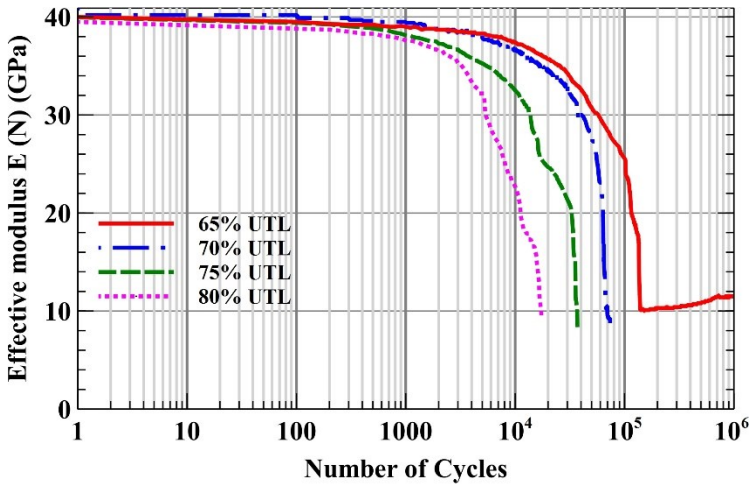

Figure 4.4. Degradation of effective modulus as a function of number of cycles for different load levels

Some damage modes such as axial splits emanating from the hole on the outer surface of the sample and delamination near the free edges and around the hole are visible during fatigue loading. The amount of stiffness degradation is quantified by the damage parameter D defined by $D = 1 - E(N)/E_0$ where E_0 is the initial stiffness measured at the beginning of the test and $E(N)$ is the stiffness at the given cycle N.

4.4.3. Interrupted fatigue tests

4.4.3.1. DIC results

A number of quasi-static tests were performed for interrupted fatigued specimens, with peak amplitude at 80% of UTS, at various life times. In each case, the quasi-static loads were limited to the maximum loads applied during fatigue cycling. Among the possible non-destructive techniques (thermography, scanning electron microscopy, acoustic emission, moiré interferometry and ultrasound) available to localize or identify the damage induced by mechanical loading in high gradient zones such as in notched composites, the DIC technique gives both good qualitative and quantitative information about the strain fields around the hole. Accordingly, three dimensional DIC analysis was used for each test to determine the full field strain on the outer ply and especially the strain profiles at selected sections.

Figure 4.5 shows the axial strain ε_{yy} curves of one sample being fatigued at a peak stress corresponding to 80% of the UTS which was loaded quasi-statically to 20%, 40%, 60% and 80 % of ultimate stress after experiencing 0.1, 0.3, 0.5, 0.7, 1 and 1.3 of the median lifetime for notched composites at that stress level. For different quasi-static load levels, the longitudinal strain profiles obtained from interrupted tests were compared to the baseline results of non-fatigued specimen. As expected, ε_{yy} is maximum at the hole due to the strain concentration introduced by the presence of the hole. Clear offsets between the strain profiles around the hole and near the free edge are observed. These offsets characterize the degradation experienced by the sample during its fatigue lifetime. In general, the magnitude of the strain increases with fatigue cycles (as expected, because of the presence of damage within layers). In addition, the magnitude of the difference between the strains at the edge of the hole and near the free edge also increases.

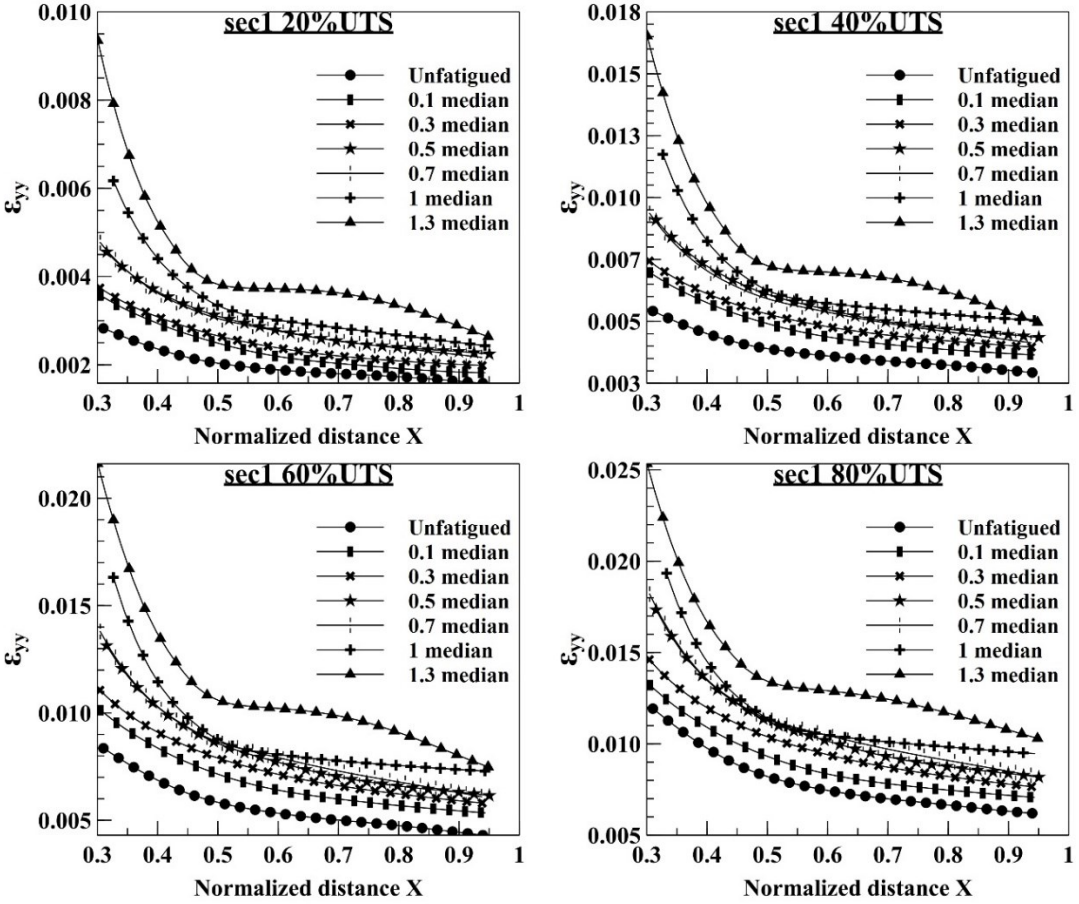

Figure 4.5. Strain profiles at different quasi-static load levels for specimen fatigued to various life fractions

During mechanical loading, including the fatigue cycling, interlaminar stresses develop and may lead to local delamination of adjacent layers. Subsequently, the layers act independently of the multidirectional laminate. The presence of these local delaminations may explain the overlap of the longitudinal strains at section 1 at fatigue lifetime ratios 0.5 and 0.7. However, shear strain profiles at section 2 for these same time frames are clearly distinct. The importance of tracking different strain components at different section locations will be discussed later.

Figure 4.6 shows DIC results of full-field engineering strain contours ε_{yy} (loading direction) of the same sample fatigued with peak amplitude 80% UTS at numerous fractions of median fatigue lifetime 0.1, 0.3, 0.5, 0.7, 1 and 1.3 and at the quasi-static load level 80% of UTS. The corresponding effective modulus degraded as a function of number of cycles is also presented in the same figure. The gradients of strains across the region of interest (ROI) are well discerned, the nuance of colors reflecting different strain values even closer to each other are clearly distinguishable. Because the hole is a discontinuity on the measured surface of the sample, the pixels localized around the notch cannot be used for calculating the strain field. The local accuracies of strain values around the edge of the notch or proximity to specimen edges or even across the sample's width depend on many parameters: fineness and density of the sputtered black painting on the white painted surface, speckle pattern, subset size, step size, the lighting conditions, the alignment of the specimen, the alignment and position of the cameras relative to the specimen and the resolution of the cameras [71]. Maximum axial strains are observed around the transverse edges of the hole perpendicular to loading direction. Low axial strain zones are across the longitudinal edges of the hole parallel to loading direction. These observations are valid for unfatigued specimen as well as fatigued specimen at various fatigue lifetime ratios. The regions of highly concentrated strains near the hole identify the emanation of axial splits from the hole towards the longitudinal extremities of the samples. Uncorrelated regions were observed due to the discontinuous displacement fields at the axial splits. The figure depicts the onset of cracking in the surface ply at 0.5 median fatigue lifetime and the development of the severe cracks in the surface ply at 0.7 median fatigue lifetime. The figures clearly indicate the cracks developing along the fiber direction reaching the longitudinal edges of the ROI of the sample prior to failure. This behavior is consistent with the results obtained for monotonic tests done by the researchers in [40].

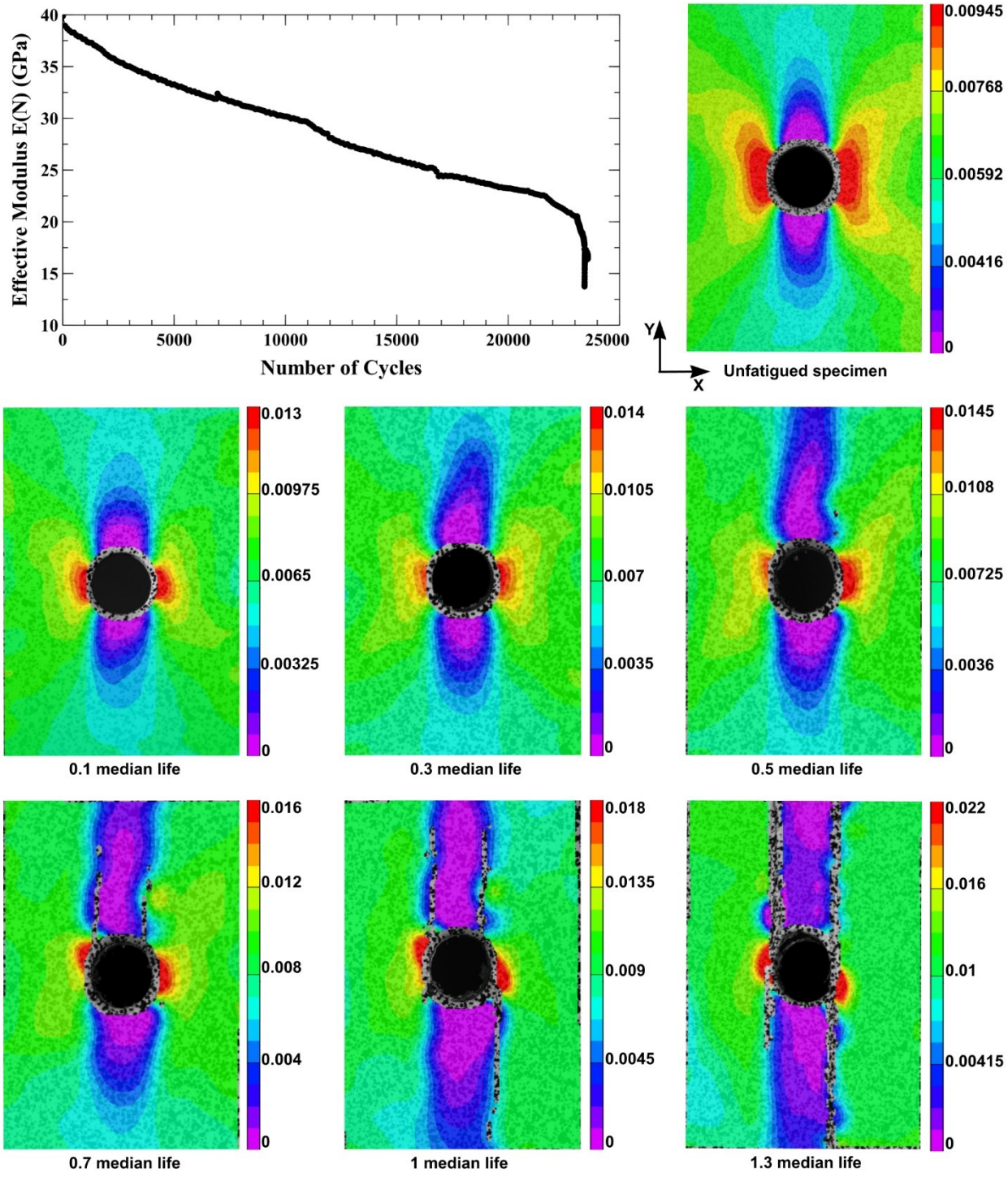

Figure 4.6. Full-field longitudinal strain (ε_{yy}) contours of fatigued specimen at different lifetimes loaded statically at 80% of UTS. It should be noted that each contour plot used a different scale at each median fatigue lifetime ratio.

Figure 4.7 shows DIC results of full-field engineering strain contours ε_{xy} of the previous sample at various fractions of median fatigue lifetime 0.1, 0.3, 0.5, 0.7, 1 and 1.3. The DIC images for all cyclic intervals show high values of the shear strains along narrow bands oriented in the loading direction and tangential to the hole, corresponding to the fiber/matrix splitting observed on the X-ray radiographs. The non-perfect symmetry of strain distribution as well as damage development is likely due to asymmetrical damage evolution around the hole, specimen thickness variation along and across the specimen width and slight misalignment of the specimen. In addition, given the current layup sequence of [0,-45,45,90]s, the surface damage evolution would not be symmetric. In fact, the surface stresses are heavily influenced by the -45° ply directly below the top 0° ply. The figure shows the initiation of fissure at 0.5 median fatigue lifetime surrounded by high shear strain zone and the accumulation of axial cracks at 0.7 median fatigue lifetime. The DIC method can be used for anticipating the crack paths by measuring the uneven shear strain distributions and localizing high strain concentrations and observing the process of cracks development in notched carbon fiber composites throughout the cyclic fatigue life. The fiber splitting is the failure mode that can be determined based on the strain diagrams.

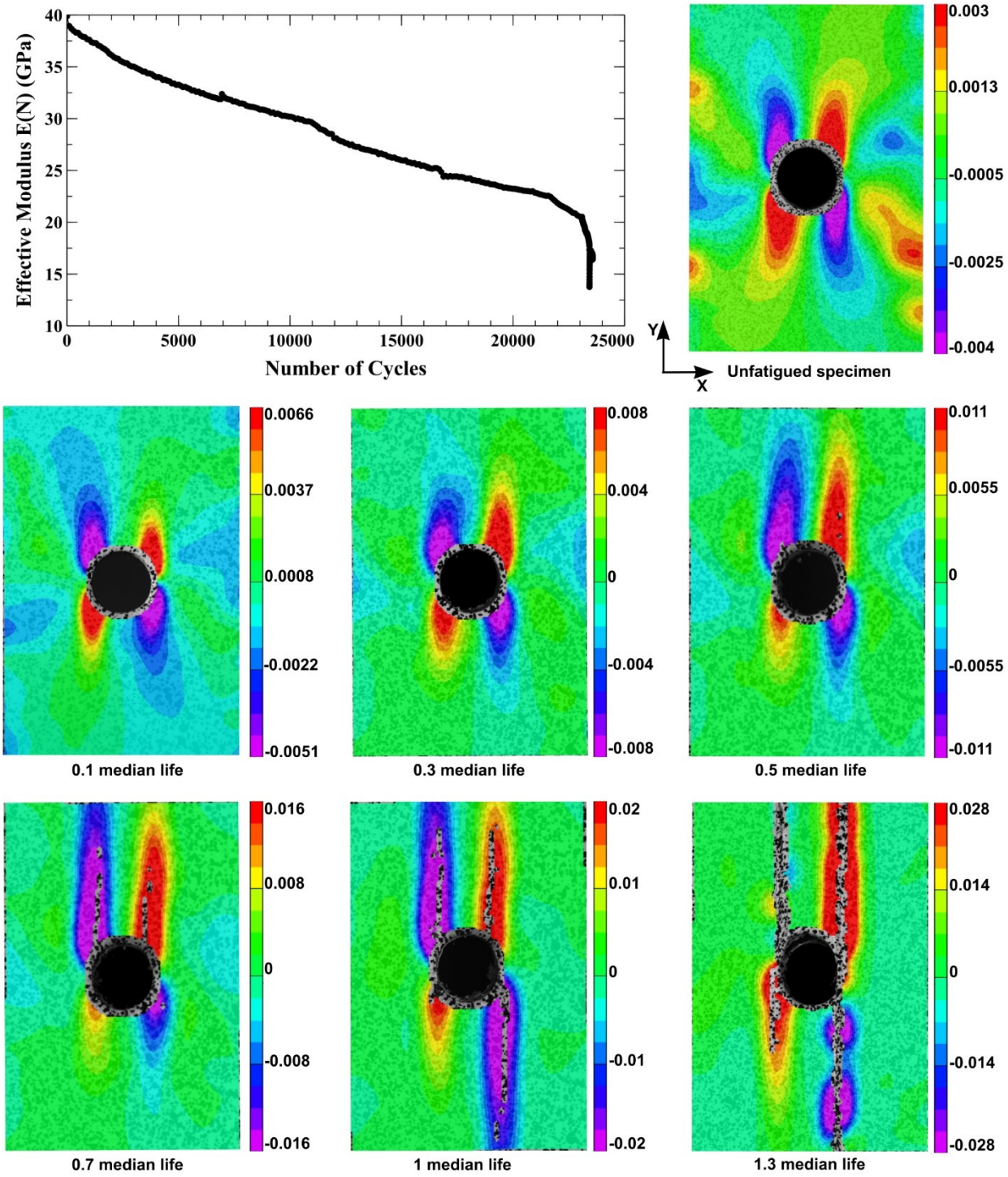

Figure 4.7. Full-field shear strain (ε_{xy}) contours of fatigued specimen at different lifetimes loaded statically at 80% of UTS. It should be noted that each contour plot used a different scale at each median fatigue lifetime ratio.

Due to the damage caused by the axial splits, stress redistribution occurred within the surface layer. This distribution is confirmed by the tendency of the longitudinal strains at section 2 to increase with increasing fatigue lifetime (Figure 4.8). The fatigue damage induced a decrease in shear modulus and that caused the longitudinal strains to be virtually plotted at sections parallel to section 2 closer and closer to the notch vicinity with increasing fatigue damage. This represents the increase of effective axis length of the hole, resulting in a hole that performs like an ellipse with the major axis aligned with the direction of loading. This effective major axis length increases with increasing fatigue cycles, blunting the effect of the notch. Shear strain profiles at section 2 were extracted also for the different fatigue lifetime ratios. The trends of the curves seem to be consistent with increasing fatigue lifetime. In fact, local valleys decrease and local peaks increase with increasing fatigue lifetime. This combined with DIC shear strain maps gives an idea about the critical shear strain value that exhibit axial splits. Figure 4.8 also shows the transverse strain profiles at section 1 and 2. The transverse strains at section 1 shows a reversal nature with increasing fatigue cycles' number compared to the curve of the unfatigued sample. ε_{xx} decreases in magnitude near the hole edge and then tends to increase until reaching a local zero slope before decreasing back and becoming minimal near the specimen edge. Nonetheless, the variation of local extrema is not consistent with increasing fatigue lifetime ratio, which makes evaluating the fatigue damage severity from the obtained transversal curves difficult. The transverse strain profiles at section 2 seem to have the same pattern with the exception of the profile related to 1.3 median fatigue lifetime ratio. The profiles corresponding to fatigue samples are distinct from the curve of the unfatigued one. However, there are only small changes in these profiles throughout the fatigue lifetime making the transverse strain a poor indicator of fatigue damage.

It is shown in this section that the DIC technique provides qualitative and quantitative information that can be used to predict and identify potential damage zones especially in high gradient areas. Moreover, the high localized strains identified by the DIC technique were in good agreement with damage captured by penetrant enhanced X-ray radiographs discussed in the following section.

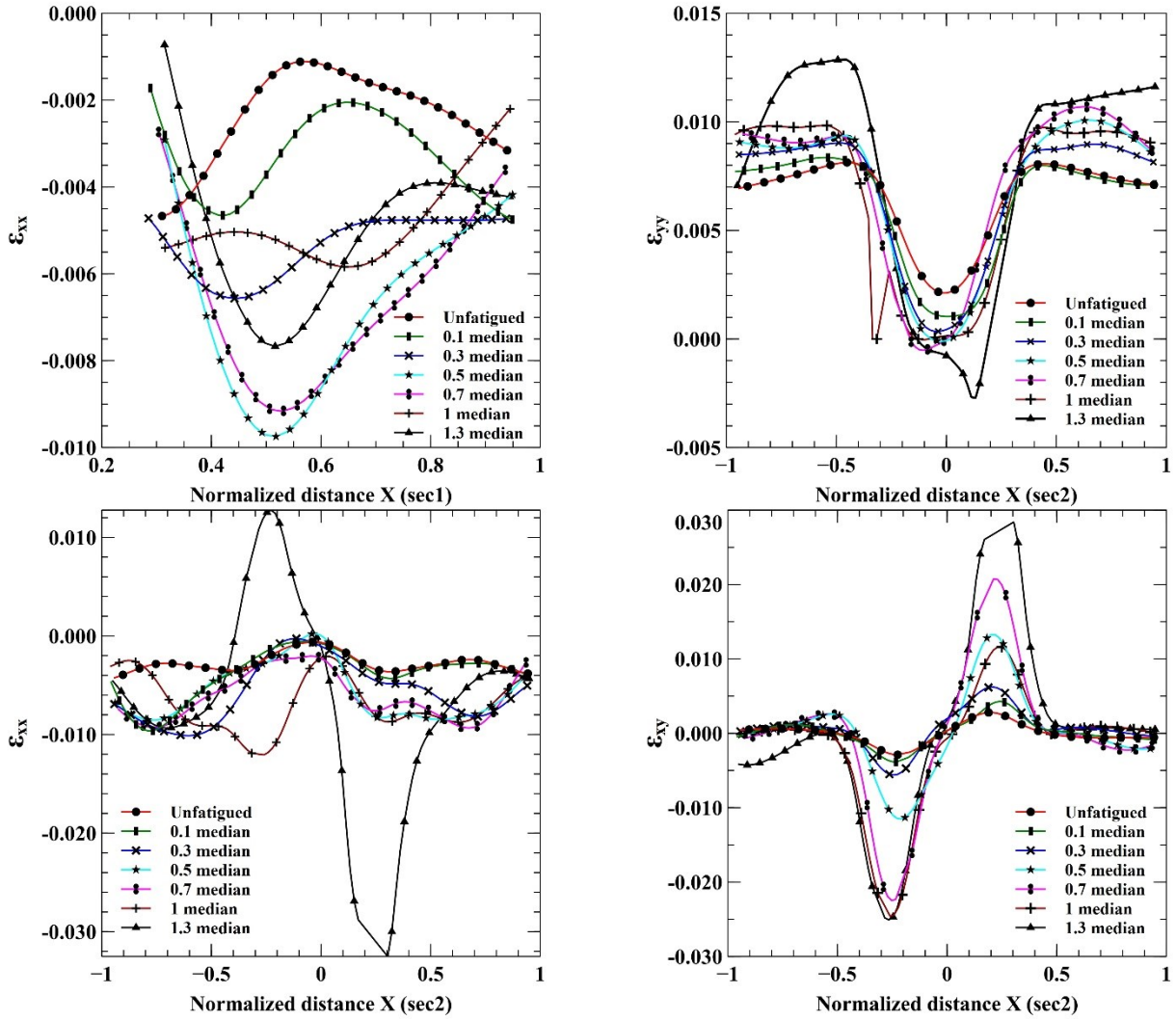

Figure 4.8. Longitudinal, transverse, and shear strain profiles of fatigued specimen at different sections locations

4.4.3.1. X-ray radiography results

Six notched specimens were cycled to preselected fractions of median fatigue lifetime with a stress level of 80% UTS. Degradation of effective modulus was tracked for all specimens during fatigue cycling. After the cyclic fatigue loading was stopped at the selected number of cycles, the specimens were subjected to vibration tests to measure frequency response and DIC measurements, and then examined via X-ray computed tomography (CT). Variation in the damage parameter, maximum strain at the transverse edge of the hole, and change in the 8th natural frequency for all samples were summarized in Table 4.1.

Table 4.1. Physical properties of 6 notched coupons at different median fatigue lifetime ratios

Sample ID	Median fatigue life ratio	$\varepsilon_{yy\max}$	$D = 1 - E(\mathrm{N}) / E_0$	$\Delta f_8 (Hz)$
106	0.025	0.0155	0.05	26
204	0.1	0.0128	0.08	42
305	0.3	0.0139	0.17	226
405	0.5	0.0171	0.35	3300
606	0.7	0.0165	0.38	3384
604	1.3	0.0250	0.73	1499

Figure 4.9 illustrates the 3D visualization of the extent and mechanisms of fatigue damage at 0.025, 0.3, 0.5, 0.7 and 1.3 of median fatigue lifetime ratios. This figure indicates that at the earliest stages of fatigue, the predominant damage mode is transverse cracking in the 90° plies, as expected. However, there were a few instances of cracks developing in the ± 45° plies. Thereafter, the beginning of edge delaminations and the onset and growth of axial splitting in the vicinity of the hole are observed at 0.1, 0.3 and 0.5 median fatigue lifetime ratios. The preponderance of transverse matrix cracks appears to develop during the two latter fatigue lifetime ratios with the exception of the sample cycled until 0.025 of median fatigue lifetime which experienced a relatively larger matrix cracking density. This damage state explains the progressive increase in high localized longitudinal strains observed by DIC near the hole and the driven axial splits, parallel to loading axis, by the higher shear strain strips. In addition, local delaminations commence to develop between the two major axial splits tangent to the hole perimeter. At later stages delamination continues to grow and becomes the predominant damage mode. The notched specimen at 0.7 median fatigue lifetime begins to exhibit noticeable off-axis cracks tangent to the hole edge. Prior to failure, local and edge delaminations accelerate to expand all over the sample. Significant delamination development is observed in the sample fatigued to 1.3 times the median fatigue lifetime.

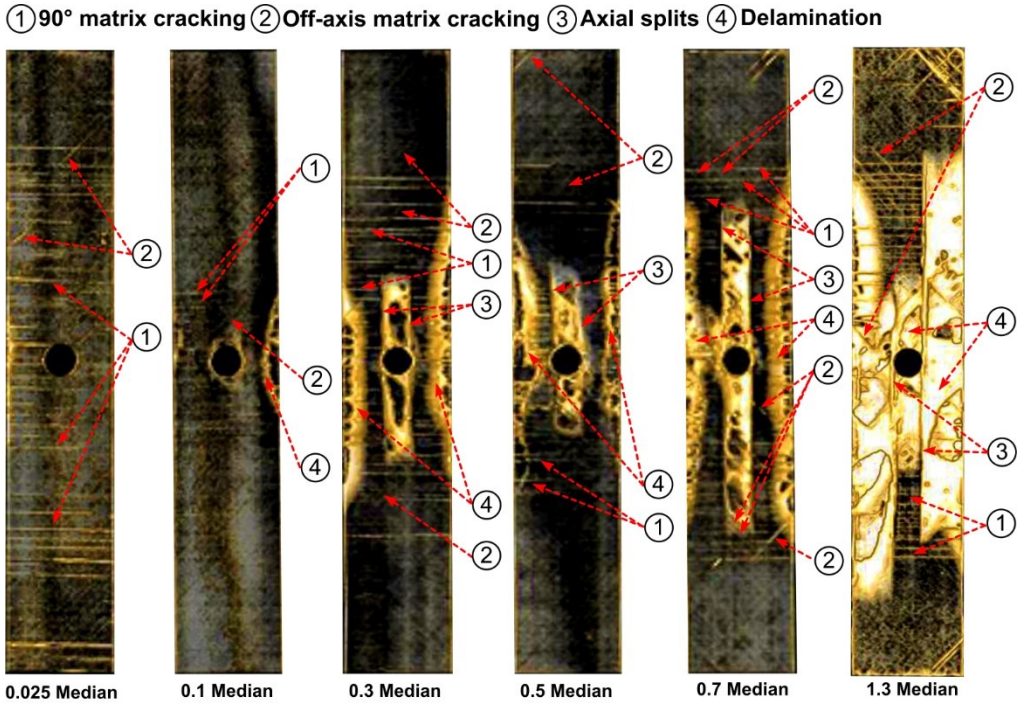

Figure 4.9. Integrated 3D images of damage of notched specimen at different fatigue life ratios

Using normal through-thickness X-ray radiography makes the precise determination of the shape of a delamination at each interface difficult because it integrates the effects of delamination at all delaminated interfaces. This shows the capability of X-ray CT in determining the extent and shape of delamination at interfaces. The damage at these interfaces can be seen in the X-ray CT slices in Figure 4.10 for two samples fatigued at 0.3 and 0.7 median fatigue lifetime ratios. For both samples, the first interface 0°/-45° shows local delamination between the two major longitudinal splits. The delamination located around the hole seems to arise from off-axis matrix cracks within the -45° layer tangent to the hole. However, this local delamination appears to expand in samples having higher numbers of cycles. It is evident from the X-ray image that this distinctive shape of local delamination delimited by the two axial splits is related in size to the splits. The second interface -45°/0° for both samples shows nearly similar damage patterns to the first interface but they are different in growth. The interfaces 45°/90° and 90°/45° show extensive edge delaminations. Tensile interlaminar normal stress and interlaminar shear stress produced at the intersection of matrix cracks with the stress free edges under axial fatigue loading between the 45° and 90° plies lead to the onset and growth of edge delamination with increasing fatigue cycles.

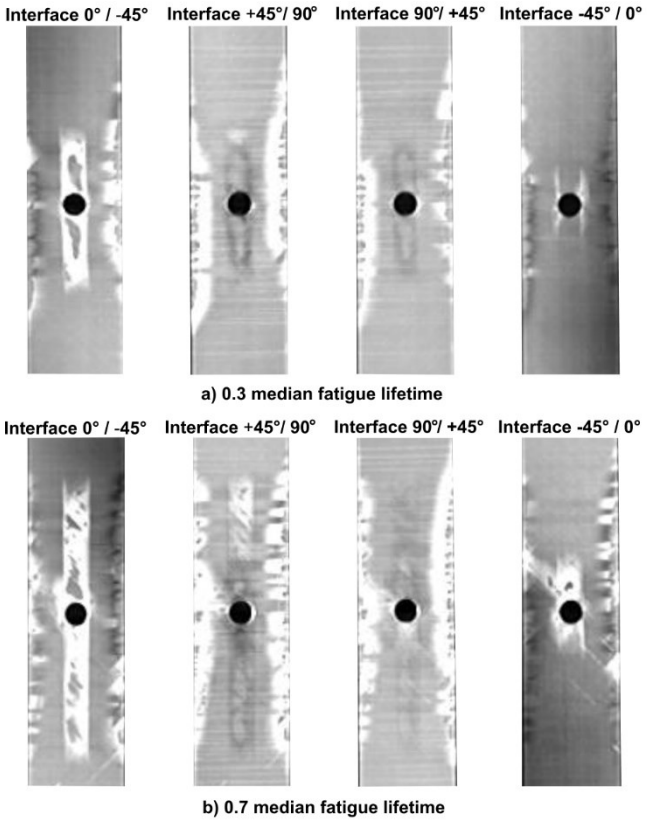

Figure 4.10. X-ray CT slices for interrupted tests at a) 0.3 median fatigue lifetime ratio and b) 0.7 median fatigue lifetime ratio

Afterwards, quasi-static tests were performed on the previous samples to determine their post-fatigue residual strengths. The results are shown in Figure 4.11. The residual strength initially increased to a value 13.6% greater than the unfatigued specimen strength at 0.1 median fatigue life ratio. It then decreased gradually for a portion of fatigue lifetime and eventually decreased sharply at the final stage of fatigue. The increase in residual strength is related to splitting at the hole edges resulting in blunting of the notch. This effect is noticeable from both the X-ray radiographs and DIC observations through the shear strain maps. These splits lead to a reduction in the stress concentration at the hole. Thus, localized fiber fracture is avoided through redistributing the load in the ligaments of the material on each lateral side of the hole. This trend echoes previous work [72]. Nonetheless, there are two competing damage modes that affect fatigue behavior. First, the matrix cracking around the notch increases tensile strength by notch blunting though it also reduces stiffness and decreases support of load-bearing fibers. Second, localized fiber fracture is promoted at the surroundings of the hole accompanied by high local stresses. These competing failure

mechanisms result in a constant or slow degradation of residual tensile strength for a portion of fatigue lifetime.

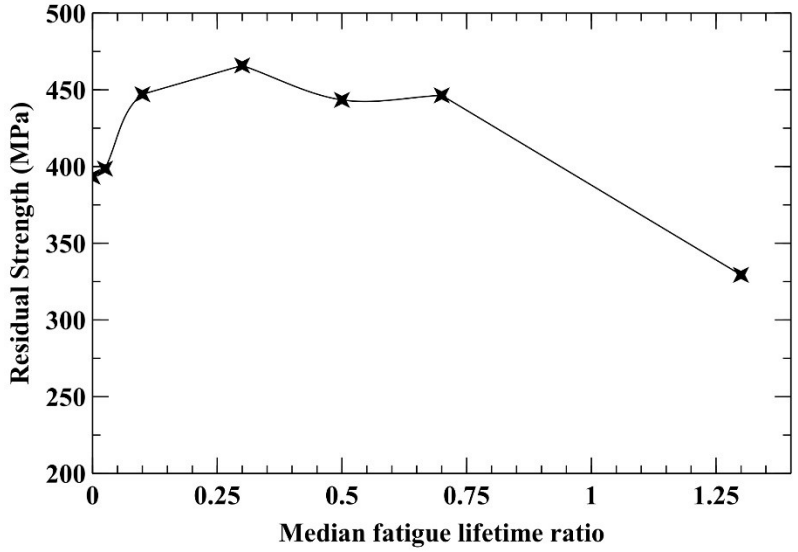

Figure 4.11. Residual strength of fatigued notched specimen at different lifetimes

4.4.3.1. Experimental frequency response results

The aim of this section is to establish a vibration-based identification method for notched carbon fiber reinforced composites under cyclic fatigue loading. This structural damage identification technique uses the structural dynamic response of fatigued damaged notched composites under excitation to examine the effect of progressive fatigue damage on the frequency response functions (FRFs). As mentioned above, the previous tests were paused at various predetermined cyclic intervals to perform vibrational tests before using DIC to obtain the full-field strain maps. The frequency responses of one sample throughout its fatigue lifetime are shown in Figure 4.12. These measured response functions of the structure have to take into account the changes of physical parameters in the structure due to progressive fatigue damage. Reduction in dynamic modulus and the damage mechanisms occurring within the structure affect the FRFs by shifting the peaks of the undamaged FRF to lower frequencies as the fatigue damage increase.

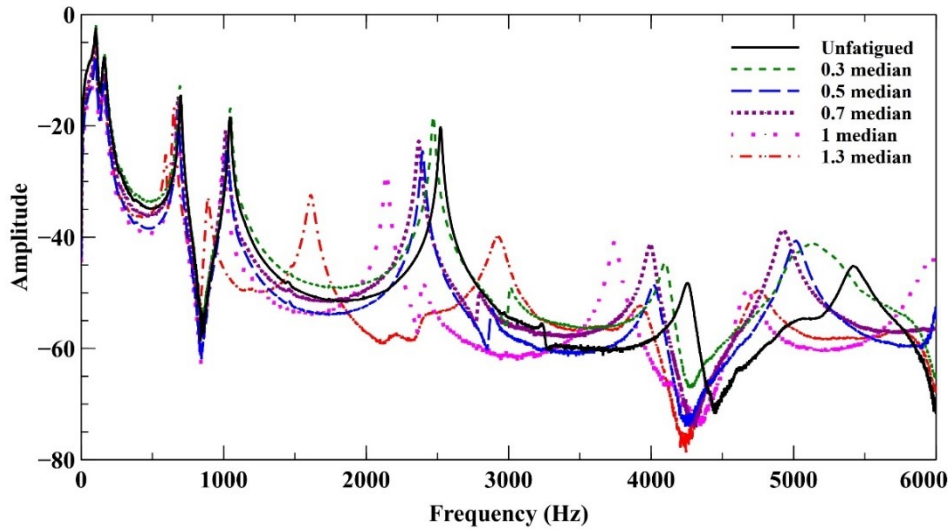

Figure 4.12. Typical frequency responses at different number of cycles relative to the load level 80% of UTS

Figure 4.13 displays the average changes (for three samples) of the first eight frequencies as the median fatigue lifetime ratio increases. These results are presented in the form of deviations of these frequencies relative to those corresponding to the healthy composite structure. This figure depicts that higher frequencies experience relatively important changes compared to lower frequencies. These noticeable changes in the natural frequencies of induced-fatigue damaged composites may represent potential candidates for assessing fatigue damage level. A similar result was found in [73].

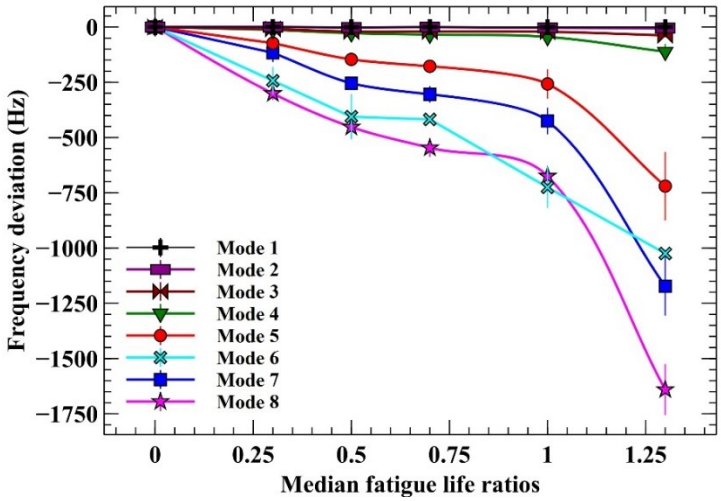

Figure 4.13. Effect of axial-fatigue loading on natural frequencies. Symbols represent mean of 3 samples; error bars are standard errors.

Furthermore, the current study has shown the potential of DIC to track the progressive fatigue damage, most of the time, by the change of strain maps and strain profiles at different sections. However, for some specific cases discussed earlier namely longitudinal strain profiles at section1 at the median fatigue lifetime ratios 0.5 and 0.7, there is no noticeable change despite the continuous degradation of dynamic modulus and the expanding of internal damage (e.g. delamination and matrix cracks). Nevertheless, vibration measurement has clearly shown the change of the performance of the notched composite by the means of the clearly decrease of higher natural frequencies. We also note that natural frequencies are reliable parameters for detecting damage even in early stages of fatigue loading but they do not directly provide information regarding its type, location and size. The shifting and the reduction of frequencies relative to higher modes are obvious for all tested specimen fatigued with different peak amplitudes including the level load of 80% of UTS.

4.5. Conclusions

The aim of this study was to assess and monitor the evolution of fatigue damage in carbon fiber notched composites using two combined non-contact methods Digital Image Correlation (DIC) and optic based vibrations. To the best knowledge of the authors, this study is the only one that tracks different strain components and residual frequency responses through axial fatigue lifetime of notched composites qualitatively and quantitatively.

The DIC technique was used to measure the surface displacements and deformations at different fatigue lifetime ratios and revealed the progressive damage during cyclic fatigue loading as a change of strain fields' maps and particularly strain profiles at selected sections without producing any corresponding environmental effects on the specimen during testing. Furthermore, the damage initiation site was generally predicted based on highly strained zone whereas the damage propagation is monitored based on appearance of uncorrelated and discontinuity area within the outer layer of the notched specimen. The choice of this method is based on the required high accuracy and spatial resolution as well as the ease of its applicability with the provided apparatus. Indeed, with the use of 2 Megapixel cameras, gradients of strains are well discerned along the length and across the width of notched specimens even if subjected to low load ratios of UTS or low fatigue lifetime ratios. X-ray computed tomography (CT) was used to obtain an in depth picture of the sequence of failure mechanisms caused by the fatigue cyclic loading on notched composites. It has been shown that emanations and growths of axial splits were successfully captured by the DIC technique through the localized high shear strain concentrations presented in the sequence of DIC strain maps at different fatigue lifetime ratios. Three-dimensional (3D) X-ray tomographic images revealed the onset and development of splitting around the hole throughout progressive fatigue cycles confirming the observations obtained by DIC. X-ray images have also explained that the evolution of strain profiles at different sections is linked to the evolution of different types of failure modes (matrix cracking, splitting and delamination) and their extent. Post-fatigue residual strengths of fatigued notched specimen at different fatigue lifetime ratios were measured in order to verify how they are influenced under the progressive fatigue damage. The notch blunting effect caused by the axial splits leads to the increase of residual strength throughout a significant portion of fatigue lifetime compared to the unfatigued notched composite strength. At this point, no direct connection has been established between the measured longitudinal strain profiles and the increase in residual strength.

The frequency response measurements were used as a complementary method to track the fatigue damage progression through the residual FRFs of fatigued notched composites. The results show that high natural frequencies of the system are useful for the detection of early damage and to assess the damage level.

To summarize, the DIC technique and non-contact vibration tests were used on fatigued notched quasi-isotropic composites to ascertain the initiation and the progression of damage accumulation

under cyclic fatigue loading through the measurement of residual properties of the composite. In addition, X-ray CT was used, as well, to observe the through-thickness failure modes of fatigued specimen and to attribute the failure mechanisms to the change of external deformation and modal parameters. Some of the X-rays revealed damage corresponding well to regions with high strain concentrations were successfully captured by the DIC. This represents an imperative step for developing corresponding tools to predict critical damage states and fatigue lifetime.

Chapter 5. Evaluation of residual properties of open hole composites fatigued with different stress levels

5.1. Abstract

Open-hole carbon fiber reinforced polymer composites loaded in tension-tension fatigue are investigated by experimental testing. 3D Digital Image Correlation (DIC) technique with its full-field intrinsic potentiality has been used to give a description of the spatial distribution of different strain components throughout quasi-static and fatigue loading. Samples were first quasi-statically loaded using DIC to determine the average ultimate tensile strength σ_{UTS} as well as the strain distribution of different strain components. These results are used as baseline for subsequent comparison with strain profiles obtained and tracked using DIC for specimens fatigued at different fatigue lifetime ratios. Interrupted fatigue tests were carried out with various stress levels 80%, 75% and 70% of the ultimate tensile strength to monitor the impact of the fatigue damage on the strain redistribution throughout the fatigue lifetime.

5.2. Material processing and experimental procedure

The material processing and the experimental procedure is the same as described in section 4.3 of chapter 4. The only difference is the use of a high resolution DIC system. In fact, . The current 3D-DIC setup used two Allied GE400 high resolution CCD cameras. Each camera has a resolution of 10.7 MP (4008 x 2672). A careful control of boundary condition was required, the test specimens were designed to be mounted with bolts to a rigid aluminum supporting frame. A low range torque with a sensitivity of 0.5Nm was used to guarantee 30Nm for each fixture in an effort to reproduce the same tightness. Achieving a constant torque before each test is very important to reduce maximally the influence of boundary condition variance.

5.3. DIC results

After finishing the continuous fatigue testing and determining the median fatigue lifetime for each stress severity, several fatigue tests were interrupted at various median fatigue lifetime ratios (0.1M, 0.3M, 0.5M and 0.7M) corresponding to diverse stiffness loss and damage accumulation states. For each stress level, the DIC measurement was first applied to the sample at 0.1M and was

repeated on the same fatigued sample at the remaining fatigue lifetime ratios (0.3M, 0.5M and 0.7M) in order to study in detail the effect of fatigue-induced damage on the stress redistribution around the hole. It should be noted that all the specimens fatigued with the different stress levels were quasi-statically loaded at 60% UTS at interrupted tests. For each stress level of 70% UTS, 75%UTS and 80%UTS, at least four specimen were tested and followed the same procedure. It should be noted that quasi-static testing with DIC observation was first made for a number of different samples and then this observation is compared and contrasted with those obtained during fatigue cycling. The results of this method are illustrated qualitatively as well as quantitatively.

Figure 5.1 shows the full-field longitudinal strain maps of the same sample fatigued with the stress level 80% UTS and quasi-statically loaded to 60% at numerous fractions of median fatigue lifetime 0.1, 0.3, 0.5 and 0.7. The gradients of strains across the field of measurement are well discerned, the nuance of colors reflecting different strain values even closer to each other are clearly distinguishable. Maximum axial strains are observed around the transverse edges of the hole perpendicular to loading direction. Low axial strain zones are across the longitudinal edges of the hole parallel to loading direction. These observations are valid for unfatigued specimen as well as fatigued specimen at various fatigue lifetime ratios. The regions of highly concentrated strains near the hole identify the emanation of axial splits from the hole toward the longitudinal extremities of the samples. Uncorrelated regions were observed due to the discontinuous displacement fields at the axial splits. The figure depicts the onset of cracking in the surface ply at 0.5 median fatigue lifetime and the development of the severe cracks in the surface ply at 0.7 median fatigue lifetime. The figures clearly indicate the cracks developing along the fiber direction reaching the longitudinal edges of the ROI of the sample prior to failure.
Figure 5.2 shows the full-field shear strain maps of the previous sample fatigued with the stress level 80% UTS and quasi-statically loaded to 60% at numerous fractions of median fatigue lifetime 0.1, 0.3, 0.5 and 0.7. The DIC images for all cyclic intervals show high values of the shear strains along narrow bands oriented in the loading direction and tangential to the hole,

To further examine the influence of fatigue damage on the strain distribution the values of the longitudinal strain component obtained by DIC along the net section (Section1 as shown in Figure 5.3) are plotted as a function of the distance from the hole edge. The temporal evolutions

of longitudinal strain profiles calculated by 3D-DIC along Section1 are superposed onto their counterpart of pristine samples in Figure 5.4.

As expected, the longitudinal strain (Exx) is maximum at the hole due to the strain concentration introduced by the presence of the hole. Clear offsets between the strain profiles especially near the free edge are observed. These offsets characterize the degradation experienced by the sample during its fatigue lifetime. The increase of strain edges is explained by the profusion of microcracks and delamination starting from the free edge at the sides of the specimen because of high interlaminar stresses. Because of the stress concentration at the edge of the hole, the initial failure tends to occur near the hole, which lead to lower the stress concentration and the strain magnitude. A non-consistence of strain variation near the hole is noticeable and this is due to the matrix cracking and delamination phenomena. Even if particular attention is paid to the sample preparation and alignment procedure, some bending components can appear in the sample during the test because of material heterogeneities and because of the non-symmetry of damage processes. Note that the curves are not smooth and do not follow a specific pattern at the transverse edge of the hole due to the complicated damage mechanisms around the hole.

As the number of cycles is further increased in the simulation, matrix damage starts to localize at the hole and then propagates in parallel to the loading direction towards the region of load introduction. This damage accumulation strongly reduces the stress concentration which is introduced by the hole.

The individual curves in Figure 5.5 correspond to the longitudinal strains plotted along the circular section (labeled Section2) at different ratios of fatigue lifetime and at different stress levels corresponding to different damage states. The radius of this circular hole is equal to 8 mm. It can be seen that the increasing axial splits as well as the delamination in between substantially reduces stress concentration. This effect shifts the axial strains gradually towards zero for the arc of Section 2 situated between the axial splits.

Figure 5.5 shows the averaged shear strain profiles along Section2 at different median fatigue lifetime ratios for the three stress levels 70%UTS, 75%UTS and 80%UTS. The magnitude of shear strain at certain angles, corresponding to the four corners of the hole, increases with increasing fatigue life ratio. These shear strains could be used in conjunction with shear strain maps to

determine the critical shear values that exhibit axial splits. These profiles could be used as well and to predict the remaining fatigue lifetime of open-hole composites.

Despite the fact that DIC is a surface method, the presented results illustrate the potentialities of 3D DIC method with high resolution cameras to measure local strain gradients and to give information about the cracking processes during the fatigue lifetime of open hole composites

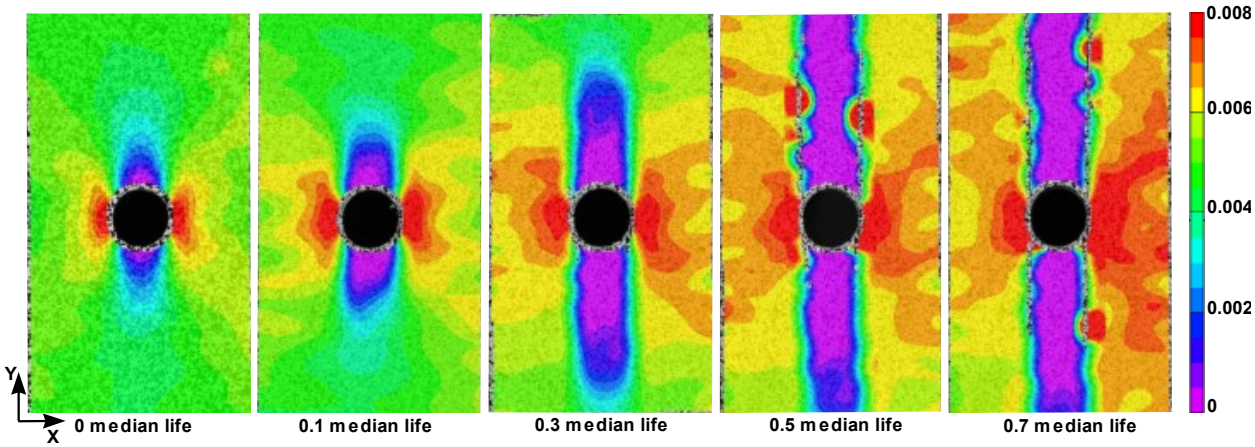

Figure 5.1. Full-field longitudinal strains of a fatigued specimen (with 80% of stress level) at different fatigue lifetime ratios loaded statically at 60% of UTS

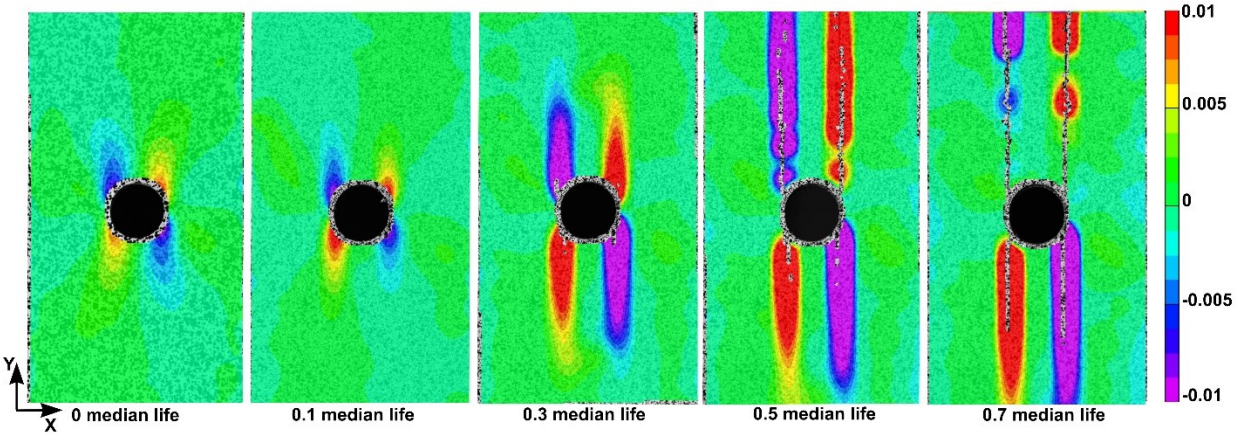

Figure 5.2. Full-field shear strains of a fatigued specimen (with 80% of stress level) at different fatigue lifetime ratios loaded statically at 60% of UTS

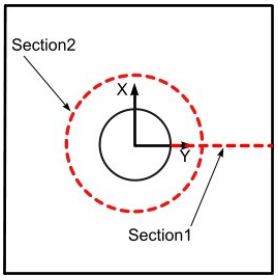

Figure 5.3. Sketch of Section1 and Section2 around the hole

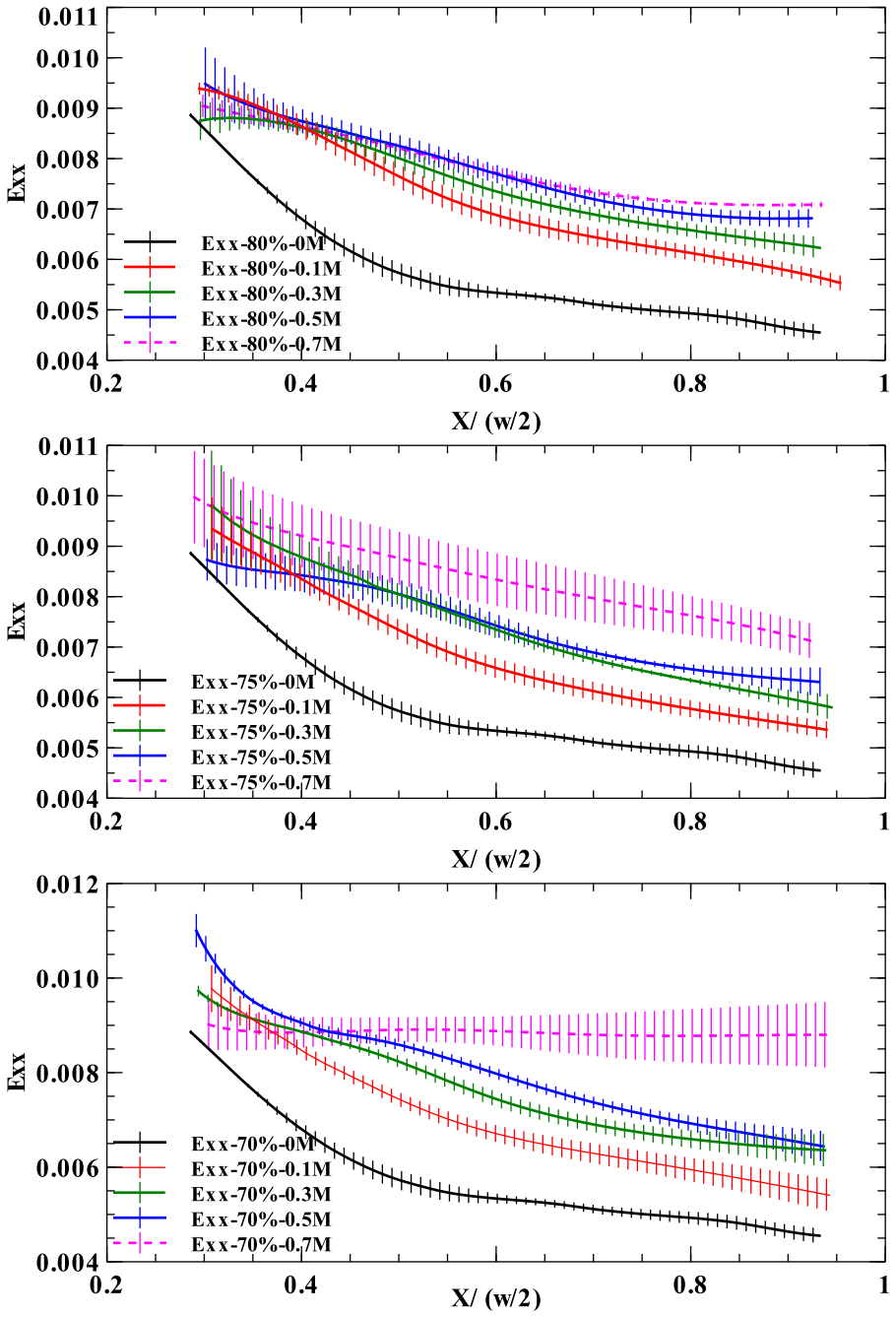

Figure 5.4. Average longitudinal strain profiles along Section1 for different stress levels 70%, 75% and 80% and for various fatigue lifetime ratios

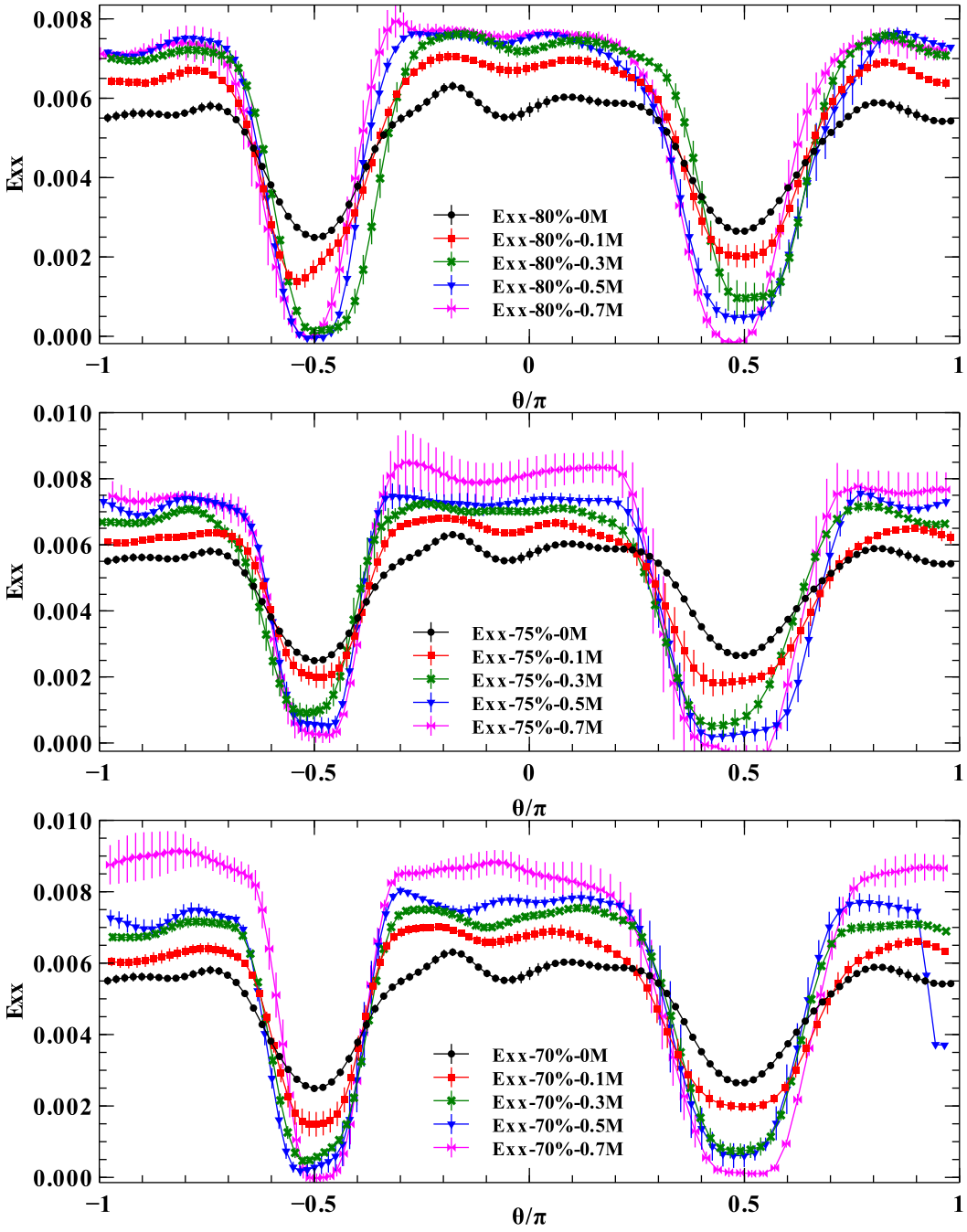

Figure 5.5. Average longitudinal strain profiles along Section2 for different stress levels 70%, 75% and 80% and for various fatigue lifetime ratios

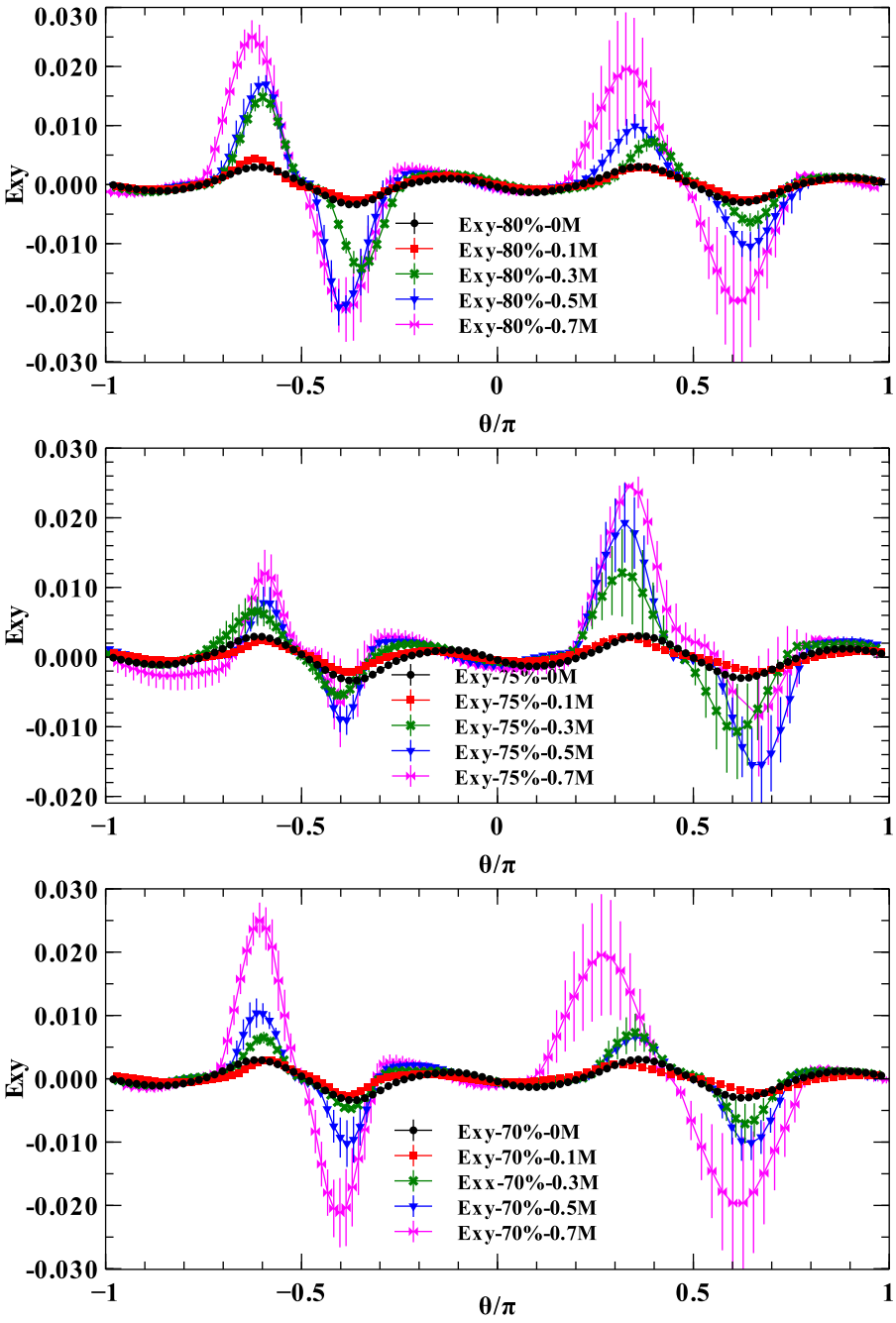

Figure 5.6. Average shear strain profiles along Section2 for different stress levels 70%, 75% and 80% and for various fatigue lifetime ratio

5.4. Vibration results

The presence of fatigue damage causes changes in the natural frequency response signature over the frequency range sampled (up to 6kHz) for the free-fixed boundary condition. Typical

frequency response measurements for one specimen fatigued at different fatigue lifetime ratios is shown in Figure 5.7. The peaks in frequency response correspond to natural vibration modes of the specimen and the shifting in peaks characterize to the impact of fatigue damage level on natural frequencies.

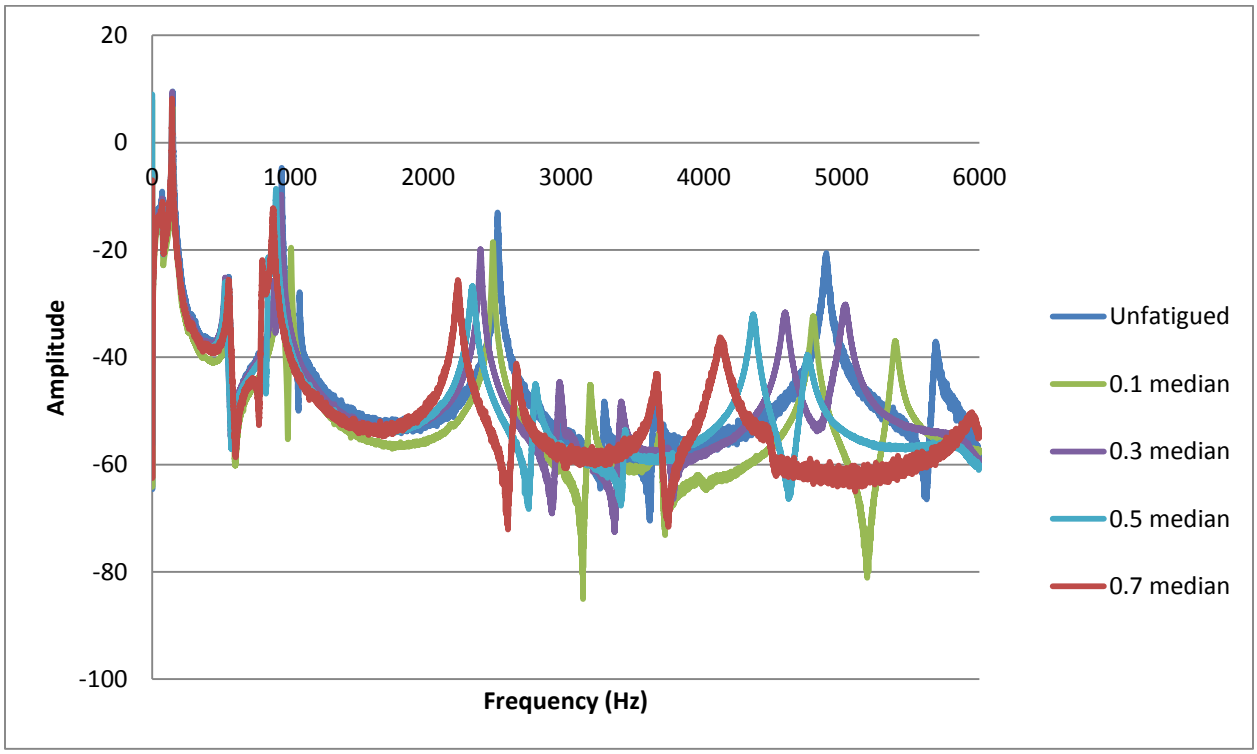

Figure 5.7. Typical frequency responses of a specimen fatigued with 75%UTS at different median fatigue lifetime ratios 0.1M, 0.3M, 0.5M and 0.7M in contrast with its frequency signature at the undamaged state.

Table 5.1, Table 5.2 and Table 5.3 summarize the averaged measured natural frequencies, along with standard deviations, of open-hole composites fatigued with the stress levels 70%, 75% and 80% of the ultimate strength, respectively, over the range analyzed for the fixed-free boundary condition. The natural frequencies decrease gradually with increasing of number of cycles by different amounts depending on the fatigue life ratio, stress level and mode number. This reduction in natural frequencies is expected as the local reduction in structural stiffness caused by the fatigue damage, reduces natural frequency.

To develop a better evaluation of the impact of fatigue damage level on natural frequencies, frequency deviations were plotted for all stress levels as shown in Figure 5.8. The frequency

deviations were calculated as the difference between the natural frequencies of the damaged specimens and unfatigued specimens. The frequency deviations for all mode numbers increase with increasing of median fatigue life ratio. It can be seen from the bar plots that the higher frequencies appear to be the most useful candidates from a damage detection perspective since they demonstrate the greatest sensitivity to damage. Mode 1 appears to be insensitive to fatigue damage progress.

The effect of stress level on the residual dynamic natural frequency response can be extracted from the aforementioned figures. It appears that, for median fatigue life ratios 0.3M, 0.5M and 0.7M and for all modes, the specimen fatigued with 70%UTS stress experience the greatest changes compared to the specimens fatigued with either 75% or 80%UTS. In contrast, for a median fatigue life ratio of 0.1 the specimen fatigued with 70%UTS experience the smallest change compared to the other stress levels and this is valid for all mode shapes. This difference can be explained through the differences between the residual frequencies from the different stress levels at the same median fatigue life time ratio is related to the nature and the development of fatigue damage. The initiated fatigue cracks around the hole at the stress concentration regions propagate extensively to the remaining regions of the specimen and towards the transversal extremities especially for the lowest peak stress level. This led to a progressive reduction in the effective stiffness of open hole composites which is manifested in the gradual reduction in natural frequency.

Moreover, the figure elucidates that the most sensitive modes to fatigue damage are the fifth and the seventh modes which can be potential candidates for monitoring damage especially at early stages.

Table 5.1. Average of the measured frequencies of open-hole composites fatigued with 70%UTS

	0M	0.1M	0.3M	0.5M	0.7M
Mode1	146.817 (2.268)	148 (1.478)	145.6 (1.451)	146.025 (2.578)	141.45 (6.822)
Mode2	946.3 (15.396)	954.1 (12.244)	904.85 (16.666)	867.75 (17.810)	768.55 (70.106)
Mode3	1045.2 (15.184)	1016.15 (12.024)	949.1 (6.983)	928.55 (11.678)	828.1 (86.774)
Mode4	2535.217 (44.338)	2559.05 (39.883)	2429.15 (68.869)	2410.2 (47.361)	2001.3 (401.811)
Mode5	3296.017 (33.287)	3222.75 (19.066)	2969.35 (61.582)	2824.5 (55.980)	2717.2 (26.022)
Mode6	4976.883 (85.247)	4980.7 (69.406)	4722.4 (106.04)	4565.55 (84.626)	4049 (633.8511)
Mode7	5694.15 (74.939)	5545.85 (64.801)	5107.9 (83.309)	4867.65 (63.453)	4382 (478.287)

Table 5.2. Average of the measured frequencies of open-hole composites fatigued with 75%UTS

	0M	0.1M	0.3M	0.5M	0.7M
Mode1	146.8167 (0.902)	147.7 (1.183)	146.15 (1.636)	145.95 (1.3)	145.25 (2.650)
Mode2	946.3 (9.329)	949.3 (16.005)	914.8 (23.800)	877.25 (26.534)	834.1 (32.807)
Mode3	1045.2 (14.74)	1009.75 (4.737)	952.25 (13.915)	933.45 (24.172)	916 (34.480)
Mode4	2535.217 (30.878)	2544.7 (51.844)	2479.35 (70.698)	2440.25 (79.501)	2420.7 (201.63)
Mode5	3296.017 (29.37)	3211.2 (47.518)	2967.6 (17.253)	2833.2 (64.205)	2740.867 (87.209)
Mode6	4976.883 (89.342)	4954.9 (112.475)	4772.05 (137.116)	4627.7 (182.560)	4151.55 (632.8457)
Mode7	5694.15 (54.493)	5507.675 (82.887)	5180 (134.203)	4969.733 (186.833)	4786.867 (280.51)

Table 5.3. Average of the measured frequencies of open-hole composites fatigued with 80%UTS

	0M	0.1M	0.3M	0.5M	0.7M
Mode1	146.8167 (3.284)	147.4 (3.410)	146.6 (2.852)	145.7 (3.631)	146 (2.227)
Mode2	946.3 (8.420)	940.6 (13.599)	907.85 (10.357)	866.55 (21.866)	818.4667 (34.250)
Mode3	1045.2 (20.275)	1002.667 (18.999)	950.95 (11.275)	928 (15.158)	913.5333 (12.624)
Mode4	2535.217 (8.648)	2510.4 (32.285)	2455.45 (39.451)	2413.5 (41.946)	2372.067 (28.375)
Mode5	3296.017 (35.071)	3179.5 (19.092)	2987.65 (107.975)	2689.6 (91.509)	2719.5 (17.394)
Mode6	4976.883 (19.482)	4890.5 (59.443)	4736.7 (95.513)	4583.65 (91.509)	4414.6 (65.317)
Mode7	5694.15 (113.432)	5348.333 (65.498)	5091.05 (97.804)	4916.85 (65.432)	4706.4 (72.973)

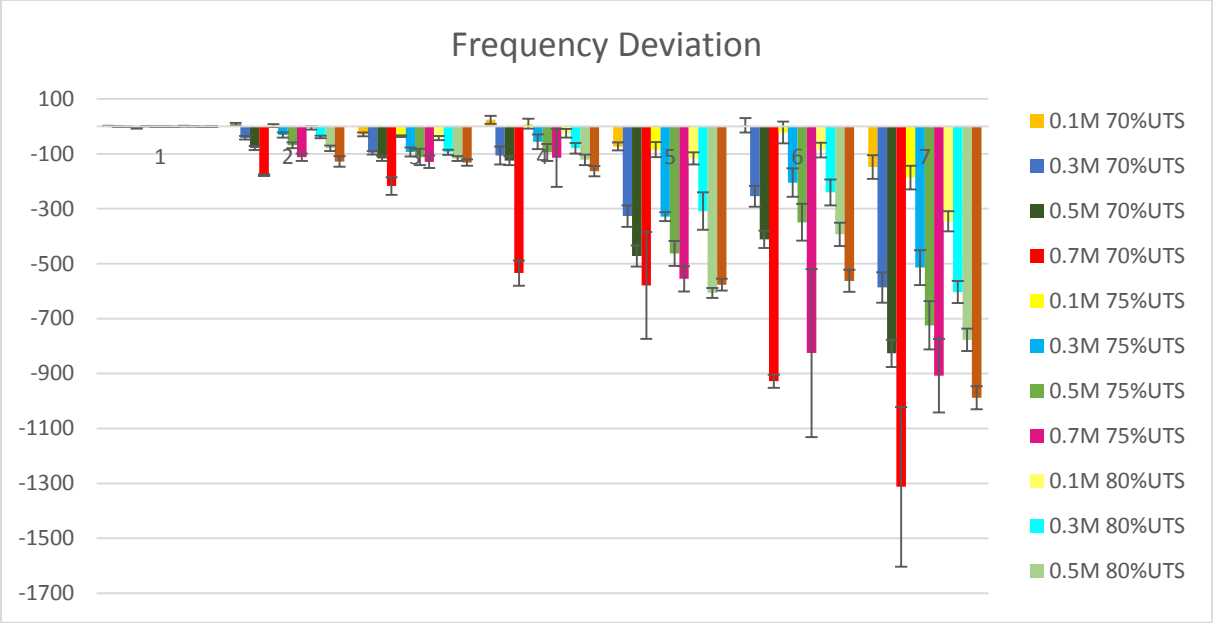

Figure 5.8. Frequency deviation of specimen fatigued with 70%UTS, 75%UTS and 80%UTS

In our situation, we determined the difference between the averaged fatigued natural frequencies $\overline{f}_f$ and the averaged unfatigued frequencies $\overline{f}_u$. A data reduction equation is defined as follows

$$r = r(\overline{f}_f, \overline{f}_u) = \overline{f}_f - \overline{f}_u \qquad (5.1)$$

Where $\overline{f}_f$ and $\overline{f}_u$ are the averaged measured variables. These mean values are determined from N independent measurements of the variable f in the current experiment. The uncertainties in the measured variables cause uncertainty in the result, and this is often modeled using the propagation equation based on Taylor series expansion. The random standard uncertainty of the calculated result is

$$(S_R)^2 = \left(\frac{\partial r}{\partial \overline{f}_f}\right)^2 S_{\overline{f}_f}^2 + \left(\frac{\partial r}{\partial \overline{f}_u}\right)^2 S_{\overline{f}_u}^2 + 2\left(\frac{\partial r}{\partial \overline{f}_f}\right)\left(\frac{\partial r}{\partial \overline{f}_u}\right)\mathrm{cov}\left(\overline{f}_f, \overline{f}_u\right) \qquad (5.2)$$

Where

$\mathrm{cov}\left(\overline{f}_f, \overline{f}_u\right) = \dfrac{\mathrm{cov}\left(f_f, f_u\right)}{N}$ since we have a paired data in which f_f and f_u are correlated.

$S^2_{\overline{f_f}} = \frac{S^2_{f_f}}{N}$ and $S^2_{\overline{f_u}} = \frac{S^2_{f_u}}{N}$.

It should be noted that the covariance factor is multiplied by the partial derivatives $\left(\frac{\partial r}{\partial \overline{f}_f}\right)$ and $\left(\frac{\partial r}{\partial \overline{f}_u}\right)$ which are equal to 1 and -1 respectively. So if the covariance factor is positive the correlation term is negative and the effect of the correlation is to reduce the uncertainty. In the contrary case, the correlation term is positive and the effect of the correlation is to increase the uncertainty. The calculated standards uncertainties, which are applied in the Figure 5.8 by error bars, characterize the extent of variation of the calculated difference by the propagation of random errors into the final result.

5.5. Conclusions

A significant experimental study of the fatigued quasi-isotropic notched composites with different stress levels has been conducted using non-contact measurement tools. The DIC technique was successfully employed to monitor local and global strains, providing critical information on the changes in strain distributions around the hole of the notched composites resulting from damage formation and growth incurred through increasing number of loading cycles for all stress levels.

Various strain components along different sections can be used for validating models to predict remaining fatigue life of open-hole components. It has been shown that the different components at various sections gave different information about the progressive fatigue damage and some of the failure mechanisms. The effect of stress level on the strain distribution has been investigated.

Non-contact vibration measurements were performed on interrupted fatigued specimens to study the effect of fatigue damage on the residual natural frequencies. The results elucidated the importance of tracking higher modes to capture the initiation of damage at early stages of fatigue lifetime as well as the progression of the damage. Specific high modes could be used as potential candidates for monitoring damage throughout fatigue lifetime. The effect of the combination of stress level and fatigue lifetime ratio on the natural frequencies has been investigated. At the low

fatigue life ratio 0.3M the effect of damage is more noticeable in the specimens fatigued with stress levels 70%UTS and 75%UTS compared to 80%UTS. For the other fatigue lifetime ratios 0.5M and 0.7M, the specimens fatigued with 80%UTS experience greater change in natural frequencies compared to the specimens fatigued with 70%UTS and 75%UTS.

Chapter 6. Experimental, numerical, and analytical free vibration analyses of open-hole composite plates

6.1. Abstract

The free vibration behavior of quasi-isotropic carbon fiber laminates containing a center hole with free-clamped boundary conditions is investigated numerically and analytically; the results are validated through subsequent experimentations. Finite element models based on classical plate theory (Kirchhoff) and the shear deformable theory (Mindlin) within the framework of equivalent single-layer and layer-wise concepts as well as the three-dimensional theory of elasticity are developed. These models are created using the finite element software, Abaqus, to determine the natural frequencies and the corresponding mode shapes. In addition, an analytical model based on Kirchhoff plate theory is developed. Using this approach, an equivalent bending-torsion beam model for cantilever laminated plates is extracted taking into account the reduction in local stiffness and mass induced by the center hole. Experimental vibration analyses are carried out using an optically-based vibration measurement tool to extract the frequency response functions (FRFs) and to measure the natural frequencies. Numerical and analytical natural frequency values are then compared with those obtained through experimental vibrational tests, and the accuracy of each finite element (FE) and analytical model type is assessed. It is shown that the natural frequencies obtained using the analytical and FE models are within 8% of the experimentally determined values.

6.2. Introduction

Fiber reinforced polymer (FRP) composite materials are increasingly used not only in aerospace but also in automotive, marine, civil, and even medical applications. This usage is often due to their high strength-to-weight and stiffness-to-weight ratios. In addition, they have excellent chemical and corrosion resistance [74]. Several studies have been performed to examine composite structures with different shapes, sizes and material systems (depending on the application) under different kinds of loading conditions including tensile, compression, impact, fatigue and creep

testing [75-79]. Along with the strength, elastic deformation and other design parameters, a good understanding of the free vibration behavior of composite structures is of great importance in order to obtain reliable predictions of their dynamic response so that we can optimize their response. A multitude number of experimental, analytical and numerical studies have been carried out concerning the free vibration problems of thin or thick isotropic, orthotropic and multilayered composites [80-85]. In this respect, different methods including analytical, semi-analytical and numerical approaches have been developed. The most popular among these are Navier, Lévy, Rayleigh-Ritz, Kantorovich, Galerkin, differential quadrature, finite difference and finite element methods [86]. The first theory used to investigate the behavior of thin plates was the classical plate theory (CPT) which is known as Kirchhoff theory. However, CPT predicts accurate results of flexural vibrations of thin homogeneous plates and gives good results for thin laminated plates and acceptable results for thick laminated plates defined within the equivalent single-layer concept [82]. In general, Kirchhoff theory underestimates deflections and overestimates natural frequencies. The reason behind that is that the transverse shear deformation is omitted in CPT [87]. To overcome the limitations of the CPT for thick plates, the first order shear deformation theory (FSDT) based on Mindlin assumptions is commonly used to study the vibration of thick orthotropic plates. Early finite element models using the FSDT to study the free vibration problem of composite plates modeled as one layer plates showed good results of predicting natural frequencies in comparison to 3D linear elasticity solutions or closed form solutions [88]. However, FSDT does not satisfy the shear stress-free conditions at the top and bottom surfaces of plates. Thus, shear correction factors are needed to alleviate this problem and appropriately take into account the strain energy of shear deformation. Furthermore, higher order shear deformation theories (HSDT) were developed to overcome the need of shear correction factors and automatically satisfy the stress-free boundary conditions. Various HSDT were developed based on various displacement fields within the concept of the single layer plate theory. A summary table of various expressions of expansions of in-plane displacement fields used from 1985 to 2013 can be seen in [86]. Nevertheless, the increase in the order of variation of displacements across the thickness cannot make any significant improvement in representing the behavior of thick multilayered laminates within the equivalent single layer (ESL) concept. Indeed, HSDT gives a continuous variation of shear strain across the thickness, while it is actually discontinuous at layer interfaces [89]; hence, the appearance of the zig-zag and layer-wise theories [90-92]. Indeed, more

accurate results can be obtained for thick multilayered composite plates using the layer-wise (LW) theory where each single layer is modeled using FSDT or HSDT. The displacement functions are chosen such that the continuity of the displacement is assured at the interfaces during the assembly of different layers. A change of slope of transverse normal at the interfaces of different layers is routinely observed after problem resolution [93]. A detailed review of the developed plate theories over the years and the assessment of these theories upon the free vibration predictions of multilayered plates is presented by Carrera in [94-96].

The presence of cutouts (e.g. square, circular, and elliptic holes) is inevitable in structures because of practical considerations. For example, the assembly of structures, providing access to other parts of assemblies, weight management, and alteration of resonant frequencies necessitate the use of such cutouts. Moreover, composite structures under service may be subjected to damage that may be approximated in the form of these cutout shapes. Therefore, the natural frequencies and corresponding modal shapes of such structures are of considerable interest to study. While there is a multitude of vibrational studies with different approaches to composites laminates having embedded delaminations, there is a scarcity of studies involving the free vibration problem of multilayered composites having cutouts. Adding such geometric discontinuities and stress-free surfaces leads to a real complication which is difficult to solve.

Viola et al. [97] investigated the dynamic behavior of moderately thick composite plates with different shapes containing geometric discontinuities through the thickness using the generalized differential quadrature finite element method (GQFEM). The Generalized Differential Quadrature (GDQ) cannot be used by itself to solve problems concerning the dynamic behavior of structures having irregular shapes, so there is a need for FEM to subdivide the whole domain into several sub-domains. Viola et al. compared the computed natural frequencies for composite plates having elliptic holes or slits using GQFEM to FEM results obtained using Abaqus. However, this study was based on FSDT applied to laminates consisting of at most three layers within the ESL approach. Chen and Hwu [98] used the anisotropic elastostatic fundamental solutions and employed the dual reciprocity method along with the boundary element method (BEM) to transform the domain integral to a boundary integral and to obtain the system of ordinary differential equations that describes the vibration problem. The system of equations was solved using Houlbot's algorithm and the modal superposition method. The difference between the natural frequencies of anisotropic plates containing a central hole obtained from the current BEM and the

finite element software Ansys was within 4%. However, due to the use of the particular solutions for the conversion of the domain integral, the boundary conditions of the hole, which are satisfied exactly by the fundamental solutions, are only approximately satisfied. In addition, this study was limited to two-dimensional thin anisotropic plates. Fantuzzi et al. [99] used a strong formulation finite element method (SFEM) based on the radial basis function (RBF) and generalized differential quadrature (GDQ) techniques to conduct the dynamic analyses of multilayered plates of arbitrary shapes. The numerical results in terms of natural frequencies were compared to the literature and finite element results. However, the study was limited to two-dimensional first-order shear deformation theory. Capozucca and Bonci [25] conducted experimental vibration tests on unidirectional CFRP containing double rectangular notches having different sizes and locations. They also developed an analytical model of the simply-supported and double-notched CFRP laminates under free vibration. Analytical frequency values were compared with those obtained experimentally. The differences ranged from 1% to 11% for the first mode and exceeded 11% for higher frequencies with a specific cut size/position. The generality of their analysis is questionable as they neglected the anisotropy of the laminates.

As a result of this review, we note that free vibration analyses of a laminated structure containing a central hole using the CPT and FSDT kinematics within the ESL and LW concepts and 3D elasticity solutions in conjunction with finite element method and subsequent experimental validation are very scarce. In addition, most of the free vibration results obtained by the analytical/numerical models were compared to one or two types of FEM solutions. However, there are different approaches to modeling (ESL and LW) using finite element method and different parameters (type and size of elements and relevant used plate theory) that simultaneously change the accuracy of the computed results and the required computational times. In this work, an attempt is made to develop different finite element models with various approaches and parameters. This will lead to information to guide a proper selection of the appropriate FE model for further comparison with any newly developed analytical/numerical model.

In this study, the finite element methods and analytical models are used to determine the natural frequencies and mode shapes of open-hole composite plates. A mathematical model is developed for a cantilever laminated composite plate with a central hole. The laminate material stiffnesses are estimated according to the ESL theory while the displacement, strain, and stress fields are modeled in the framework of Kirchhoff plate theory. An equivalent one-dimensional laminated

composite beam is derived to model the bending and the torsional modes of the cantilever plate. Two governing differential equations are derived and analytically solved to investigate the bending and torsional behaviors of the cantilever plate. The natural frequencies of a laminated plate with carbon epoxy composite layers are calculated using the proposed FE models and the analytical model and are then compared to the frequencies measured experimentally using a non-contact vibration method. To accomplish this, the remainder of this paper is organized as follows: the experimental setup, modal analyses, and measurements are presented in Section II. In Section III, different finite element methods are shown and discussed. In Section IV, the analytical model based on CPT is developed taking into account the local reduction of the stiffness and mass due to the presence of the central hole. The summary and conclusions are presented in Section V.

6.3. Experimental modal analysis

6.3.1. Preparation of the carbon fiber quasi-isotropic laminates with central hole

Laminated composite panels consisting of carbon fiber Hexcel T650/F584 pre-impregnated tapes in a [0/-45/+45/90]s stacking sequence were cured in a hot press. The recommended curing cycle consisting of a temperature ramp of 3°C/min to 180°C under 690 kPa, holding for 2 hours, then cooling down at room temperature was followed. The panels were subsequently cut into five specimens with a length of 140mm and width of 25mm. A hole with a radius of 3.17mm was introduced at the geometric center of the specimen using a water-cooled tungsten carbide drill bit. Sacrificial front and back plexiglass plates were used to clamp the specimens during the drilling process in an effort to reduce damage from the machining process.

6.3.2. Vibration measurements

Vibration analysis of the composite samples was conducted using a non-contact vibration method. The measurements of displacements were performed using a single point scanning laser Doppler vibrometer (Polytec OFV-505) connected with the modular vibrometer controller (Polytec OFV-5000) with a built-in velocity and displacements decoder. The composite plates were clamped vertically at one end using a fixture mounted to the electrodynamic shaker; the other end was free. Great care was taken to reproduce the clamping force in each test. Indeed, a torque wrench was used to exert the same couple 2.26 Nm on the bolts of the fixture. Before the measurements, a tiny piece of retroreflective copper tape of negligible mass was attached to either

mid or left free-end tip of the cantilevered open-hole composite plate. The samples were excited with a bandwidth-limited random noise excitation signal in the frequency range of 0-6000 Hz using a Ling Dynamics Systems LDS V408 shaker and a LDS PA100E power amplifier. During the tests, the scanning head launched a probe beam to the sample's mid tip (MT) or left tip (LT) and also collected the back-scattered light signal. A National Instruments system with a PXI-4461 (24-bit input-output resolution, 204.8 kS/s sampling rate, 2-input/2-output) and a PXI-4462 (24-bit input-output resolution, 204.8 kS/s sampling rate, 4-input) data acquisition modules with antialiasing filters recorded the velocity from the laser vibrometer and provided the output signal for the shaker as shown in Figure 6.1.

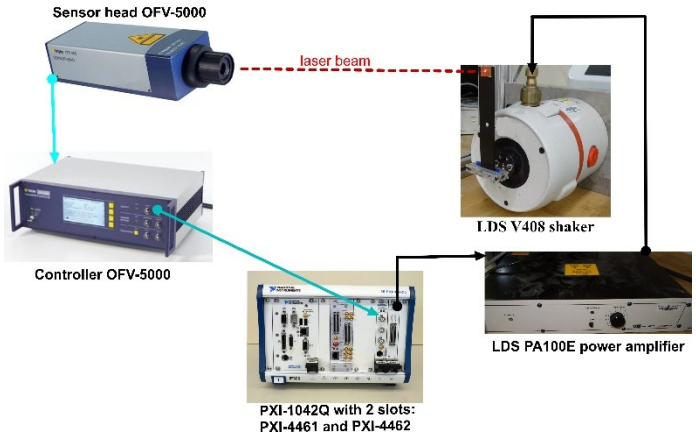

Figure 6.1. Elements of the experimental vibrational setup

The Sound and Vibration Measurement Suite in LabView 2010 was used to calculate the results, display the data, and record the data. The frequency response functions (FRFs) were then computed using the ratio of the tip displacement to the base acceleration. Typical data obtained from one sample at the two measurement locations MT and LT are plotted in Figure 6.2. Every peak in this plot represents a natural frequency of the sample. The averaged measured frequencies of five samples and the corresponding standard errors are presented in Table 6.1 for the two measurement locations.

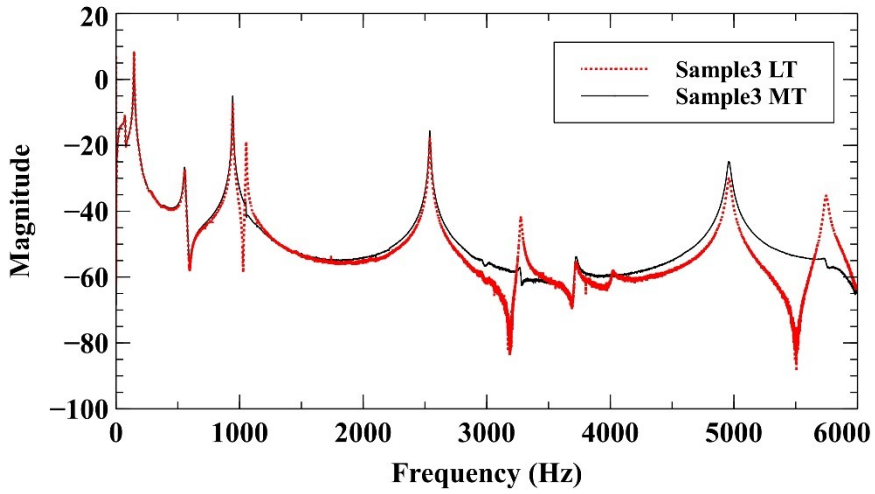

Figure 6.2. Frequency response functions of the same sample extracted from two different single points (mid free tip MT and left free tip LT)

Table 6.1. Measured frequencies (in Hz) at two different single points (MT and LT) at the outer surface of the open hole composites.

	Mode1	Mode2	Mode3	Mode4	Mode5	Mode6	Mode7
Mean LT	148±1	958±7	1049±4	2570±19	3273±15	5020±37	5729±22
Mean MT	148±1	958±7	1053±1	2570±20	3271±15	5020±38	5728±28

6.4. Finite Element Analysis

In this study, three different models were developed using Abaqus 6.14.4 in order to calculate the natural frequencies of the free-clamped quasi-isotropic laminate containing a center hole. The computed results are compared with each other and with the experimentally measured values. The three models are based on (1) the equivalent single-layer theory using conventional shell elements, (2) the layer-wise theory using continuum shell elements, and (3) the three-dimensional approach using continuum solid elements. It should be noted that for all the FE models, the composite laminates are made of perfectly bonded layers of equal thicknesses. The bonding is non-shear-deformable (no lamina can slip relatively to another). In addition, the orientations of fibers for each layer are defined with respect to the stacking sequence [0,-45,+45,90]s by an in-plane rotation angle measured relatively to the global directions of the whole model, as presented in Figure 6.3. The thickness of each Carbon/Epoxy layer is 0.28225 mm. The length and the width of the plate used in the model are equal to 140.29 mm and 25.41 mm respectively. The material properties

used for the composite layers were obtained from [100] and are given as: E1 =156.5 GPa, E2=E3=15.65 GPa, G12=G_{13}=5.19 GPa, G_{23}=1.98 GPa, ν_{12}=0.32, ν_{23}=0.35 and ρ=1770 kg/m^3.

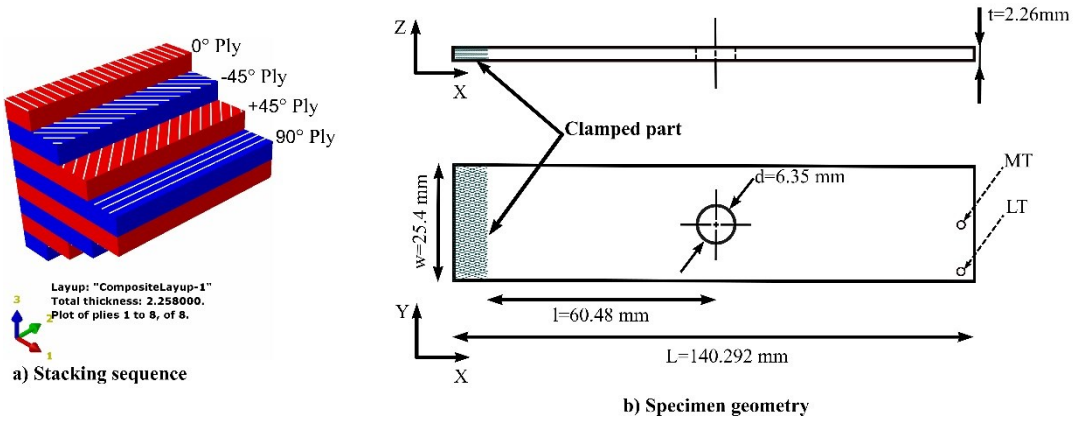

Figure 6.3. Lay-up configuration and used specimen dimensions for the finite element model.

The eigenvalue problem for the natural frequencies and associated mode shapes was solved using the Abaqus/Standard solver where the Lanczos method is implemented. A uniform mesh was adopted for the whole structure. A mesh sensitivity analysis with respect to the element size and the type of the FE model was carried out. The smallest element size was chosen on the basis of either slight insignificant differences between the calculated values of natural frequencies after refinement or on the basis of reasonable computational time. The models were solved on an Intel core i7 4180MQ CPU running at 2.8 GHz with four physical cores and eight threads (eight logical cores) along with 32 GB RAM and a solid state drive (SSD) with sequential read and write speeds of 550 MB/s and 520 MB/s, respectively. It should be mentioned that during each job analysis, 90% of the physical RAM was used for all analyses and 16 GB of disk space was used as a virtual RAM.

6.4.1. Shell model

Shell elements are used to model structures in which one dimension, the thickness, is significantly smaller than the other dimensions in the shell surface. Conventional shell elements use this condition to discretize a body by defining the geometry at a reference surface. The shell theory approximates a three-dimensional continuum with a two-dimensional theory via appropriate kinematic constraints. In the shell models used in this study, the thickness is defined using the

section property definition. Three types of quadrilateral shell elements were utilized: (1) S4R general purpose linear elements, (2) S8R5 thin shell elements, and (3) S8R thick shell quadratic elements [101]. The S4R element uses a mixed finite element formulation where neither pure Kirchhoff nor pure Mindlin theory is used. The S8R5 element is most commonly used for thin laminates since it uses the CPT assumptions. The S8R element is most commonly used for thick plates or in cases where transverse shear flexibility is important and second-order interpolation is desired. When modeling with any of such shell elements, the equivalent single layer concept is employed. Therefore, three sub-models representing the stacking sequence [0/-45/+45/90]s as an equivalent single layer (ESL) were developed using S4R, S8R5, and S8R elements.

6.4.2. Continuum Shell model

Unlike conventional shell elements, the geometry (topology) of continuum shell element resembles solid elements. However, the theory used by these elements is similar to the one used by conventional shell elements. In continuum shell models, the full 3D geometry is specified, and element thickness is defined by the nodal geometry. These elements are able to more accurately capture the through-thickness response and achieve an accurate prediction of transverse shear flexibility for composite laminate structures than conventional shell elements, especially for thick laminates. A model of the eight-layer plate based on eight-node quadrilateral SC8R continuum shell elements was developed. The layer wise (LW) concept is utilized to study the free vibration of the [0/-45/+45/90]s quasi-isotropic laminate via a stacking sequence of continuum shell elements through the thickness. Indeed, each layer across the thickness is represented by one element. This implies each layer is modeled using the FSDT and the slope of displacements at the interfaces changes yielding in a zig-zag behavior of the displacement through the thickness.

6.4.3. 3D model

While orthotropic plates or multi-layered composite plates are typically modeled using appropriate shell elements for the purpose of increasing accuracy for thin plates (high ratio of the span-to-thickness ratio) or rapid estimation of required results, other cases including low span-to-thickness ratios require the use of three-dimensional solid elements with one or several elements through the thickness.

For the current model, 3D hexahedral elements were used to discretize the geometry where one element or two elements were used for each composite layer. In these models, the composite plate was modeled with eight or sixteen elements through the laminate thickness, respectively. The reduced integration linear C3D8R and quadratic C3D20R elements were utilized to perform the free vibration analysis of the open-hole composite plates. First order elements suffer from shear locking. They cannot provide the pure bending solution because they must shear at the numerical integration points to respond with an appropriate kinematic behavior corresponding to the bending. This spurious shear stress arises because the edges of the elements are unable to curve. This shearing locks the element, and the response is too stiff. The use of reduced integration first order elements may alleviate this problem; however, they suffer from hourglassing if the mesh is not fine enough. Consequently, the use of second order elements is more reliable since the displacement interpolation functions are quadratic. However, their use is limited by the additional computational effort required.

6.4.4. Finite element results

In order to evaluate the effectiveness of different types of finite element models for free vibration analysis, equivalent single layer (ESL), layer wise (LW), and 3D models representing the clamped-free open-hole composite plate were developed. The numerical models were built to represent the experimental geometry, stacking sequence, and boundary conditions. A comparison is then made between the results obtained by the FEM results and the experimental ones.

The plots in Figure 6.4 show the convergence rate of the finite element solutions obtained with different models for the first seven bending and torsion natural frequencies as a function of element size and geometric order. The 3D model with first-order elements was the most sensitive to element size variation. The computational time of each model as a function of an element size is also shown in the latter graph of Figure 6.4. The results show a rapid convergence as the size of element decreased (total number of elements and DOFs increased) and approached 1mm. It follows from the plots in Figure 6.4 that, in general, fine meshing tends out to lead to lower values of natural frequencies whereas coarser mesh leads to the structure to perform more rigidly, as expected.

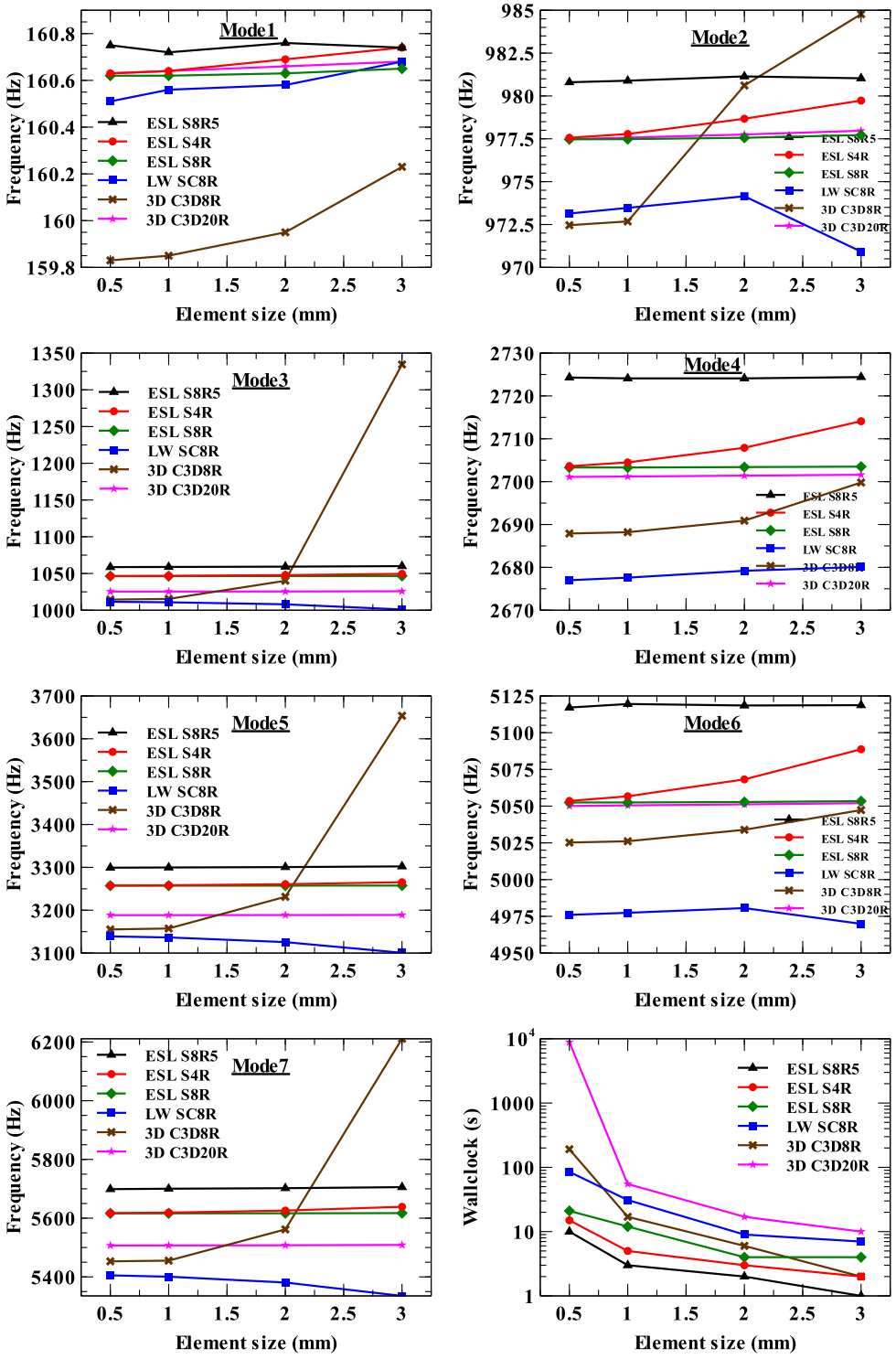

Figure 6.4. Variations of the seven natural frequencies and computation time with respect to the size of the element.

The natural frequencies for the element size of 0.5mm for each model type are given in Table 6.2 and compared to the experimental measurements of the modal frequencies. It is clear that the discrepancy between the numerical results for all FE models and element types with respect to experimental results does not exceed 8%. The highest difference of 8% is obtained for the first mode. Good agreement is also noted between the calculated and measured frequencies for higher-order modes, which supports the fact that the current FE models can predict the vibrational response of the open-hole composite plate with accuracy. The upper and lower bounds of most FE models are the CPT shell model within the ESL concept and the FSDT continuum shell model within the LW concept respectively. The percentage difference between the upper and lower bounds are 0.57%, 0.85%, 4.45%, 1.73%, 4.36%, 2.75% and 5.15% respectively for Mode 1 to 7. These percentage deviations emphasize the need of development of different FE models for the selection of the appropriate model and comparison or evaluation of any developed analytical/numerical model.

Furthermore, the use of ESL and LW models involving FSDT with the use of thick second-order shell elements S8R and continuum shell elements SC8R gives accurate results which are comparable with the 3D solutions resulting from the models with linear (C3D8R) or quadratic (C3D20R) solid elements. Nonetheless, the 3D models require higher computational effort compared to the models involving the FSDT within the ESL or LW approach. As a result, the use of the LW approach along with the FSDT, where each layer is discretized with one continuum shell element SC8R across the thickness, more accurately captures variations of transverse shear deformation and provides realistic in-plane displacements through the whole laminate thickness which yield not only accurate predictions of natural frequencies but also local vibration responses in reasonable computational times in comparison with the 3D models. Furthermore, the accuracy can be increased when using the layer-wise approach by creating fictitious interfaces between the layers where each single layer is split into two or more sublayers yielding a nonlinear displacement behavior across the thickness of each layer. Inspecting the last graph of Figure 6.4, one sees that the use of 3D models requires significantly greater computational resources than the other models. In addition, the increase in the number of elements through the thickness, by representing each layer with two solid elements across the thickness, did not yield a noticeable change in the results for our current span-to-thickness configuration.

Furthermore, the ESL model developed with the general-purpose first-order S4R shell elements gives comparable results to the ESL model developed with second order elements S8R but with slightly less computational time. The plate model involving the CPT with S8R5 shell elements within the ESL approach gives sufficiently accurate results for the current thin open-hole laminate since the percentage difference is still within 0 to 8% when compared to all other models. This result is consistent with that seen in [82] for orthotropic thin plates with high aspect ratios. Nevertheless, the frequencies obtained by the latter model are higher compared to all frequencies obtained by the other models. This is as expected due to neglecting the transverse shear effect. The mode shapes associated with the computed natural frequencies for the open-hole composite plates were also found, and nodal lines were located, as shown in Figure 6.5. The nodal lines of an eigenfunction of a plate are lines on the plate where there is little or no movement (zero displacement) when the plate is excited at a natural frequency. The mode shapes explain why the mid-tip measurement location does not identify some of the torsional natural frequencies.

Table 6.2. Comparison of experimental and FE frequency values (Hz) for the open hole composite along with the variation percentage. The percentage values in brackets indicate the difference between the calculated and averaged measured frequency values.

	Mode1	Mode2	Mode3	Mode4	Mode5	Mode6	Mode7
Experimental results	148.4	957.85	1048.9	2570	3272.5	5019.75	5728.65
FE shell model S8R5 (Equivalent single layer)	160.75 (-8.32)	980.80 (-2.39)	1058.7 (-0.93)	2724.3 (-6)	3299.2 (-0.81)	5117.1 (-1.93)	5698.8 (0.52)
FE shell model S4R (Equivalent single layer)	160.63 (-8.24)	977.56 (-2.05)	1046.5 (0.22)	2703.6 (-5.19)	3257.5 (0.45)	5053.5 (-0.67)	5617.1 (1.94)
FE shell model S8R (Equivalent single layer)	160.62 (-8.23)	977.47 (-2.04)	1046.4 (0.23)	2703.3 (-5.18)	3257.2 (0.46)	5052.4 (-0.65)	5616.4 (1.95)
FE shell model SC8R (Layer wise model)	160.51 (-8.1)	973.14 (-1.59)	1011.5 (3.56)	2677 (-4.16)	3139 (4.07)	4976 (0.87)	5405.3 (5.64)
FE 3D model C3D8R (1 Element per ply)	159.83 (-7.7)	972.46 (-1.52)	1014.5 (3.27)	2687.9 (-4.58)	3155.1 (3.58)	5025.2 (-0.1)	5453 (4.81)
FE 3D model C3D20R (1 Element per ply)	160.63 (-8.24)	977.48 (-2.04)	1025.4 (2.24)	2701.1 (-5.1)	3188.5 (2.56)	5050.1 (-0.6)	5506.9 (3.87)
FE 3D model C3D8R (2 Elements per ply)	160.43 (-8.1)	976.25 (-1.92)	1022.9 (2.47)	2679.8 (-4.27)	3180.8 (2.8)	5044 (-0.48)	5494.1 (4.09)
FE 3D model C3D20R (2 Elements per ply)	160.63 (-8.24)	977.45 (-2.04)	1025.4 (2.24)	2701.1 (-5.1)	3188.4 (2.56)	5049.9 (-0.6)	5506.6 (3.87)

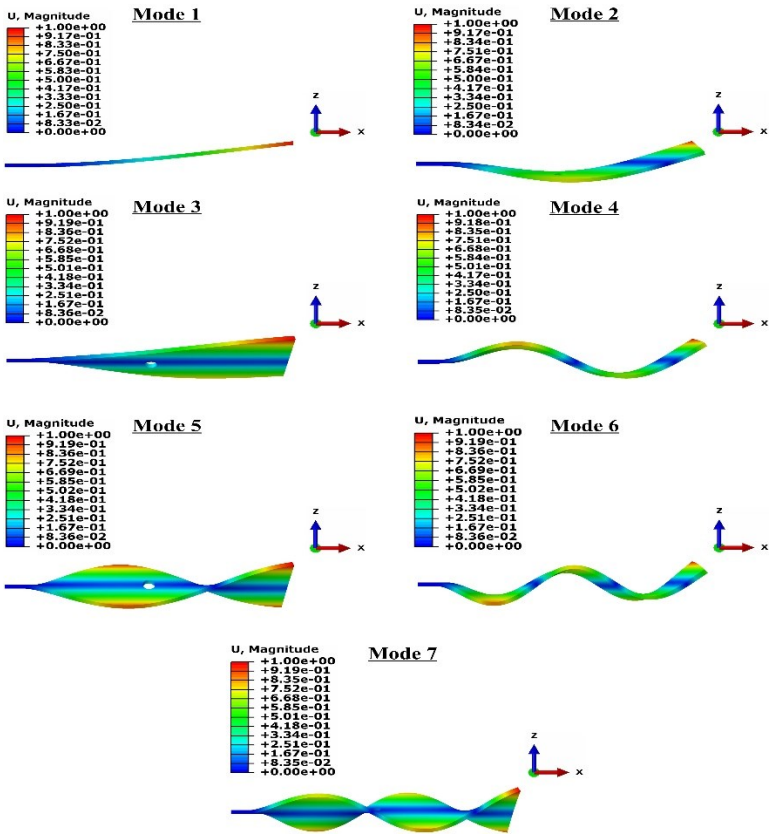

Figure 6.5. Mode shapes for the open hole composite.

6.5. Analytical Modeling

A mathematical model is developed for a cantilever laminated composite plate with a central hole. The laminate material stiffnesses are estimated according to the Equivalent Single Layer (ESL) theory while the displacement, strain, and stress fields are modeled in the framework of Kirchhoff plate theory. The cantilever plate under consideration is schematically shown in Figure 6.6 where the proposed analytical model accounts for both the bending and torsional modes of the plate. According to the plate setup, shown in the Figure 6.6, the plate can be modeled as a one-dimensional laminated beam. By deriving the equivalent bending and torsional rigidities of the beam, two governing differential equations are derived to model the bending and the torsional behaviors of the cantilevered plate.

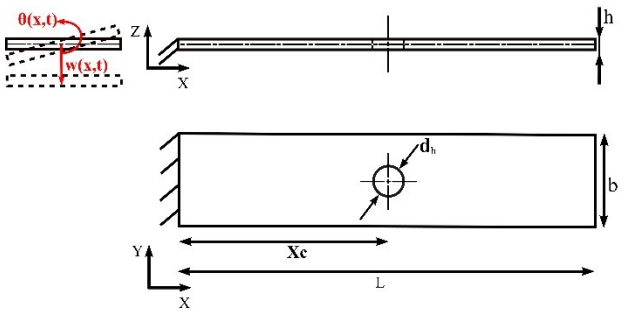

Figure 6.6. Geometries and modes of vibrations of a cantilever plate with a central circular hole

6.5.1. Modeling of the plate using Kirchhoff theory

The displacement field of plate structures with transverse vibrations according to Kirchhoff plate assumptions are defined as follows:

$$u_x(x,y,z,t) = -z\bar{w}_{,x}(x,y,t)\ , u_y(x,y,z,t) = -z\bar{w}_{,y}(x,y,t)\ , u_z(x,y,z,t) = \bar{w}(x,y,t) \tag{6.1}$$

where $\bar{w}(x,y,t)$ is the plate deflection. Accordingly, the plate's strain field is defined as follows:

$$\bar{\varepsilon}_{xx}(x,y,z,t) = -z\bar{w}_{,xx}(x,y,t)\ ;\ \bar{\varepsilon}_{yy}(x,y,z,t) = -z\bar{w}_{,yy}(x,y,t)\ ;\ \bar{\varepsilon}_{xy}(x,y,z,t) = -z\bar{w}_{,xy}(x,y,t) \tag{6.2}$$

The plate under consideration is composed of stacked orthotropic composite layers. Therefore, the constitutive relations for each individual orthotropic k^{th} layer can be defined as follows:

$$\begin{Bmatrix}\sigma_{xx}(x,y,z,t)\\ \sigma_{yy}(x,y,z,t)\\ \sigma_{xy}(x,y,z,t)\end{Bmatrix}^{(k)} = -z\begin{bmatrix}\bar{Q}_{11} & \bar{Q}_{12} & \bar{Q}_{16}\\ \bar{Q}_{12} & \bar{Q}_{22} & \bar{Q}_{26}\\ \bar{Q}_{16} & \bar{Q}_{26} & \bar{Q}_{66}\end{bmatrix}^{(k)}\begin{Bmatrix}\bar{w}_{,xx}(x,y,t)\\ \bar{w}_{,yy}(x,y,t)\\ 2\bar{w}_{,xy}(x,y,t)\end{Bmatrix}^{(k)} \tag{6.3}$$

where σ_{ij} are the in-plane stress components.

In the framework of the equivalent single layer theory, the laminate constitutive equations can be defined as:

$$\begin{Bmatrix}\bar{M}_{xx}(x,y,z,t)\\ \bar{M}_{yy}(x,y,z,t)\\ \bar{M}_{xy}(x,y,z,t)\end{Bmatrix} = -\begin{bmatrix}D_{11} & D_{12} & D_{16}\\ D_{12} & D_{22} & D_{26}\\ D_{16} & D_{26} & D_{66}\end{bmatrix}\begin{Bmatrix}\bar{w}_{,xx}(x,y,t)\\ \bar{w}_{,yy}(x,y,t)\\ 2\bar{w}_{,xy}(x,y,t)\end{Bmatrix} \tag{6.4}$$

where $\bar{Q}_{ij}$ are the transformed reduced stiffnesses which are obtained by the transformation of the plane stress stiffnesses of each lamina from the local to the global Cartesian coordinates. D_{ij} are

the bending stiffnesses of the whole laminate presented to convert the laminate to an equivalent single layer [102].

The stress resultants defined in equation (4) are related to the plate stress components by:

$$\bar{M}_{ij}(x,y,t) = \int_{-h/2}^{h/2} z\sigma_{ij}(x,y,z,t)dz \tag{6.5}$$

6.5.2. Equivalent bending-torsional beam model for cantilever laminated plates

In this section, our objective is to derive the governing equations for cantilever plates under bending and torsional vibrations. It is clear from Figure 6.6 that the plate has negligible displacements in y −direction. Consequently, the plate can be modeled as a one-dimensional beam structure. To capture the bending and the torsional modes of the laminate vibrations, it follows from Figure 6.7 that the beam deflection, $w(x,t)$, and the beam torsion, $\theta(x,t)$, are related to the plate deflection, $\bar{w}(x,y,t)$ by:

$$\begin{aligned} w(x,t) &= \bar{w}(x, y = b/2, t) \\ \theta(x,t) &= \bar{w}_{,y}(x, y = b/2, t) \end{aligned} \tag{6.6}$$

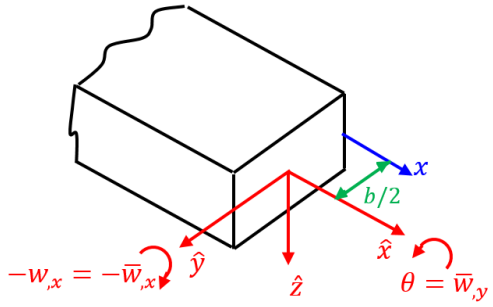

Figure 6.7. Bending and torsional modes of the equivalent beam.

Considering these relations in equation (6), the strain field of the plate is also reduced to form the strain field of the equivalent beam with both bending and torsional vibrations as follows:

$$\varepsilon_{xx}(x,z,t) = -zw_{,xx}(x)\ ;\ \varepsilon_{yy}(x,z,t) = 0\ ;\ \varepsilon_{xy}(x,z,t) = -z\theta_{,x}(x) \tag{6.7}$$

According to the plate and the beam theories, the beam bending stress resultants, M_{ij}, in terms of the plate bending resultants, $\bar{M}_{ij}$, are defined by:

$$M_{ij} = b\bar{M}_{ij} \tag{6.8}$$

By substituting equations (7) and (8) into equation (4) and then by taking the inverse of the resulted equation, the beam deflection and torsion in terms of the beam bending and torsional moments can be expressed as:

$$\begin{Bmatrix} w_{,xx}(x,t) \\ 0 \\ 2\theta_{,x}(x,t) \end{Bmatrix} = -\frac{1}{b}\begin{bmatrix} D_{11}^* & D_{12}^* & D_{16}^* \\ D_{12}^* & D_{22}^* & D_{26}^* \\ D_{16}^* & D_{26}^* & D_{66}^* \end{bmatrix}\begin{Bmatrix} M_{xx}(x,t) \\ 0 \\ M_{xy}(x,t) \end{Bmatrix} \tag{6.9}$$

where $M_{yy}(x,t)$ is omitted by definition. D_{ij}^* are the components of the inverse of the bending stiffness matrix.

Applying the Hamilton's principle, the differential equations that govern the beam bending and torsional modes of free vibration can be obtained in terms of the stress resultants:

$$\begin{aligned} &M_{xx,xx} - m\ddot{w} = 0 \\ &-2M_{xy,x} - \frac{b^3}{12}\int_{-\frac{h}{2}}^{\frac{h}{2}} \rho(z)dz\,\ddot{\theta} = 0 \end{aligned} \tag{6.10}$$

where $m = b\int_{-h/2}^{h/2}\rho(z)\,dz$ denotes the beam mass per unit length and $\rho(z)$ is the beam mass density. According to the beam and torsional bar theories, the bending and the torsional moments can be defined as follows:

$$\begin{aligned} M_{xx} &= -(EI)_{eq}w_{,xx} \\ M_{xy} &= -2(GJ)_{eq}\theta_{,x} \end{aligned} \tag{6.11}$$

where $(EI)_{eq}$ and $(GJ)_{eq}$ are the equivalent bending and torsional rigidities, respectively. Substituting equation (11) into equation (10), the governing equations in terms of the beam deflection and torsion are:

$$\begin{aligned} &(EI)_{eq}\nabla^4 w + m\ddot{w} = 0 \\ &4(GJ)_{eq}\nabla^2\theta - \frac{b^3}{12}\int_{-\frac{h}{2}}^{\frac{h}{2}} \rho(z)dz\,\ddot{\theta} = 0 \end{aligned} \tag{6.12}$$

With the aid of equations (9) and (11), the two rigidities are derived in terms of the plate bending stiffnesses to be in the form:

$$(EI)_{eq} = \frac{b}{D_{11}^* - \frac{D_{16}^* D_{12}^*}{D_{26}^*}}$$
$$(GJ)_{eq} = \frac{b}{D_{66}^* - \frac{D_{16}^* D_{26}^*}{D_{12}^*}} \quad (6.13)$$

It should be mentioned that the rigidities are derived in this form to account for the bending-torsion coupling and to satisfy the condition presented in the second equation of equation (9).
The boundary conditions for the plate (beam) under consideration are given by:

$$w(x = 0) = 0,\ \theta(0) = 0,\ w_{,xx}(L) = 0, \text{ and } \theta_{,x}(L) = 0 \quad (6.14)$$

6.5.3. Eigenvalue problem analysis

An eigenvalue problem is needed to determine the natural frequencies and associated mode shapes of the considered structure. To this end, the beam deflection and torsion are decomposed as:

$$w(x,t) = \sum_{n=1}^{\infty} \varphi_n(x) e^{I\omega_n t}$$
$$\theta(x,t) = \sum_{n=1}^{\infty} \psi_n(x) e^{I\Omega_n t} \quad (6.15)$$

where $\varphi_n(x)$ and $\psi_n(x)$ are two mode shape functions defined to model the bending and the torsional modes of vibration, respectively. ω_n is the nth bending mode natural frequency while Ω_n is the nth torsional mode natural frequency. The general solutions of the two differential equations (12) that satisfy the boundary conditions in equation (14) are expressed in the following form:

$$\varphi_n(x) = A_b \left(\left(\cosh\left(\frac{\lambda_n}{L}x\right) - \cos\left(\frac{\lambda_n}{L}x\right) \right) - \frac{\sinh(\lambda_n) - \sin(\lambda_n)}{\cosh(\lambda_n) + \cos(\lambda_n)} \left(\sinh\left(\frac{\lambda_n}{L}x\right) - \sin\left(\frac{\lambda_n}{L}x\right) \right) \right) \quad (6.16)$$
$$\psi_n(x) = A_t \sin\left(\frac{n\pi}{2L}x\right) \text{ with } n = 1,3,5, \ldots$$

where λ_n for the first five bending modes are: 1.8751, 4.6940, 7.8547, 10.9955, 14.1372. A_b and A_t are the two amplitudes for the bending and the torsional modes, respectively.

Using the Galerkin discretization ($w(x,t) = \sum_{n=1}^{\infty} \varphi_n(x)\, u_n^b(t)$ and $\theta(x,t) = \sum_{n=1}^{\infty} \psi_n(x) u_n^t(t)$) and then multiplying the expressions in equation (12) by the shape functions (equation (16)) and integrating over the beam length leads to the uncoupled form of the equations of motion:

$$\begin{aligned} &\sum_{n=1}^{\infty} M_n^b \ddot{u}_n^b(t) + \sum_{n=1}^{\infty} K_n^b u_n^b(t) = 0 \\ &\sum_{n=1}^{\infty} M_n^t \ddot{u}_n^t(t) + \sum_{n=1}^{\infty} K_n^t u_n^t(t) = 0 \end{aligned} \tag{6.17}$$

where $u_n^b(t)$ and $u_n^t(t)$ are the bending and the torsional nth modes of vibrations, respectively. M_n and K_n are the equivalent mass and the equivalent stiffness of the beam where the subscript "b" and "t" stand for the bending and the torsional modes, respectively. These equivalent masses and stiffnesses can be defined for the two modes as follows:

$$\begin{aligned} M_n^b &= b \int_0^L \left(\int_{-h/2}^{h/2} \rho(z) dz \right) \varphi_n(x) \varphi_n(x) dx \\ M_n^t &= b \int_0^L \left(\int_{-h/2}^{h/2} \rho(z) dz \right) \psi_n(x) \psi_n(x) dx \\ K_n^b &= \int_0^L (EI)_{eq} \nabla^4 \varphi_n(x) \varphi_n(x) dx \\ K_n^t &= \int_0^L 4(GJ)_{eq} \nabla^2 \psi_n(x) \psi_n(x) dx \end{aligned} \tag{6.18}$$

Consequently, the natural frequency of the nth bending and torsion modes can be obtained, respectively, as follows:

$$\omega_n = \sqrt{\frac{K_n^b}{M_n^b}} \quad \text{and} \quad \Omega_n = \sqrt{\frac{K_n^t}{M_n^t}} \tag{6.19}$$

The natural frequencies of the bending and torsional modes of the laminated composite plate with no hole discontinuities can be easily obtained using the expressions in equation (19). However, the plate under consideration has a central hole which affects the plate conventional frequencies. The hole contributes to the plate's frequencies by decreasing its equivalent stiffness and mass. The

reductions in the equivalent stiffnesses, $\widehat{K}_n^b$ and $\widehat{K}_n^t$, of the plate due to the inclusion of the hole are derived as follows:

$$\widehat{K}_n^b = \int_{d_1}^{d_2} (EI)_{eq}^h \nabla^4 \varphi_n(x)\varphi_n(x)dx \quad \text{with } (EI)_{eq}^h = \frac{d_h}{D_{11}^* - \frac{D_{16}^* D_{12}^*}{D_{26}^*}}$$
$$\widehat{K}_n^t = \int_{d_1}^{d_2} 4(GJ)_{eq}^h \nabla^2 \psi_n(x)\psi_n(x)dx \quad \text{with } (GJ)_{eq}^h = \frac{d_h}{D_{66}^* - \frac{D_{16}^* D_{26}^*}{D_{12}^*}} \tag{6.20}$$

where $d_2, d_1 = x_c \pm \frac{d_h}{2}$. $x_c \approx \frac{L}{2}$ represents the location of the central hole along the x-axis. The reduction in the stiffnesses are determined by integrating the local stiffnesses along the hole diameter, d_h.

In addition, the reduction of the equivalent masses of the plate due to the hole are:

$$\widehat{M}_n^b = M_n^b \frac{\pi d_h^2}{Lb}$$
$$\widehat{M}_n^t = M_n^t \frac{\pi d_h^2}{Lb} \tag{6.21}$$

Finally, the natural bending and torsional frequencies of plates with circular holes are, respectively, given by:

$$\omega_n = \sqrt{\frac{K_n^b - \widehat{K}_n^b}{M_n^b - \widehat{M}_n^b}} \text{ and } \Omega_n = \sqrt{\frac{K_n^t - \widehat{K}_n^t}{M_n^t - \widehat{M}_n^t}} \tag{6.22}$$

It should be noted that equations (20) and (21) are derived based on the assumption that the size of the hole is small in comparison with the plate's in-plane dimensions.

Next, two examples are considered to discuss the applicability of the proposed model to perform the frequency analysis of isotropic and anisotropic laminated plates.

A. Results and discussions

Two plates with central circular holes are considered to validate the proposed equivalent beam model. First, the natural frequencies of an isotropic plate made of silicon with $E = 169$ GPa, $\nu = 0.064$, and $\rho = 2300\ kg/m^3$ are calculated using the proposed mathematical model and compared to finite element results, as shown in Table 6.3. The geometric dimensions of the considered isotropic plate are relevant to the parameters in Figure 6.6 with $x_c = 70$ mm, $d_h = 6.5$ mm, $b = 25$ mm, $L = 140$ mm and $h = 3$mm. Inspecting the results presented in Table 6.3 and Figure 6.8,

it is clear that the proposed analytical model gives very good results when compared with the finite element model.

Table 6.3. Frequency analysis (in Hz) of an isotropic cantilever plate with a central hole.

Mode	Present Model	Finite Element	Difference %
1	211.42	211.47	0.024
2	1312.15	1313.5	0.103
3*	2503.85	2470.1	-1.36
4	3718.53	3699.7	-0.51
5	7199.07	7167.2	-0.44
6*	7510.07	7508.4	-0.022
7	12042.3	11856	-1.57
8*	12514.8	12723	1.64

* *Torsional modes*

After validating the isotropic case, the eigenvalue analysis of the laminated composite plate with carbon epoxy composite layers presented in Figure 6.3 is reconsidered using the proposed model. Table 6.4 shows the validity of the proposed mathematical model when compared with the experimental and the finite element results. Clearly, a very good agreement is obtained between the developed analytical model and the experimental measurements. Indeed, a maximum error of 8% is detected for the seventh natural frequency. Figure 6.8 compares the modal shape displacements of FE solutions and proposed analytical model. A good agreement is also noticed for the displacement profiles.

These two examples demonstrate the validity of the proposed analytical model which can replace the finite element and the experimental models for laminated composite plates with initial discontinuities. The proposed model can be used to study the free vibration behaviors of composite plates with central holes in an easy and efficient way when compared with the FE solutions.

Table 6.4. Frequency analysis (in Hz) of the anisotropic cantilever plate with carbon epoxy layers containing a central hole; comparison with the experimental and the FE results.

Mode	Present Model	Experiment	FE 3D model C3D20R (2 Elements per ply)	FE shell model S4R (ESL)
1	152.77	148.4 (-2.94)[1]	160.63 (4.89)[2]	160.63 (4.89)[3]
2	949.73	957.85 (0.85)	977.45 (2.84)	977.56 (2.84)
3*	1051.53	1048.9 (-0.25)	1025.4 (-2.55)	1046.5 (-0.48)
4	2686.9	2570 (-4.55)	2701.1 (0.53)	2703.6 (0.62)
5*	3162.54	3272.5 (3.36)	3188.4 (0.81)	3257.5 (2.92)
6	5215.26	5019.75 (-3.89)	5049.9 (-3.27)	5053.5 (-3.2)
7*	5242.4	5728.65 (8.48)	5506.6 (4.79)	5617.1 (6.67)

* *Torsional modes*

[1] *Difference % between the proposed model results and the experimental results*

[2] *Difference % between the proposed model results and the FE 3D model results.*

[3] *Difference % between the proposed model results and the FE ESL model results.*

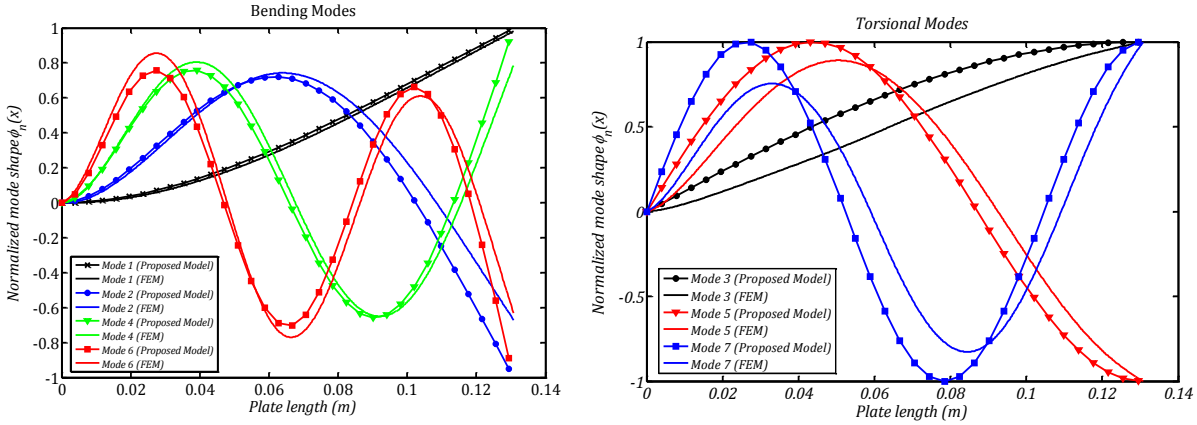

Figure 6.8. Normalized mode shapes of the cantilever anisotropic plate with a central hole. (The normalized bending mode shape is $\boldsymbol{\phi_n(x) = \varphi_n(x)/A_b}$ and the normalized torsional mode shape is $\boldsymbol{\Psi_n(x) = \psi_n(x)/A_t}$)

6.6. Conclusions

The vibration analysis of carbon fiber epoxy laminated composite plates containing a hole in the center is numerically, analytically, and experimentally carried out. Different finite element plate models based on the classical plate theory (CPT), the first shear deformation theory (FSDT), and the three-dimensional elasticity solutions have been developed. The accuracy of each model was valued based on the comparison with experimental results. Moreover, the convergence rate and the numerical efficiency of all developed FE models were also shown. In addition, an analytical model has been developed to determine the natural frequencies and mode shapes of the composite plate with a central hole. In this analytical modeling, an equivalent bending-torsion beam model for cantilever laminated plate was estimated taking into account the reduction in the local stiffness and mass of the plate induced by the central hole. The results showed that excellent agreements are obtained between the measured natural frequencies and the computed ones from all finite element and analytical models with the relative percentage errors ranging from 0% to 8%. The analytical model, as well as the ESL models created with FSDT S8R shell elements or general-purpose S4R shell elements and the LW model created via the stacked through-the-thickness FSDT SC8R continuum shell elements, give accurate results that are comparable with the results obtained by the 3D models based on linear C3D8R or quadratic C3D20R elements. Nevertheless, considering both the accuracy and computational time required by all models the proposed analytical model and former ESL and LW models should be used instead of 3D models for subsequent dynamic analysis or parametric study of free vibration analysis for such open-hole composite structure and material system. Besides, the quadratic order of elements is also preferred over the linear ones since the former ones converge very quickly and do not require refinement as much as the linear ones do. Furthermore, even if the current ESL model created with thin shell elements S8R5 endowed by the CPT has higher natural frequencies compared to the all other models, it is still very suitable for performing the free vibration analysis of the current laminate aspect ratio and material orthotropy. The ESL models involving either the CPT or the FSDT adequately predict the natural frequencies, but it is compulsory to use the LW models if predictions of local or interlaminar vibration responses are required.

In summary, the finite element and analytical models were validated by comparing the calculated natural frequencies against those measured experimentally using a laser vibrometer and comparing mode shape profiles against each other. Thereby, the current numerical and analytical results

obtained and validated by such experiments could be considered as benchmark solutions for further models assessment.

Chapter 7. General Conclusions and Future Work

7.1. General Conclusions

In recent years, optical measurement techniques have led to major advances in experimental mechanics. Their application to damage investigation in CFRP laminates has been addressed in the present work. In the first two chapters, the evaluation of strain distribution in composite plates with an open hole subjected to uniaxial tensile loading was examined using Digital Image Correlation (DIC), an optical full-field strain measurement technique. The strain measurements were compared to the results obtained from two finite element models developed using Abaqus, one of them is based on micromechanics and the other on the Matzenmiller damage approach and Hashin failure criteria.

Next, DIC was used to monitor the local and global changes of strain distributions of open-hole composites under tension-tension fatigue. The high localized strains identified by the DIC technique were also in good agreement with damage captured by penetrant enhanced X-ray radiography. It has been shown that matrix cracking, axial splits, and delaminations that appear in the radiographs coincide either with the highest or lowest strain concentrations around the hole as measured by DIC. Additional interrupted fatigue tests were performed to elucidate the effect of stress level on the strain evolution during fatigue.

Moreover, non-contact vibration measurements were also conducted using a laser vibrometer to assess the frequency response signatures of fatigued open-hole composites. It has been shown that specific higher modes of vibration could be used as potential candidates of monitoring initiation of damage during fatigue as well as predicting the remnant fatigue lifetime. The effect of stress level on the residual natural frequencies was also investigated. It should be noted that at median fatigue lifetime ratios 0.3, 0.5 and 0.7, the specimens fatigued at a stress level corresponding to 70% of the ultimate tensile strength (UTS) experience the greatest change in natural frequency compared to specimens fatigued at stress levels corresponding to 75%UTS and 80%UTS. Nonetheless, at 0.1 median fatigue lifetime ratio the specimen fatigued at 70%UTS experience the smallest change in natural frequency compared to the specimens fatigued with 75%UTS and 80%UTS.

Furthermore, one of the main contributions of the present study is to combine the full-field measurement technique (DIC) with the non-contact vibration technique to monitor the degradation

process. The focus was not only on the qualitative aspects, but also on the quantitative evaluation of strain components and dynamic parameters

Indeed, the present research work has shown the potential of DIC and non-contact vibration measurement tools for online monitoring of composite structures. DIC is revealed as an efficient and simple methodology to study damage progress in laminates with discontinuities. Despite the fact that DIC is capable of predicting some of the failure mechanisms, it is still a challenge to accurately identify internal damage. Vibration measurements were able to present the effect of intrinsic damage at every fatigue lifetime ratio without giving any idea about the type, location and size of induced cracks within the damaged notched laminates

Finally, taking into account the importance of studying the vibration behavior of composite structures especially with discontinuities, different finite element models based on equivalent single-layer and layer-wise approaches as well as an analytical model based on Kirchhoff theory were developed to predict the natural frequencies and corresponding mode shapes of virgin notched composites. The obtained results from both analytical and numerical models were validated by the measured experimental results. It was demonstrated that the simple approach adopted in the analytical model to account for the local reduced stiffness induced by the hole was able to yield good agreement with the FEM and experimental results.

7.2. Future Work

Further work is required to investigate the ability of the DIC technique to capture the stacking sequence effect on surface displacements and strains. It would be interesting to use, in conjunction with DIC, infrared thermography through the use of FLIR cameras to measure the change in thermal fields during fatigue loading. Their combination will allow a coupled analysis of different demonstrations of same degradation mechanisms. It would be interesting as well to use a micro CT scan to reveal precisely and thoroughly all the progressive failure mechanisms during fatigue lifetime and relate them with the strain and temperature results obtained from both DIC and thermography techniques respectively.

Moreover, a discrete progressive fatigue damage model is required to be developed using a finite element model through the use of user material subroutine to predict the strain contours and compare them with the ones measured by DIC. The model will need to incorporate cohesive elements to model the delamination and the matrix crackings particularly around the hole. The use

of discrete damage modeling is essential to predict some of the complex strains at the vicinity of the hole. The numerical model should be then extended to predict the residual natural frequencies of fatigued specimen. In addition, the developed analytical model that is able to predict the modal parameters of pristine notched composites can be extended to predict the residual modal properties using the already tracked changes in strain profiles throughout fatigue lifetime. These changes of strains will be used appropriately to update the degraded elastic properties.

Bibliography

[1] B. Attaf, *Advances in composite materials for medicine and nanotechnology*: InTech, 2011.

[2] R. B. Heslehurst, *Defects and Damage in composite materials and structures*: CRC Press, 2014.

[3] R. C. Alderliesten, "Critical review on the assessment of fatigue and fracture in composite materials and structures," *Engineering Failure Analysis,* vol. 35, pp. 370-379, 12/15/ 2013.

[4] O. J. Nixon-Pearson and S. R. Hallett, "An investigation into the damage development and residual strengths of open-hole specimens in fatigue," *Composites Part A: Applied Science and Manufacturing,* vol. 69, pp. 266-278, 2// 2015.

[5] C. Goidescu, H. Welemane, C. Garnier, M. Fazzini, R. Brault, E. Péronnet*, et al.*, "Damage investigation in CFRP composites using full-field measurement techniques: Combination of digital image stereo-correlation, infrared thermography and X-ray tomography," *Composites Part B: Engineering,* vol. 48, pp. 95-105, 5// 2013.

[6] A. Matzenmiller, J. Lubliner, and R. L. Taylor, "A constitutive model for anisotropic damage in fiber-composites," *Mechanics of Materials,* vol. 20, pp. 125-152, 4// 1995.

[7] F. P. van der Meer, L. J. Sluys, S. R. Hallett, and M. R. Wisnom, "Computational modeling of complex failure mechanisms in laminates," *Journal of Composite Materials,* vol. 46, pp. 603-623, March 1, 2012 2012.

[8] P. P. Camanho, C. G. Davila, and M. F. de Moura, "Numerical Simulation of Mixed-Mode Progressive Delamination in Composite Materials," *Journal of Composite Materials,* vol. 37, pp. 1415-1438, August 1, 2003 2003.

[9] Q. Yang and B. Cox, "Cohesive models for damage evolution in laminated composites," *International Journal of Fracture,* vol. 133, pp. 107-137, 2005.

[10] M. L. Benzeggagh and M. Kenane, "Measurement of mixed-mode delamination fracture toughness of unidirectional glass/epoxy composites with mixed-mode bending apparatus," *Composites Science and Technology,* vol. 56, pp. 439-449, 1996/01/01 1996.

[11] A.Atas, "Strength prediction of mechanical joints in composite laminates based on subcritical damage modelling," The University of Sheffield, Sheffield, UK, 2012.

[12] L. B. M. a. D. F. Cheung C K "Composite strips with a circular stress concentration under tension " in *Proceedings of the SEM X International Congress & Exposition on Experimental and Applied Mechanics*

Costa Mesa, CA, 2004.

[13] A. Ataş and C. Soutis, "Subcritical damage mechanisms of bolted joints in CFRP composite laminates," *Composites Part B: Engineering,* vol. 54, pp. 20-27, 11// 2013.

[14] B. G. Green, M. R. Wisnom, and S. R. Hallett, "An experimental investigation into the tensile strength scaling of notched composites," *Composites Part A: Applied Science and Manufacturing,* vol. 38, pp. 867-878, 3// 2007.

[15] M. R. Wisnom and S. R. Hallett, "The role of delamination in strength, failure mechanism and hole size effect in open hole tensile tests on quasi-isotropic laminates," *Composites Part A: Applied Science and Manufacturing,* vol. 40, pp. 335-342, 4// 2009.

[16] L. Qin, Z. Zhang, Z. Feng, X. Li, Y. Wang, Y. Wang, *et al.*, "Full-field analysis of notch effects of 3D carbon/carbon composites," *Journal of Materials Science,* vol. 48, pp. 3454-3460, 2013/05/01 2013.
[17] M. A. Caminero, M. Lopez-Pedrosa, C. Pinna, and C. Soutis, "Damage Assessment of Composite Structures Using Digital Image Correlation," *Applied Composite Materials,* vol. 21, pp. 91-106, 2014/02/01 2014.
[18] J. M. Whitney and R. J. Nuismer, "Stress Fracture Criteria for Laminated Composites Containing Stress Concentrations," *Journal of Composite Materials,* vol. 8, pp. 253-265, July 1, 1974 1974.
[19] M. E. Waddoups, J. R. Eisenmann, and B. E. Kaminski, "Macroscopic Fracture Mechanics of Advanced Composite Materials," *Journal of Composite Materials,* vol. 5, pp. 446-454, October 1, 1971 1971.
[20] E. Martin, D. Leguillon, and N. Carrère, "A coupled strength and toughness criterion for the prediction of the open hole tensile strength of a composite plate," *International Journal of Solids and Structures,* vol. 49, pp. 3915-3922, 12/15/ 2012.
[21] S. R. Hallett, B. G. Green, W. G. Jiang, and M. R. Wisnom, "An experimental and numerical investigation into the damage mechanisms in notched composites," *Composites Part A: Applied Science and Manufacturing,* vol. 40, pp. 613-624, 5// 2009.
[22] A. Ataş and C. Soutis, "Strength prediction of bolted joints in CFRP composite laminates using cohesive zone elements," *Composites Part B: Engineering,* vol. 58, pp. 25-34, 3// 2014.
[23] M. Ridha, C. H. Wang, B. Y. Chen, and T. E. Tay, "Modelling complex progressive failure in notched composite laminates with varying sizes and stacking sequences," *Composites Part A: Applied Science and Manufacturing,* vol. 58, pp. 16-23, 3// 2014.
[24] Z. Su and L. Ye, "Lamb wave-based quantitative identification of delamination in CF/EP composite structures using artificial neural algorithm," *Composite Structures,* vol. 66, pp. 627-637, 10// 2004.
[25] R. Capozucca and B. Bonci, "Notched CFRP laminates under vibration," *Composite Structures,* vol. 122, pp. 367-375, 4// 2015.
[26] S. S. Kessler, S. M. Spearing, M. J. Atalla, C. E. S. Cesnik, and C. Soutis, "Damage detection in composite materials using frequency response methods," *Composites Part B: Engineering,* vol. 33, pp. 87-95, 1// 2002.
[27] Z. Zhang, K. Shankar, E. V. Morozov, and M. Tahtali, "Vibration-based delamination detection in composite beams through frequency changes," *Journal of Vibration and Control,* May 20, 2014 2014.
[28] Z. Kıral, B. M. İçten, and B. G. Kıral, "Effect of impact failure on the damping characteristics of beam-like composite structures," *Composites Part B: Engineering,* vol. 43, pp. 3053-3060, 12// 2012.
[29] M. R. Nasiri, M. J. Mahjoob, and A. Aghakasiri, "Damage Detection in a Composite Plate Using Modal Analysis and Artificial Intelligence," *Applied Composite Materials,* vol. 18, pp. 513-520, 2011/12/01 2011.
[30] "Abaqus Analysis User's Manual Section 7.2," ed, 2012.
[31] J. S. Mayes and A. C. Hansen, "Composite laminate failure analysis using multicontinuum theory," *Composites Science and Technology,* vol. 64, pp. 379-394, 3// 2004.
[32] "Abaqus Analysis User's Manual Section 24.3.3," version 6.12 ed, 2012.
[33] "Autodesk Simulation Composite Analysis - Theory Manual," ed, 2014.

[34] "Autodesk Simulation Composite Analysis - User's Guide for Abaqus
", ed, 2014.
[35] K. Doug, N. Emmett, R. Don, and M. Gerald, "Developing Guidelines for the Application of Coupled Fracture/Continuum Mechanics - Based Composite Damage Models for Reducing Mesh Sensitivity," in *53rd AIAA/ASME/ASCE/AHS/ASC Structures, Structural Dynamics and Materials Conference*, ed: American Institute of Aeronautics and Astronautics, 2012.
[36] "Aramis User Manual-Hardware," Version 6 ed, 2007.
[37] "Aramis User Manual-Software," Version6 ed, 2007.
[38] S. D. Alan Baker, Donald Kelly, *Composite Materials for Aircraft Structures Second Edition*, 2004.
[39] M. A. Caminero, M. Lopez-Pedrosa, C. Pinna, and C. Soutis, "Damage monitoring and analysis of composite laminates with an open hole and adhesively bonded repairs using digital image correlation," *Composites Part B: Engineering,* vol. 53, pp. 76-91, 10// 2013.
[40] M. Kashfuddoja and M. Ramji, "Whole-field strain analysis and damage assessment of adhesively bonded patch repair of CFRP laminates using 3D-DIC and FEA," *Composites Part B: Engineering,* vol. 53, pp. 46-61, 10// 2013.
[41] e-Xtream-engineering, "Digimat manual 5.1.1," ed, 2014.
[42] A. Poursartip, M. F. Ashby, and P. W. R. Beaumont, "The fatigue damage mechanics of a carbon fibre composite laminate: I—development of the model," *Composites Science and Technology,* vol. 25, pp. 193-218, // 1986.
[43] S. M. Spearing and P. W. R. Beaumont, "Fatigue damage mechanics of composite materials. I: Experimental measurement of damage and post-fatigue properties," *Composites Science and Technology,* vol. 44, pp. 159-168, // 1992.
[44] A. P. Vassilopoulos and T. Keller, *Fatigue of Fiber-reinforced Composites*, 2011.
[45] R. D. Jamison, K. Schulte, K. L. Reifsneider, and W. W. Stinchcomb, "Characterization and Analysis of Damage Mechanisms in Tension-Tension Fatigue of Graphite/Epoxy Laminates," in *Effects of Defects in Composite Materials, American Society for Testing and Materials*, 1984, pp. 21-55.
[46] M. R. Bhat, M. A. Majeed, and C. R. L. Murthy, "Characterization of fatigue damage in unidirectional GFRP composites through acoustic emission signal analysis," *NDT & E International,* vol. 27, pp. 27-32, 2// 1994.
[47] E. K. Gamstedt, L. A. Berglund, and T. Peijs, "Fatigue mechanisms in unidirectional glass-fibre-reinforced polypropylene," *Composites Science and Technology,* vol. 59, pp. 759-768, 4// 1999.
[48] J. Bartley-Cho, S. Gyu Lim, H. T. Hahn, and P. Shyprykevich, "Damage accumulation in quasi-isotropic graphite/epoxy laminates under constant-amplitude fatigue and block loading," *Composites Science and Technology,* vol. 58, pp. 1535-1547, 9// 1998.
[49] P. Margueres, F. Meraghni, and M. L. Benzeggagh, "Comparison of stiffness measurements and damage investigation techniques for a fatigued and post-impact fatigued GFRP composite obtained by RTM process," *Composites Part A: Applied Science and Manufacturing,* vol. 31, pp. 151-163, 2// 2000.
[50] D. S. de Vasconcellos, F. Touchard, and L. Chocinski-Arnault, "Tension–tension fatigue behaviour of woven hemp fibre reinforced epoxy composite: A multi-instrumented damage analysis," *International Journal of Fatigue,* vol. 59, pp. 159-169, 2// 2014.

[51] I. El Sawi, Z. Fawaz, R. Zitoune, and H. Bougherara, "An investigation of the damage mechanisms and fatigue life diagrams of flax fiber-reinforced polymer laminates," *Journal of Materials Science,* vol. 49, pp. 2338-2346, 2014/03/01 2014.

[52] J. Montesano, Z. Fawaz, and H. Bougherara, "Use of infrared thermography to investigate the fatigue behavior of a carbon fiber reinforced polymer composite," *Composite Structures,* vol. 97, pp. 76-83, 3// 2013.

[53] J. Montesano, H. Bougherara, and Z. Fawaz, "Application of infrared thermography for the characterization of damage in braided carbon fiber reinforced polymer matrix composites," *Composites Part B: Engineering,* vol. 60, pp. 137-143, 4// 2014.

[54] R. Steinberger, T. I. Valadas Leitão, E. Ladstätter, G. Pinter, W. Billinger, and R. W. Lang, "Infrared thermographic techniques for non-destructive damage characterization of carbon fibre reinforced polymers during tensile fatigue testing," *International Journal of Fatigue,* vol. 28, pp. 1340-1347, 10// 2006.

[55] V. Dattoma and S. Giancane, "Evaluation of energy of fatigue damage into GFRC through digital image correlation and thermography," *Composites Part B: Engineering,* vol. 47, pp. 283-289, 4// 2013.

[56] W. R. Broughton, M. R. L. Gower, M. J. Lodeiro, G. D. Pilkington, and R. M. Shaw, "An experimental assessment of open-hole tension–tension fatigue behaviour of a GFRP laminate," *Composites Part A: Applied Science and Manufacturing,* vol. 42, pp. 1310-1320, 10// 2011.

[57] S. S. S. K. D. Z. F. Edgren, "Fatigue testing of composites with in-situ full-field strain measurement," in *18TH INTERNATIONAL CONFERENCE ON COMPOSITE MATERIALS*, Korea, 2011.

[58] G. H. Erçin, P. P. Camanho, J. Xavier, G. Catalanotti, S. Mahdi, and P. Linde, "Size effects on the tensile and compressive failure of notched composite laminates," *Composite Structures,* vol. 96, pp. 736-744, 2// 2013.

[59] R. Zitoune, L. Crouzeix, F. Collombet, T. Tamine, and Y. H. Grunevald, "Behaviour of composite plates with drilled and moulded hole under tensile load," *Composite Structures,* vol. 93, pp. 2384-2391, 8// 2011.

[60] T. Yang, Z. Li, J. Wang, and L. Tong, "Overall moduli and natural frequencies of composite laminates containing multiple interlaminar transverse cracks," *Composite Structures,* vol. 66, pp. 223-230, 10// 2004.

[61] S. H. Diaz Valdes and C. Soutis, "DELAMINATION DETECTION IN COMPOSITE LAMINATES FROM VARIATIONS OF THEIR MODAL CHARACTERISTICS," *Journal of Sound and Vibration,* vol. 228, pp. 1-9, 11/18/ 1999.

[62] N. E. Bedewi and D. N. Kung, "Effect of fatigue loading on the modal properties of composite structures and its utilization for prediction of residual life," *Composite Structures,* vol. 37, pp. 357-371, 3// 1997.

[63] M. Abo-Elkhier, A. A. Hamada, and A. Bahei El-Deen, "Prediction of fatigue life of glass fiber reinforced polyester composites using modal testing," *International Journal of Fatigue,* vol. 69, pp. 28-35, 12// 2014.

[64] T.-C. Moon, H.-Y. Kim, and W. Hwang, "Natural-frequency reduction model for matrix-dominated fatigue damage of composite laminates," *Composite Structures,* vol. 62, pp. 19-26, 10// 2003.

[65] H. Y. Kim, "VIBRATION-BASED DAMAGE IDENTIFICATION USING RECONSTRUCTED FRFS IN COMPOSITE STRUCTURES," *Journal of Sound and Vibration,* vol. 259, pp. 1131-1146, 1/30/ 2003.
[66] M. A. Sutton, J.-J. Orteu, and H. W. Schreir, *Image Correlarion for Shape, Motion and Deformation Measurements*
Springer US, 2009.
[67] O. J. Nixon-Pearson, S. R. Hallett, P. J. Withers, and J. Rouse, "Damage development in open-hole composite specimens in fatigue. Part 1: Experimental investigation," *Composite Structures,* vol. 106, pp. 882-889, 12// 2013.
[68] S. L. Ogin, P. A. Smith, and P. W. R. Beaumont, "Matrix cracking and stiffness reduction during the fatigue of a (0/90)s GFRP laminate," *Composites Science and Technology,* vol. 22, pp. 23-31, // 1985.
[69] R. Talreja, "Stiffness properties of composite laminates with matrix cracking and interior delamination," *Engineering Fracture Mechanics,* vol. 25, pp. 751-762, // 1986.
[70] S. M. Spearing, P. W. R. Beaumont, and P. A. Smith, "Fatigue damage mechanics of composite materials Part IV: Prediction of post-fatigue stiffness," *Composites Science and Technology,* vol. 44, pp. 309-317, // 1992.
[71] M. Kashfuddoja, R. G. R. Prasath, and M. Ramji, "Study on experimental characterization of carbon fiber reinforced polymer panel using digital image correlation: A sensitivity analysis," *Optics and Lasers in Engineering,* vol. 62, pp. 17-30, 11// 2014.
[72] W. W. Stinchcomb and C. E. Bakis, "Chapter 4 - Fatigue Behavior of Composite Laminates," in *Composite Materials Series*. vol. Volume 4, K. L. Reifsnider, Ed., ed: Elsevier, 1991, pp. 105-180.
[73] B. Aydi, M. A. Ben Hassena, and S. Choura, "Modal analysis of cracked wind turbines using the finite element method," in *Systems, Signals and Devices (SSD), 2012 9th International Multi-Conference on*, 2012, pp. 1-6.
[74] J. Bai, "1 - Introduction," in *Advanced Fibre-Reinforced Polymer (FRP) Composites for Structural Applications*, J. Bai, Ed., ed: Woodhead Publishing, 2013, pp. 1-4.
[75] A. Bilel and W. C. Scott, "Experimental and numerical monitoring of strain gradients in notched composites under tension loading," in *56th AIAA/ASCE/AHS/ASC Structures, Structural Dynamics, and Materials Conference*, ed: American Institute of Aeronautics and Astronautics, 2015.
[76] R. Kalhor and S. W. Case, "The effect of FRP thickness on energy absorption of metal-FRP square tubes subjected to axial compressive loading," *Composite Structures,* vol. 130, pp. 44-50, 10/15/ 2015.
[77] D. J. Bull, S. M. Spearing, and I. Sinclair, "Investigation of the response to low velocity impact and quasi-static indentation loading of particle-toughened carbon-fibre composite materials," *Composites Part A: Applied Science and Manufacturing,* vol. 74, pp. 38-46, 7// 2015.
[78] B. Aidi, M. K. Philen, and S. W. Case, "Progressive damage assessment of centrally notched composite specimens in fatigue," *Composites Part A: Applied Science and Manufacturing,* vol. 74, pp. 47-59, 7// 2015.
[79] E. M. Jensen and R. S. Fertig, "Physics-Based Multiscale Creep Strain and Creep Rupture Modeling for Composite Materials," *AIAA Journal,* pp. 1-9, 2015.
[80] C. H. Thai, H. Nguyen-Xuan, N. Nguyen-Thanh, T. H. Le, T. Nguyen-Thoi, and T. Rabczuk, "Static, free vibration, and buckling analysis of laminated composite Reissner–

Mindlin plates using NURBS-based isogeometric approach," *International Journal for Numerical Methods in Engineering,* vol. 91, pp. 571-603, 2012.
[81] F. Alijani, M. Amabili, G. Ferrari, and V. D'Alessandro, "Nonlinear vibrations of laminated and sandwich rectangular plates with free edges. Part 2: Experiments & comparisons," *Composite Structures,* vol. 105, pp. 437-445, 11// 2013.
[82] V. N. Burlayenko, H. Altenbach, and T. Sadowski, "An evaluation of displacement-based finite element models used for free vibration analysis of homogeneous and composite plates," *Journal of Sound and Vibration,* vol. 358, pp. 152-175, 12/8/ 2015.
[83] F. A. Fazzolari, M. Boscolo, and J. R. Banerjee, "An exact dynamic stiffness element using a higher order shear deformation theory for free vibration analysis of composite plate assemblies," *Composite Structures,* vol. 96, pp. 262-278, 2// 2013.
[84] W. Zhen, S. H. Lo, and R. Xiaohui, "A C0 zig-zag model for the analysis of angle-ply composite thick plates," *Composite Structures,* vol. 127, pp. 211-223, 9/1/ 2015.
[85] J. Javanshir, T. Farsadi, and U. Yuceoglu, "Free Vibrations of Composite Base Plates Stiffened by Two Adhesively Bonded Plate Strips," *Journal of Aircraft,* vol. 49, pp. 1135-1152, 2012/07/01 2012.
[86] A. S. Sayyad and Y. M. Ghugal, "On the free vibration analysis of laminated composite and sandwich plates: A review of recent literature with some numerical results," *Composite Structures,* vol. 129, pp. 177-201, 10/1/ 2015.
[87] A. K. Noor, "Free vibrations of multilayered composite plates," *AIAA Journal,* vol. 11, pp. 1038-1039, 1973/07/01 1973.
[88] J. N. Reddy, "Free vibration of antisymmetric, angle-ply laminated plates including transverse shear deformation by the finite element method," *Journal of Sound and Vibration,* vol. 66, pp. 565-576, 1979/10/22 1979.
[89] R. P. Khandelwal and A. Chakrabarti, "Calculation of interlaminar shear stresses in laminated shallow shell panel using refined higher order shear deformation theory," *Composite Structures,* vol. 124, pp. 272-282, 6// 2015.
[90] H. Murakami, "Laminated Composite Plate Theory With Improved In-Plane Responses," *Journal of Applied Mechanics,* vol. 53, pp. 661-666, 1986.
[91] X. Lu and D. Liu, "An Interlaminar Shear Stress Continuity Theory for Both Thin and Thick Composite Laminates," *Journal of Applied Mechanics,* vol. 59, pp. 502-509, 1992.
[92] S. Srinivas, "A refined analysis of composite laminates," *Journal of Sound and Vibration,* vol. 30, pp. 495-507, 10/22/ 1973.
[93] M. Boscolo, "Analytical solution for free vibration analysis of composite plates with layer-wise displacement assumptions," *Composite Structures,* vol. 100, pp. 493-510, 6// 2013.
[94] E. Carrera, "Layer-Wise Mixed Models for Accurate Vibrations Analysis of Multilayered Plates," *Journal of Applied Mechanics,* vol. 65, pp. 820-828, 1998.
[95] E. Carrera, "Historical review of Zig-Zag theories for multilayered plates and shells," *Applied Mechanics Reviews,* vol. 56, pp. 287-308, 2003.
[96] E. Carrera, "Theories and Finite Elements for Multilayered Plates and Shells:A Unified compact formulation with numerical assessment and benchmarking," *Archives of Computational Methods in Engineering,* vol. 10, pp. 215-296, 2003/09/01 2003.
[97] E. Viola, F. Tornabene, and N. Fantuzzi, "Generalized differential quadrature finite element method for cracked composite structures of arbitrary shape," *Composite Structures,* vol. 106, pp. 815-834, 12// 2013.

[98] Y. C. Chen and C. Hwu, "Boundary element method for vibration analysis of two-dimensional anisotropic elastic solids containing holes, cracks or interfaces," *Engineering Analysis with Boundary Elements,* vol. 40, pp. 22-35, 3// 2014.
[99] N. Fantuzzi, F. Tornabene, E. Viola, and A. J. M. Ferreira, "A strong formulation finite element method (SFEM) based on RBF and GDQ techniques for the static and dynamic analyses of laminated plates of arbitrary shape," *Meccanica,* vol. 49, pp. 2503-2542, 2014/10/01 2014.
[100] L. Tong and G. P. Steven, *Analysis and design of structural bonded joints*. Boston :: Kluwer Academic, 1999.
[101] Abaqus Theory Guide Section3 v6.14.
[102] J. N. Reddy, *Mechanics of laminated composites plates: Theory and analysis*: Boca Raton: CRC Press, 1997.